POLITECNICO DI TORINO

Corso di Laurea Magistrale in Ingegneria Energetica e Nucleare

Tesi Magistrale

CFD analysis of a Loss-of-Coolant Accident from a He-cooled blanket in the EU DEMO Vacuum Vessel

Relatore:
Prof. Laura Savoldi

Candidato:
Gianluca Digioia

Anno Accademico 2017/2018

Abstract

This dissertation is dedicated to a Computational Fluid Dynamic (CFD) analysis of an accidental sequence caused by the release of pressurized helium into the EU DEMO Vacuum Vessel from the cooling circuit of a He-cooled Breeding Blanket (BB). This work was performed at the NEMO computational laboratory based in the Energy department (DENERG) of Politecnico di Torino.

The safety assessment of the Vacuum Vessel is compulsory as it contains a moderate inventory of radioactive material and it is designed to stand a maximum pressure of 2 bar: in this framework, one of the Design Basis Accident (DBA) regarding the Vacuum Vessel is the in-Vessel Loss of Coolant Accident (in-VV LOCA) that foresees the release of highly pressurised helium from the cooling circuits of the Breeding Blankets towards the VV. On this topic, 0D simulations have already been performed, but their results might be not conservative

The purpose of this thesis is to perform a 2D and 3D CFD simulations of the in-VV LOCA. The comparison of the results obtained from a 0D study is performed, as well as the investigation of the occurrence of pressure peaks on the walls directly interested by the impingement of the helium jet that develops in such conditions.

The CFD simulations verify the general trend of the 0D results for the average quantities confirming, however, that local informations play a key role assessing the presence of dangerous pressure peaks on the VV surfaces slightly below the safety limits on the walls of the VV.

Contents

List of Figures

List of Tables

List of Abbreviations

AMR	**A**daptive **M**esh **R**efinement
BB	**B**reeding **B**lanket
BC	**B**oundary **C**ondition
BD	**B**urst **D**isk
BL	**B**leed **L**ine
BV	**B**leed **V**alve
DBA	**D**esign **B**asis **A**ccident
DEMO	**DEMO**nstrating fusion power reactor
EV	**E**xpansion **V**olume
FW	**F**irst **W**all
GETTHEM	**GE**neral **T**okamak **THE**rmal-hydraulic **M**odelling
HCPB	**H**elium **C**ooled **P**ebble **B**ed
IC	**I**nitial **C**ondition
ICE	**I**ngress of **C**oolant **E**vent
ITER	**I**nternational **T**hermonuclear **E**xperimental **R**eactor
LOCA	**L**oss **O**f **C**oolant **A**ccident
PHTS	**P**rimary **H**eat **T**ransferl **S**ystem
RL	**R**elief **L**ine
SP	**S**uppression **P**ool
VV	**V**acuum **V**essel
VVPSS	**V**acuum **V**essel **P**ressure **S**uppression **S**ystem
WCLL	**W**ater **C**ooled **L**ithium **L**ead

Chapter 1

Introduction

The heat emitted by the stars comes from fusion reactions in their cores. The extreme temperature and gravity inside these stellar bodies create the perfect conditions for hydrogen nuclei to collide and fuse together in heavier particles, principally helium. For fusion reactions to occur, it is necessary that the natural electrostatic repulsion between the two colliding particles is overcome by an external force. Since the mass of the resulting helium atom is lower than the sum of the initial fused particles, the loss of mass results in a very strong release of heat. The amount of energy (E) freed by each fusion reaction can be evaluated from the Einstein's formula:

$$E = \Delta mc^2 \tag{1.1}$$

where Δm, called loss of mass, represents the difference between the mass of reagents and products of the reactions and c represents the speed of light. Being the speed of light a very big value, even a tiny defect of mass can cause a strong release of energy.

In the past few years, scientists and researchers have started to study a feasible way to reproduce fusion reactions on Earth and identified the so-called deuterium-tritium (DT) reaction as the optimal one which maximizes the energy gain while maintaining a low operative temperature:

$${}^2_1D + {}^3_1T \rightarrow {}^4_2He^{1+} + e^- + n + \bar{\nu}_e \tag{1.2}$$

As showed in Equation 1.2, the needed fuel for fusion reactions is composed by two isotopes of hydrogen: Deuterium and Tritium. Deuterium can be extracted directly from water: its mining technique is established and regularly applied for scientific and industrial purposes [23]. Conversely, Tritium is a very instable isotope and quickly decades into an atom of helium. This is the cause of its relatively poor concentration in nature [23]. A direct way of producing tritium is to “breed” it by forcing the interaction between neutrons and Lithium atoms. Since neutrons are also a product of fusion reactions, they can be reused to collide with Lithium to produce Tritium. Lithium can be extracted by land-based resources and ocean water and its inventory is supposed to be enough to meet the world's energy demand for more than 5 million years [23].

Fusion reactions occur on Earth only if the fuel is in plasma conditions which is a state of matter obtainable by over-heating particles at very high temperatures (at least 150 000 000 K) and semi-vacuum conditions (order of μPa) so that electrons separate from their nuclei. Gaseous hydrogen in plasma condition is the environment in which hydrogen atoms can be brought to fuse and yield energy: such conditions can be recreated inside a device called tokamak.

The construction of a tokamak capable of producing electric energy is the final objective of fusion engineers and scientists and can bring to a strong reduction of greenhouse gas emissions . Several advantages are related to fusion technology applications:

- Concentrated energy: at equal mass of fuel, fusion reactions produce four million times more energy than a chemical reaction (coal, oil or gas) and four times as much as nuclear fission reactions.
- Fuel availability: fusion fuels can easily be extracted and is nearly inexhaustible.
- No greenhouse gases: fusion reactions do not produce anything but helium, an inert and non toxic gas. No greenhouse gases are produced.
- No long-lived radioactive waste: the biggest problem of nuclear fission plants is the production of long-lived radioactive waste. In fusion reactors, the activated components will be short-lived nuclear waste (<100 years).
- No proliferation: fusion reactors do not employ uranium and plutonium.
- No risk of meltdown: if something goes wrong inside the tokamak, and the plasma is shut off, all the reactions stops. No decay heat is present nor chain reactions.

In this framework, the ITER project was born [6, 8, 23].

1.1 The ITER project

In 1985, the ITER project was first launched. It is a very ambitious project whose objective is to build the world's largest tokamak [6] to prove the feasibility of fusion as a large scale and carbon-free source of energy. The ITER members (China, EU, Japan, India, Korea, Russia and the USA) cooperate to build this experimental tokamak in Saint Paul-lez-Durance, near Cadarache in the south of France. The five main goals of the project are:

1. Produce an amount of energy 10 times higher than the input heating power. Until date, no fusion reactor has been able to produce net positive energy. Even if ITER is not designed to collect the produced energy, it can demonstrate the feasibility of fusion-based electricity production.
2. Prove the integration of all the technologies that will be held in a future fusion power plant. All the previous fusion reactors were too small to be considered representative of a future fusion power plant; the operative conditions in ITER are those foreseen to exist in the future fusion power plants.
3. Realize an auto-sustained D-T plasma by internal heating. Until date, the D-T plasma is heated from the outside of the VV by means of neutral beam injection and high-frequency electromagnetic waves.
4. Produce tritium inside the VV. In ITER, the first breeding blanket for the production of tritium will be tested. This objective is very important due to the lack of tritium in the world [6, 23].
5. Demonstrate the inherent safety of a fusion power plant [6, 23].

1.1.1 The ITER tokamak

The ITER tokamak, sketched in Figure 1.1, is composed by the following components:

- Vacuum Vessel (VV)
- Blankets
- Magnets
- Divertor
- Cryostat

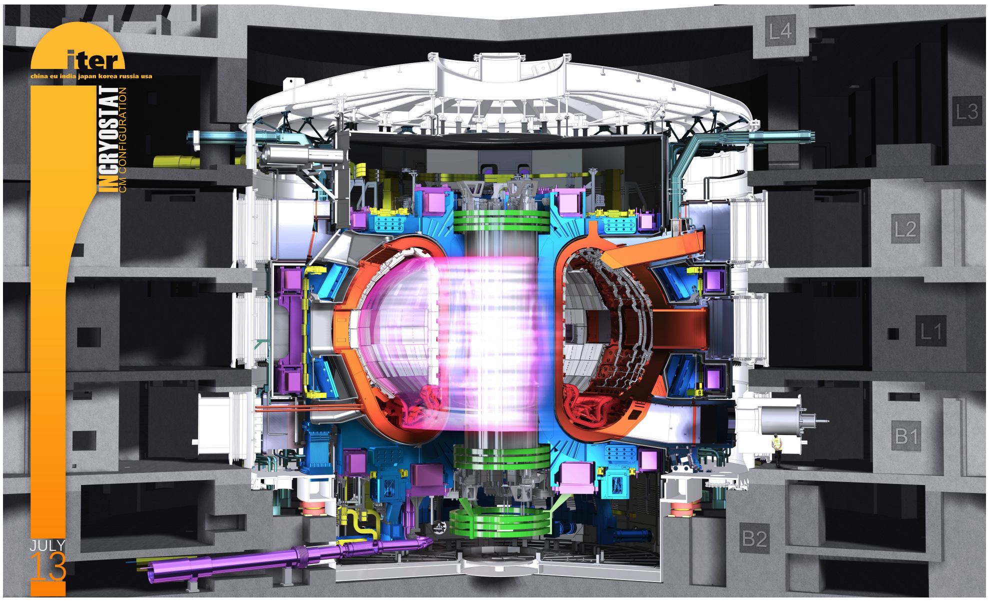

FIGURE 1.1: The ITER tokamak [23].

The Vacuum Vessel A sketch of the toroidal VV is shown in Figure 1.2. Made of stainless steel, it contains the plasma and will host all the ITER fusion experimental reactions [23]. A water based cooling system located in the vessel's double steel walls, extracts the excessive heat load deposited on the VV surfaces. With a volume of 1400 m^3 it will be the biggest VV in the world [6, 23]. This component has also a safety feature since it works as a passive primary containment barrier.

The Blankets The inner walls of the VV are totally covered by 440 blanket modules [23] (see Figure 1.3) whose purpose, in ITER, is to protect the VV surfaces and structures from the strong magnetic fields, the free neutron fluxes and the high heat loads. These components are made of beryllium on the plasma facing surface (called First Wall, FW) while the internal portion is made of copper and stainless steel. Some blanket modules, called Breeding Blankets (BB), will be tested to check the feasibility of an on-stage production of tritium by collisions of neutrons (from plasma) with lithium.

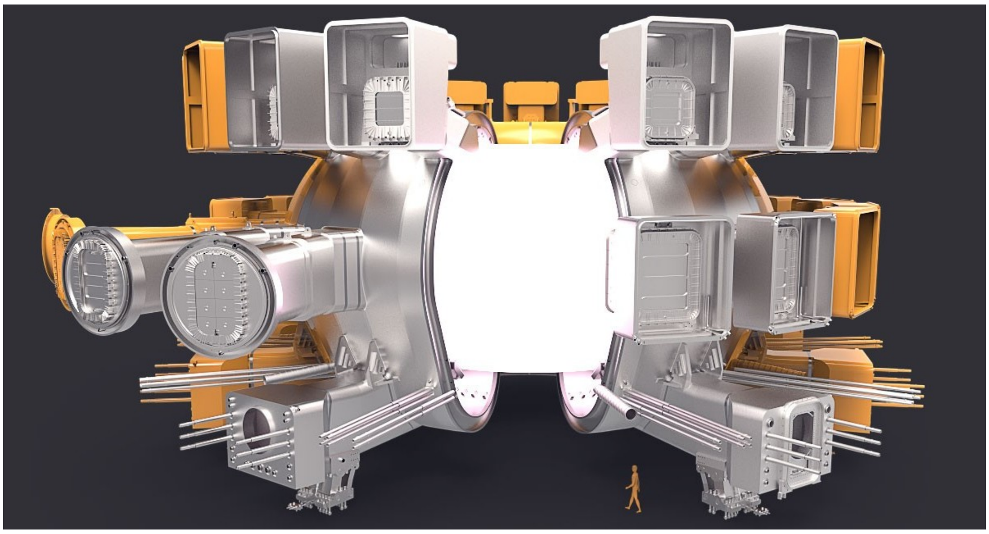

FIGURE 1.2: The ITER Vacuum Vessel [23].

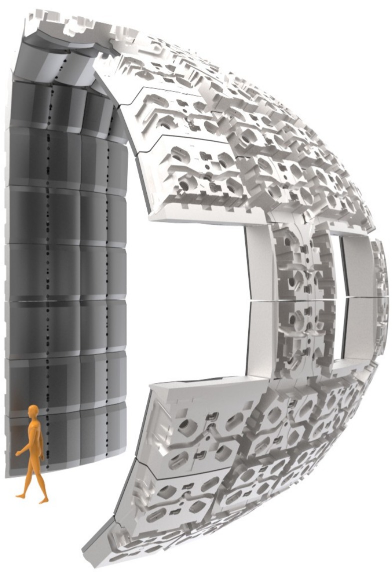

FIGURE 1.3: The ITER blanket [23].

The Magnets These components, showed in Figure 1.4, aim at creating a magnetic cage that prevent particles from escaping from the VV, confining plasma in a narrow section of the VV increasing its density and collision rate and, from the technological point of view, avoiding the hot plasma to be in contact with the VV surfaces. Strong magnetic fields produced by superconducting magnets located all around the VV, confine the natural charged plasma. These magnetic fields are produced by 4 different systems which are the toroidal field system, the poloidal field system, central solenoid and correction field system.

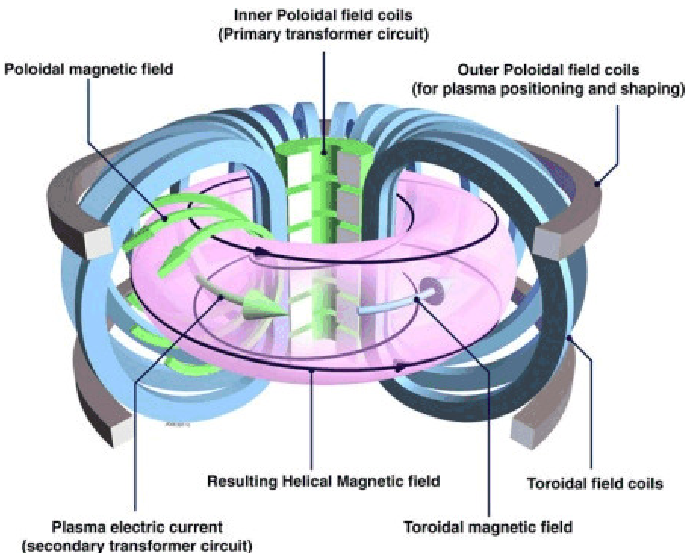

FIGURE 1.4: Magnetic confinement of plasma [15].

The Divertor This stainless steel and tungsten component, sketched in Figure 1.5, is located at the bottom of the VV. Its purposes are to extract helium ash produced by the cool down of energetic alpha particles generated in fusion reactions avoiding plasma contamination and dilution, and protect the bottom part of the VV which is characterised by strong neutronic and thermal loads.

FIGURE 1.5: The ITER divertor [23].

The Cryostat The ITER cryostat, made of stainless steel, provides the necessary conditions for the tokamak to correctly work: high vacuum and ultra-cool environment for VV and the superconducting magnets. Due to the very different and extreme operative conditions, it is designed to cope with thermal expansions and contractions. Figure 1.6 shows this component.

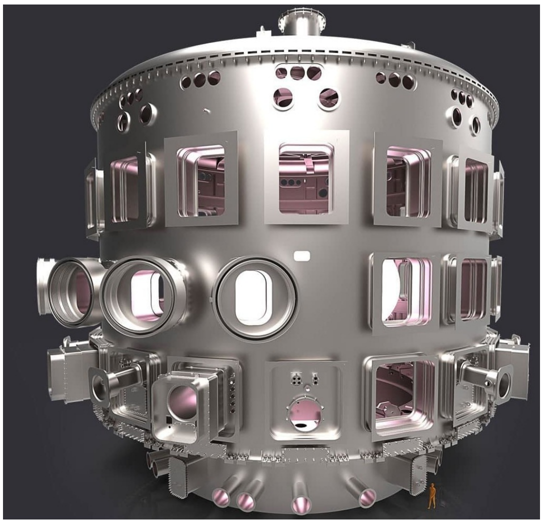

FIGURE 1.6: The ITER cryostat [23].

1.2 After ITER: the EU DEMO power plant

Once performed all the necessary studies in the ITER experimental utility, the DEMOnstration reactor will be built. Its construction is foreseen to start in the 2030s and operation in the 2040s. The objective of the DEMO machine is the production of electricity from fusion reactions: this device should produce from 30 to 50 times the initially injected energy used to sustain the operating condition of the tokamak [23]. With the reduction of CO2 emissions driving future energy policy, fusion can start market penetration around 2050 with up to 30% of electricity production by 2100 [6].

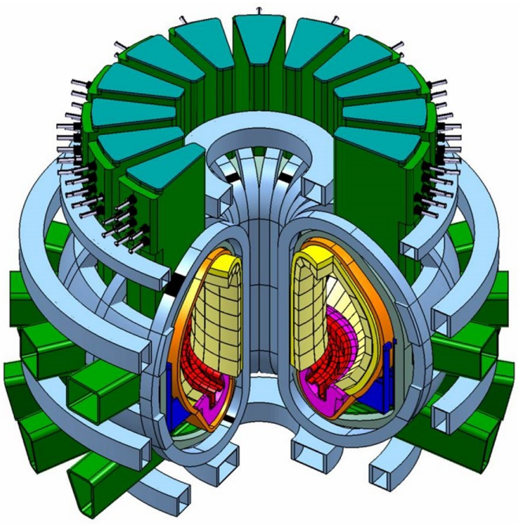

FIGURE 1.7: The EU DEMO reactor[28].

In the European Demonstration Fusion Power Plant (EU DEMO), the integrity of the Vacuum Vessel is of concern since it represents the primary containment barrier to radioactive release in case of accidental sequences. In the design process of a nuclear plant, its inherent safety is guaranteed by the preliminary analyses of each possible sequence that could occur and bring to accidental conditions. This study is characterised by a deep focus on the accident as well as the mitigation procedures to follow or countermeasures to take. The dangerous sequence is called Design Basis Accident (DBA).

One of the most critical DBA is the in-vessel Loss-Of-Coolant Accident (in-VV LOCA) caused by a break in the First Wall of the Breeding Blanket with a consequent release of coolant into the VV also called Ingress of Coolant Event (ICE).

In case of in-VV LOCA, a key role is played by the VV Pressure Suppression Systems (VVPSS) whose aim is to mitigate the pressurization of the VV following this kind of accidents. These systems are respectively suppression pools (SPs) or expansions volumes (EVs) in case of release from a water-cooled Breeding Blanket (BB) or helium-cooled BB.

1.3 The in-VV LOCA for helium cooled BB

Inside the VV of the DEMO reactor, the tritium fuel is produced inside the Breeding Blanket, allowing neutrons freed from fusion reactions to collide with lithium hosted by the BB. In the accidental scenario, a toroidally continuous strip of FW is supposed to be melted by runaway electrons. Due to the proximity of the FW cooling channels to the FW, all the channels below the melted surface are supposed to be exposed to the plasma volume as the FW surface melts. Figure 1.8 shows the break scenario in case of a Helium Cooled Pebble Bed (HCPB) BB, which is cooled by the Primary Heat Transfer System (PHTS).

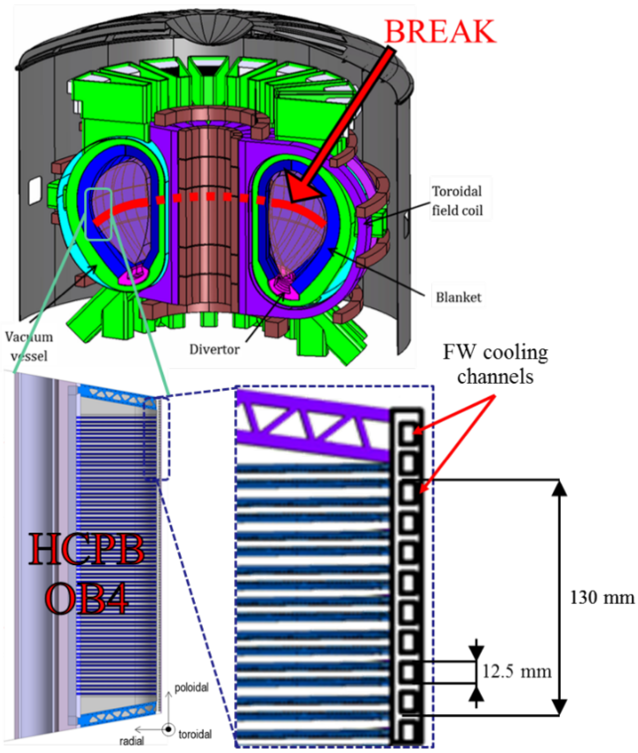

FIGURE 1.8: LOCA location in the DEMO VV [2, 16].

In the PHTS, the coolant is pressurised at 80 bar and at a temperature of 673 K [2, 16]. After the break, due to the huge pressure difference between the VV (5 μPa) and the PHTS, choked flow occurs, limiting the flow to the VV. As the transient proceeds, the coolant from the BB enters the VV and rapidly pressurizes it. A free jet develops inside the VV and impinges on its internal walls. In order to avoid the overpressure of the VV, which has a maximum operative pressure of 2 bar, more safety systems are conceived: the Vacuum Vessel Pressure Suppression Systems (VVPSS).

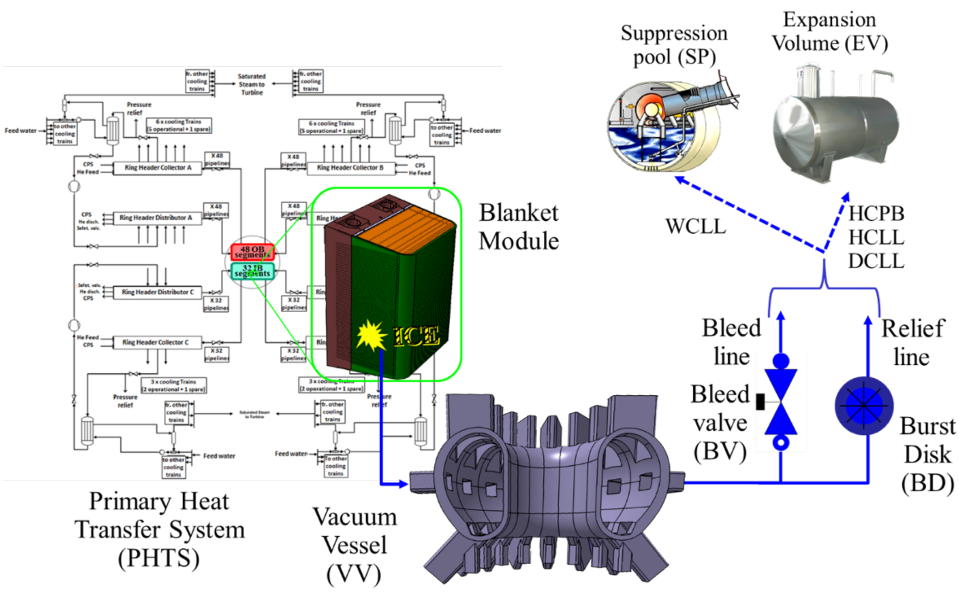

FIGURE 1.9: Schematic of the relations between the PHTS, the VV and the PHTS [16].

The simplified layout of the EU DEMO VVPSS is reported in Figure 1.9. The domain is composed by the PHTS that cools the BB; the VV, which contains the BB; to avoid overpressure, the VV must be connected to the VVPSS by means of one or more relief lines (RLs), equipped with burst disks (BDs), and by smaller lines (called bleed lines, BLs, useful for small leakages) equipped with actively operated valves (bleed valves, BVs). Once the pressure on the BDs and BVs has reached the breaking/opening set-point, the coolant starts flowing towards the VVPSS. Since the VVPSS is kept at very low pressure, also the flows through the BDs and BVs are foreseen to be choked [2, 16].

1.3.1 Previous studies

Due to the safety role of the VVPSS, their design and sizing are very important. In the framework of this task, in the last years, a thermal-hydraulic model of the EU DEMO VVPSS, for both helium and water based BB solutions, has been developed within the GEneral Tokamak THErmal-hydraulic Modelling (GETTHEM) code enabling fast parametric analyses on the system. This tool, based on the Modelica language, which is an equation-based acausal object-oriented modelling language aimed at simplified modelling of complex systems [19], is able to evaluate both water and helium based transients [16, 17]. Figure 1.10 shows the GETTHEM model of the EU DEMO VVPSS.

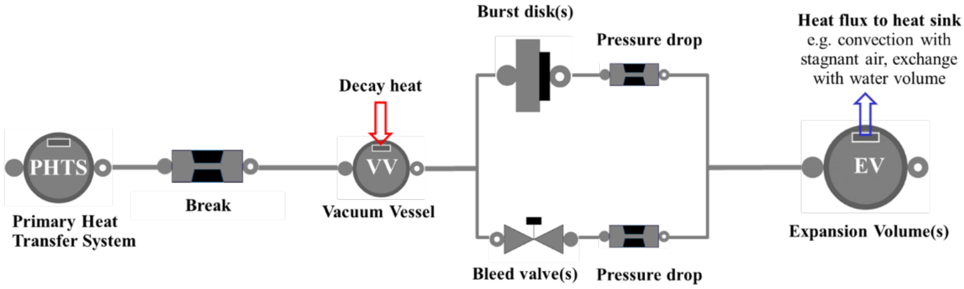

FIGURE 1.10: GETTHEM model of the EU DEMO VVPSS for helium coolant [16].

Each component is modelled as a 0D constant-volume tank; the break, BVs and BDs are modelled in order to take into account the choked flow that occurs during the transient. When the simulation starts, each component is considered to be full of helium and at its initial operative conditions (outlined in Table 1.1).

TABLE 1.1: Value of the initial conditions for the in-VV LOCA [16].

PHTS	
Volume [m^3]	2325
Initial pressure [MPa]	80
Initial temperature [K]	673
Break	
Cross section [m^2]	
VV	
Volume [m^3]	3000
Real initial pressure [μPa]	5
EV	
Volume [m^3]	120 000
Initial pressure [kPa]	4.2

The main results of the 0D study [2, 16] are showed in Figures 1.11 and 1.12.

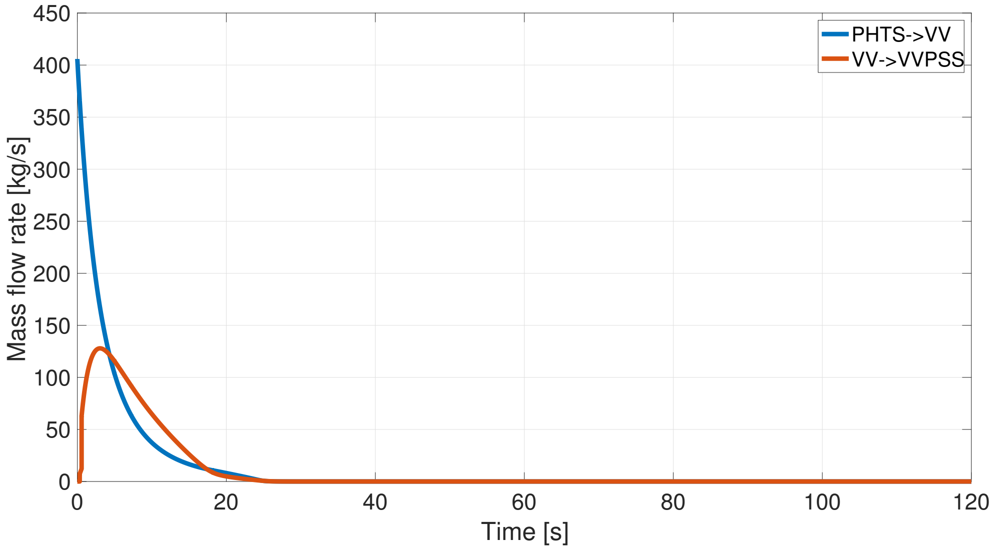

FIGURE 1.11: Evolution of the flow rates in the three considered volumes [2, 16].

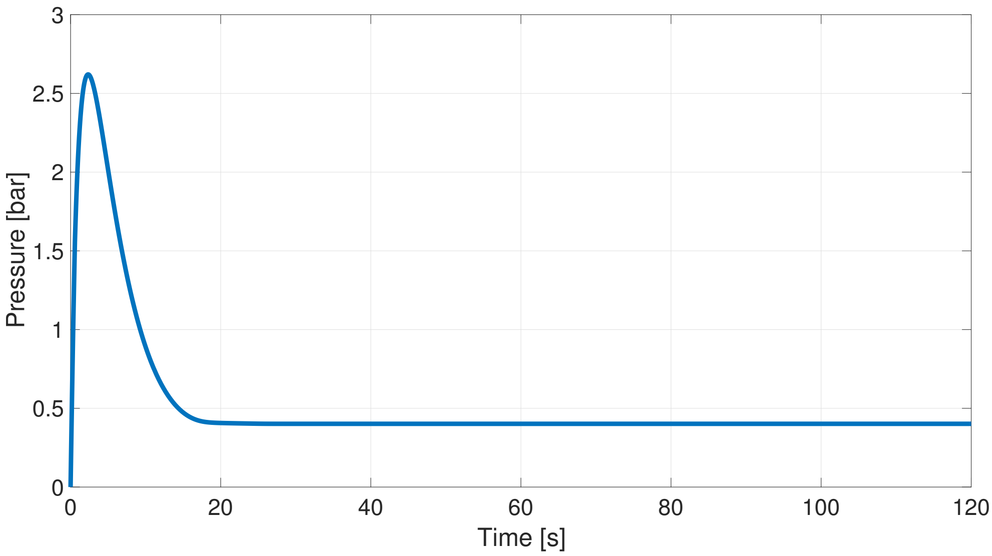

FIGURE 1.12: Evolution of the pressure for the HCPB in-vessel LOCA scenario [2, 16].

1.3.2 Objectives of this work

The aim of this thesis is to preliminarily compare the results obtained with the 0D MODELICA analysis of the in-VV LOCA [2, 16] with a CFD analysis of the same accident simulated on a 2D and 3D simplified geometries. Once this verification is performed, the second important result is the analysis of the evolution of the pressure field in the VV stressing the study on the presence of high pressure spots, in particular on the walls of the VV for the verification of the structural safety limit.

1.3.3 Outline of this thesis

This thesis is divided in three main chapters:

1. The first chapter is devoted to the identification of the strategy to be used for the CFD study of an in-VV LOCA: all the main phenomena occurring during the accident are modelled checking that the experimental results present in literature are the same as the simulated ones. The main phenomena are the development of a free jet and its impaction with a cylindrical wall. Thus, it is of main importance the choice of the right turbulence model and the number of prism layers that guarantees a good wall treatment. A deep study is also performed on the moving front of the jet and on the algorithm implemented so that the mesh "follows" the jet. The last part of the chapter is about the generalization of the algorithm for any under expanded jet made with a parametric study of the variables present in the algorithm.

2. In the second chapter the accidental conditions present in DEMO in-VV LOCA are applied to two simplified VV geometries. These simulations are performed taking into account all the information obtained from Chapter 1. The results obtained in this chapter can be divided in two main lines: the first one aimed at comparing the 0D results with the numerical esults regarding physical parameters averaged on the entire domain and the second line aimed at the investigation of the presence of pressure peaks on the walls of the VV for a preliminary safety assessment.

3. The third chapter presents a summary of the results and comments on the goodness of a 0D approach in accidents like this taking into account the results obtained through the CFD approach.

Chapter 2

Identification of the strategy for the case study

During the first phase of the accident an under expanded jet develops in the VV due to the high pressure difference between the BB and the VV. As the expansion proceeds, the moving jet reaches the internal wall of the VV and impinges on it. For the identification of the strategy to be used in the final simulations, different parameters must be set correctly in order to be sure that the results obtained are validated against experimental results and have a physical meaning. Three different aspects of the simulation are studied separately:

- Turbulence model: chosen comparing experimental data against a CFD steady state analysis of a free jet in an open domain modelled with different turbulence models.
- Wall treatment: the number of prism layers on the cylindrical surface on which the jet impinges is chosen comparing experimental data against a CFD steady state analysis of a free jet impinging on a cylindrical wall.
- Moving front meshing strategy: set properly with a comparison of experimental data against a CFD unsteady analysis of a free jet in an open domain.

2.1 Choice of the turbulence model: test case 1

The choice of the turbulence model is a key point for the CFD analysis of free jets in open domains: in the first part of a study conducted by Novembre et al. [22], Ansys Fluent code is validated comparing CFD results with the experimental ones obtained by Eggins et al. [7]. The same procedure is followed using STAR-CCM+ in this thesis. A 2D axis-symmetric, steady state simulation is performed using different turbulence models for the definition of the most accurate model for this kind of study.

2.1.1 Experimental test case

Eggins et al. provide velocity measurements in an under-expanded supersonic free jet of air [7]. The experimental set-up is showed in Figure 2.1. The jet is produced by a converging nozzle with an exit diameter of 2.7 mm rigidly connected to an air reservoir maintained at a pressure p_1 of 6.7 bar and at a temperature T_1 of 293 K. This work gives velocity profiles in several cross-sections downstream of the nozzle exit and the velocity profile along the jet axis (until a maximum distance from the nozzle equal to 80 mm). The jet develops in atmospheric conditions with a pressure p_0 equal to 1 bar and at a temperature T_0 equal to 293 K.

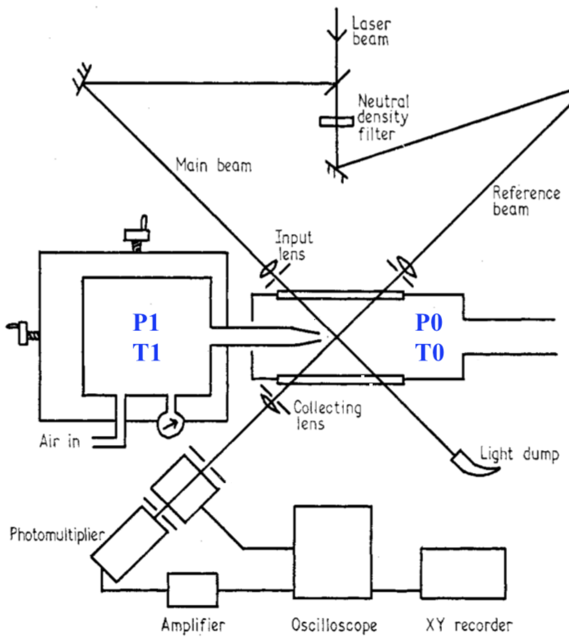

FIGURE 2.1: Test case 1: schematic of the experimental apparatus.

The following CFD study is based on the conditions summarized in Table 2.1

TABLE 2.1: Test case 1: experimental conditions.

p_1	p_0	T_1=T_0
6.7 bar	1 bar	293 K

2.1.2 CFD set-up

A steady state CFD analysis with the same physical parameters of the experimental case (see 2.1) is performed following the same procedure used by Novembre et al. [22]. A coupled implicit solver is used to solve the governing equations for mass, momentum and energy and the results from the three different turbulence models (standard k-ϵ, two-layer ϵ and ω SST) are compared. The computational domain is showed in Figure 2.2 and the main CFD parameters are summarised in Table 2.2.

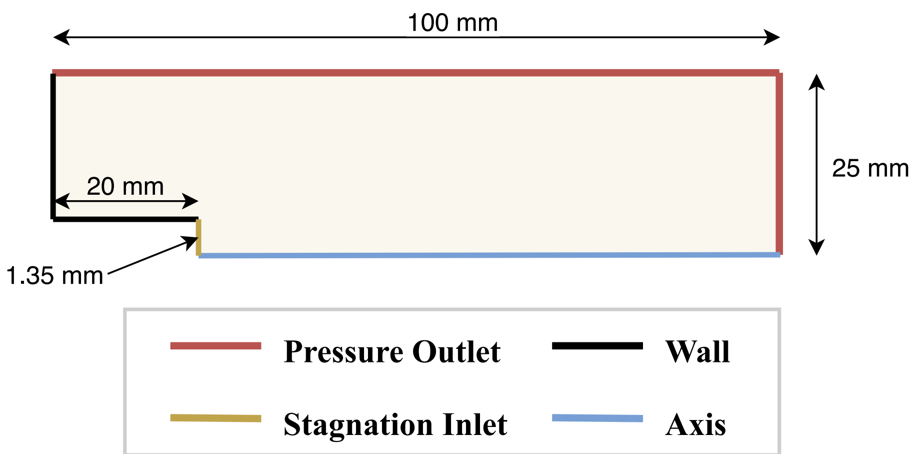

FIGURE 2.2: Test case 1: CFD domain.

TABLE 2.2: Test case 1: CFD boundary and initial conditions.

Reservoir pressure (p_1)	6.7 bar
Expansion chamber pressure (p_0)	1 bar
Reservoir and expansion chamber temperature	293 K
Jet and expansion chamber composition	air (100%), ideal gas

In order to obtain a good resolution near the jet maintaining a low computational time, an adaptive mesh refinement based on velocity gradient is implemented. Figure 2.3 shows the final mesh distribution once convergence is reached: the black area is characterised by a finer mesh.

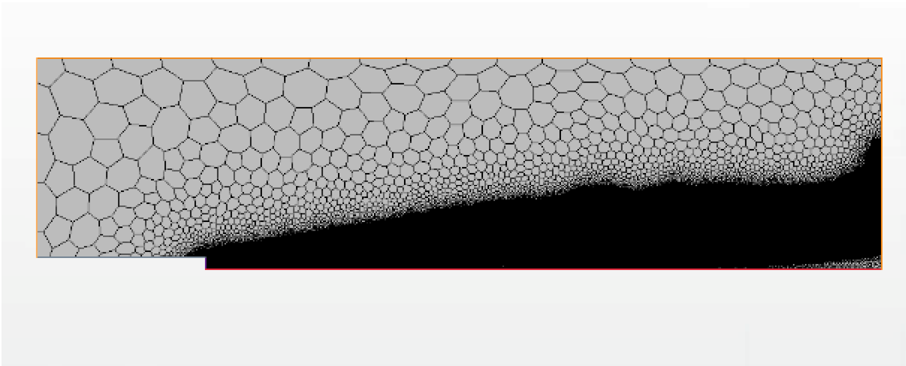

FIGURE 2.3: Test case 1: mesh at convergence.

A brief summary of the main characteristics of the polyhedral mesh used is present in Table 2.3

TABLE 2.3: Test case 1: Mesh characteristics.

Base size	Refined base size	# of cells
5 mm	0.03 mm	850k

2.1.3 Results and comparisons

This section hosts the main numerical results obtained with the three turbulence models used. Figure 2.4 shows a qualitative comparison between the steady-state final velocity fields obtained (the domain is mirrored with respect to the axis). The general jet shape seems to be very similar for each case.

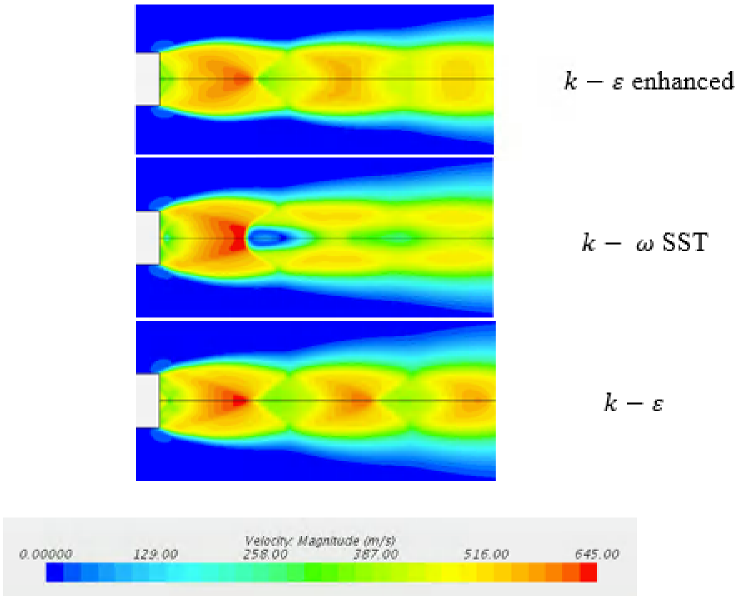

Figure 2.4: Test case 1: steady state jet velocity fields: graphic comparison between the three models.

The reliability of the numerical results is checked comparing the three CFD axial velocity profiles with the experimental one (Figure 2.5(a)) and verifying the similarity between their evolutions and that of a typical under expanded jet [22] (Figure 2.5(b)).

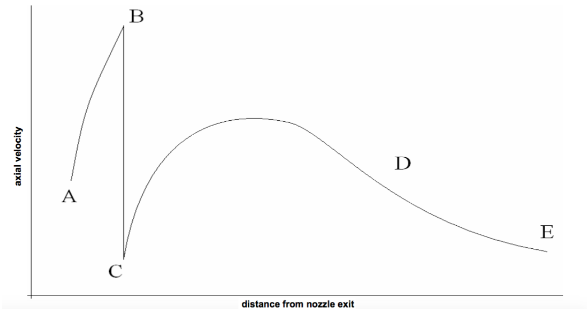

(a)

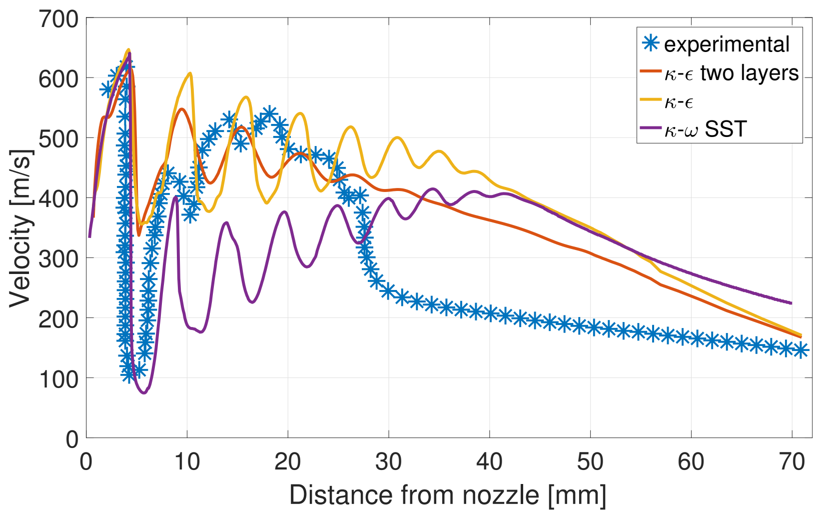

(b)

FIGURE 2.5: Test case 1: comparison between the theoretical expected axial velocity profile (a) and the experimental and numerical axial profiles (b).

According to Novembre et al. [22] the axial velocity profile can be divided into four intervals:

1. first interval (A-B): supersonic expansion with a fast acceleration up to a maximum axial velocity.

2. second interval (B-C): presence of the shock characterised by a sudden velocity drop.

3. third interval (C-D): bell-shaped velocity profile.

4. fourth interval (D-E): dispersion of the jet and reaching of an asymptotic velocity.

In the first interval the results from each models are in good agreement with the experimental data. As far as the second interval is of concern, the velocity drop after the shock is foreseen by each model. However, only k - ω SST reproduces correctly the minimum velocity in line with the experimental data as showed in Figure 2.5(b). In the third interval, the numerical results are characterised by an oscillating behaviour with constant frequency and diminishing amplitude until an asymptotic velocity is reached in the fourth interval. The oscillations present in the third interval have nothing in common with the experimental data except from the results obtained with the k - ω SST which is the only model capable of foreseeing correctly at least the first oscillation. In the last interval the three numerical results are quite similar but differ from the experimental solution even though the trend seems to reach the experimental asymptotic velocity. Another quantitative comparison between experimental and numerical results is conducted analysing the radial velocity profile on two plane sections orthogonal to the axis of the domain located 0.2 mm upstream and downstream the shock position (see Figure 2.6). Also in this study, upstream the shock, numerical results with the three different models are very similar and in good agreement with the experimental ones while different behaviours are found in the downstream section: the only model capable of foreseeing the correct minimum velocity in correspondence of the shock is k - ω SST as showed in Figure 2.6(b).

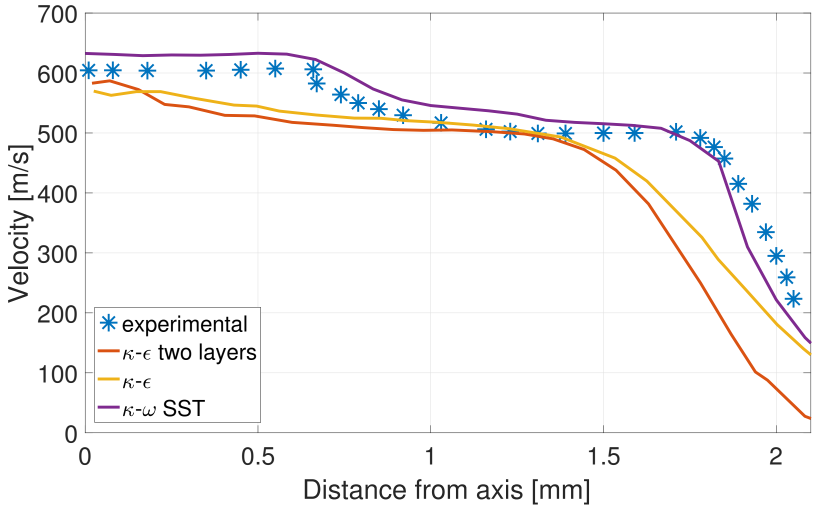

(a)

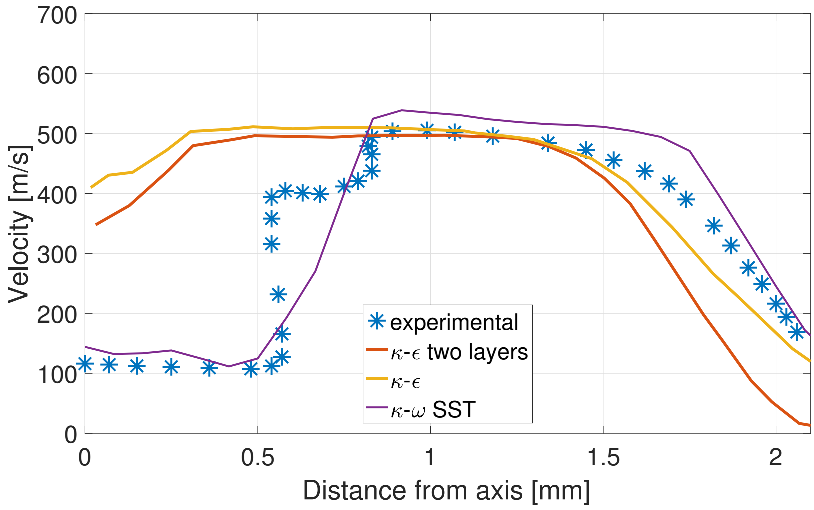

(b)

FIGURE 2.6: Test case 1: upstream (a) and downstream (b) radial velocity profiles.

Finally, Table 2.4 compares the axial coordinate of the shock obtained in the different simulations with the theoretical expected location evaluated by Equation 2.1 [14]:

$$X_{Mach} = 0.645 d_{ext} \sqrt{\frac{p_{reservoir}}{p_{discharge}}} \tag{2.1}$$

TABLE 2.4: Test case 1: theoretical, experimental and numerical shock locations.

	Shock location [mm from nozzle]	ΔX_{Mach} [mm wrt theoretical]	Err [wrt theoretical]
Theoretical	4.5	–	–
Experimental	3.9	-0.6	13.3%
κ-ϵ standard	4.7	+0.2	4.4%
κ-ϵ two-layer	4.9	+0.4	8.9%
κ-ω SST	4.3	-0.2	4.4%

The largest error is related to the experimental results, while the absolute errors related to the numerical results seem reasonable if compared to the order of magnitude of the distance.

2.1.4 ENI - POLIMI study

The aim of this paragraph is to compare the previously exposed numerical results with those obtained from the same benchmarking study performed on the commercial code FLUENT by Novembre et al. in a study [22] conducted in collaboration between Ente Nazionale Idrocarburi (ENI) and Politecnico di Milano (POLIMI) aimed at the analysis of a free jet expansion from methane pipelines. The two equation models, k-ϵ , k-ϵ RNG and k-ω SST are tested on a quadrangular mesh of 24000 cells in a set of simulations characterised by the same domain, set-up of boundary and initial conditions, physics model and solver as stated in subsection 2.1.2. As a general conclusion of their study, the k-ω SST is considered to be the best model to properly represent the experimental jet results.

Figure 2.7 shows a comparison between experimental and numerical velocity profiles both from FLUENT and STAR-CCM+ with the implementation of the RANS k-ω SST model: for each velocity profile taken into consideration, the general shape of the numerical results is in line with the expected from experiments. The only critical point is the minimum velocity foreseen by the ENI-POLIMI study in correspondence of the shock which has a negative value. More generally, the two numerical results are very similar being affected by the same amplitude of distortions from the experimental data and being characterised by the same peculiarities and differences.

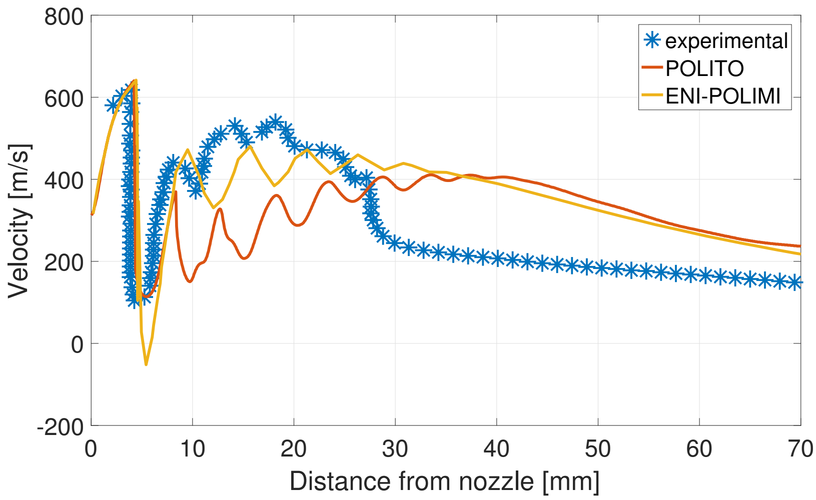

(a) Axial velocity profile.

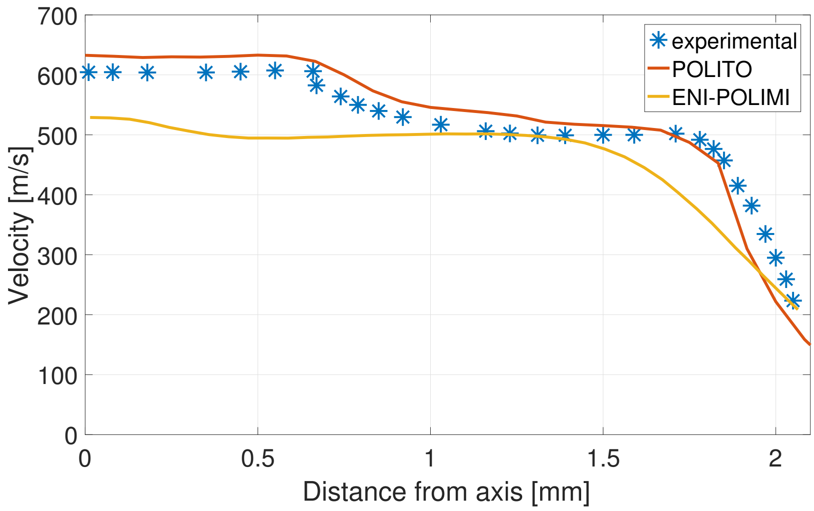

(b) Upstream radial velocity profile.

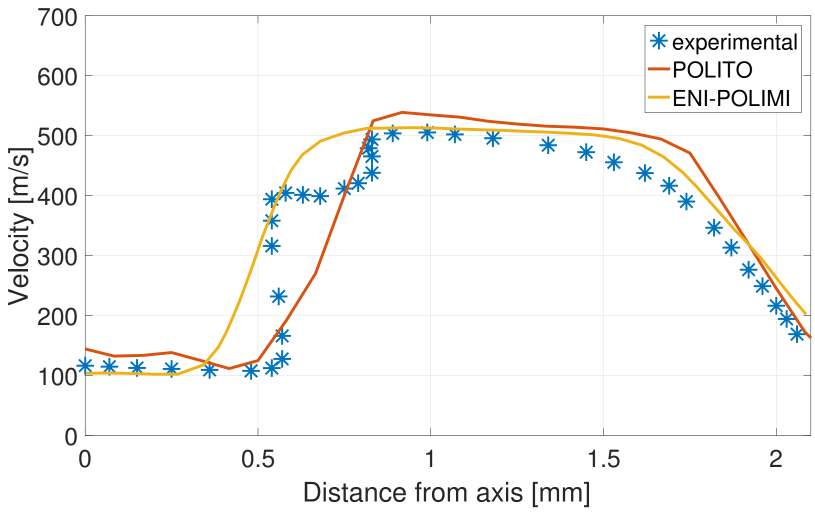

(c) Downstream radial velocity profile.

FIGURE 2.7: Test case 1: comparison between results from POLIMI and from STAR-CCM+.

2.1.5 Conclusions

As a first result of this chapter, the k-ω SST turbulence model is considered to be the most adequate for the analysis of an under-expanded free jet mainly for its ability to at least qualitatively reproduce the after-shock performance of the jet (see Figures 2.5(b) and 2.6(b)). Radial velocity profiles upstream and downstream the shock are confirmed to be in line with the experimental data but some criticalities are present in the jet intervals far away from the nozzle: the presence of velocity oscillations can cause misrepresentations of the velocity field on that restricted area of the domain. Downstream the oscillatory zone, the velocity values approach again those expected from the experimental data. The comparison between the results by the ENI-POLIMI study and STAR-CCM+ present in Figure 2.7 shows little differences allowing to state that STAR-CCM+ has been validated against experimental data as well as FLUENT.

2.2 Wall treatment: test case 2

After the release of helium from the blankets, the jet expands and moves towards the cylindrical wall opposite to the break, impinges on it causing an increase of pressure that can lead to the structural failure of the VV walls. Since the evaluation of the pressure peaks on the walls is one of the aim of this thesis, it is necessary to test the capability of STAR-CCM+ to properly evaluate the interaction between an expanding jet and a cylindrical wall. The fluid zones near the walls are meshed with the Prism Layer Mesher, whose aim is to decrease the mesh base size introducing layers of progressively smaller size towards the wall enhancing the wall treatment and the caption of the near wall flow [26].

An experimental study focused on a jet-wall interaction is conducted by Tabrizi in his PhD thesis [27] with a particular focus on the pressure distribution on a cylindrical surface subjected to an impinging jet. The experimental pressure distribution is compared with the one obtained through a 3D, steady in time CFD simulation of the previously introduced experimental set-up and a parametric study is executed changing the number of prism layers on the wall.

2.2.1 Experimental test case

Amongst all the different experimental cases analysed by Tabrizi, the most similar to the in-VV LOCA is taken into consideration. In the experimental domain, showed in Figure 2.8, a jet of air exits from a circular nozzle with a diameter (D_N) equal to 5 mm and impinges on a cylinder located at a distance (H) of 100 mm. The cylinder diameter, (D) is equal to 25 mm. The nozzle connects a pressurized chamber at an initial pressure $\mathrm{p_1}$ equal to 3.75 bar and the jet is discharged in the expansion chamber in atmospheric conditions $\mathrm{p_0}$ equal to 1 bar. The pressurized and the expansion chamber are at the same temperature $\mathrm{T_0}$ equal to 293 K. Table 2.5 summarizes the main experimental data.

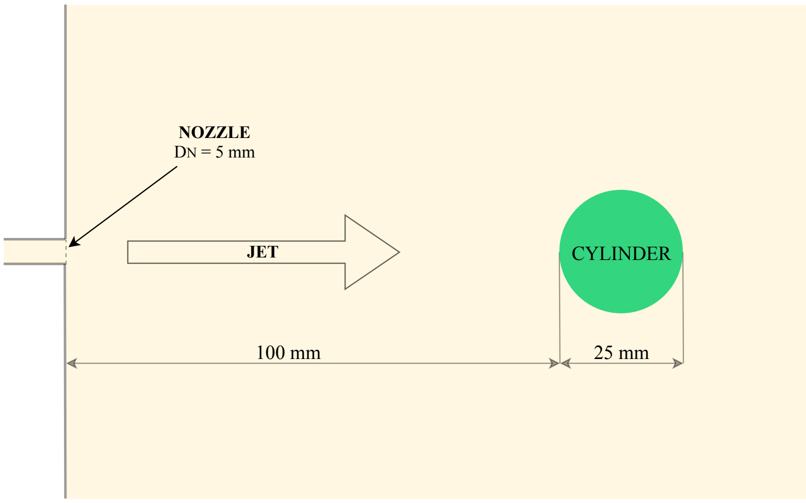

FIGURE 2.8: Test case 2: schematic of the experimental apparatus.

TABLE 2.5: Test case 2: experimental conditions.

p_1	p_0	T_1=T_0
3.75 bar	1 bar	293 K

2.2.2 CFD set-up

The experimental conditions are simulated on a 3D steady state CFD study using a coupled implicit solver and a k-ω SST turbulence model. Only a quarter of the domain is simulated, as showed in Figures 2.9 - 2.11, due to its symmetric properties. The main conditions are outlined in Table 2.6.

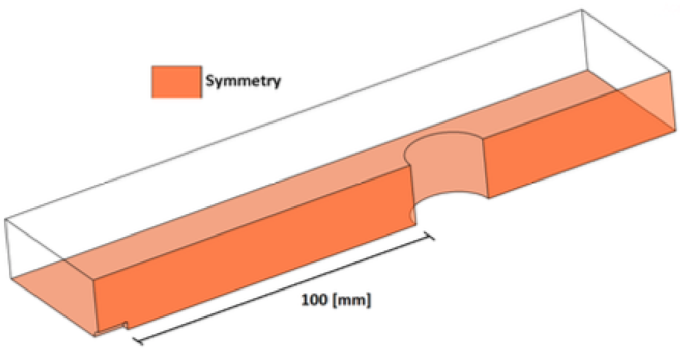

FIGURE 2.9: Test case 2: CFD domain and location of the symmetry boundary condition. Image from [24]

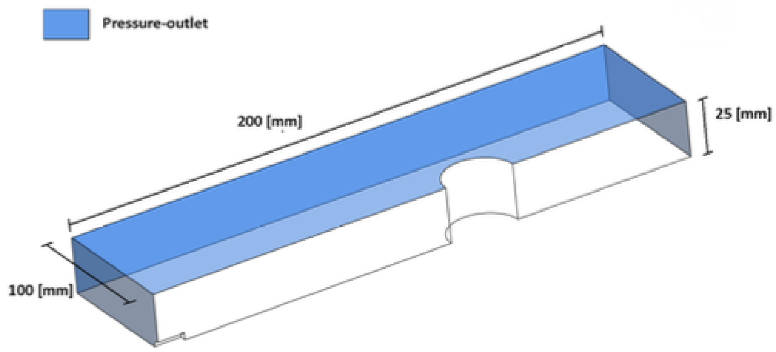

FIGURE 2.10: Test case 2: CFD domain and location of the pressure outlet boundary condition. Image from [24]

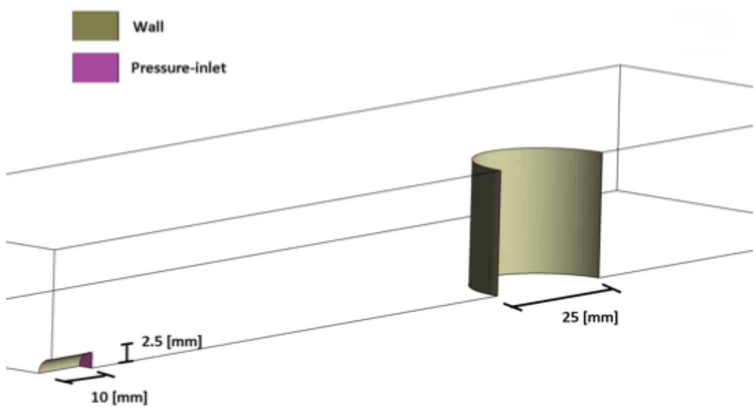

FIGURE 2.11: Test case 2: CFD domain and dimensions. Image from [24]

TABLE 2.6: Test case 2: CFD boundary and initial conditions.

Pressurized chamber pressure (p_1)	3.75 bar
Expansion chamber pressure (p_0)	1 bar
Pressurized and expansion chamber temperature	293 K
Jet and expansion chamber composition	air (100%), ideal gas

2.2.3 Mesh

In order to reduce the computational time, an adaptive mesh refinement based on the velocity gradient is implemented. Figure 2.12 shows the mesh distribution at the end of the simulation. The main characteristics of the polyhedral mesh used are outlined in Table 2.7.

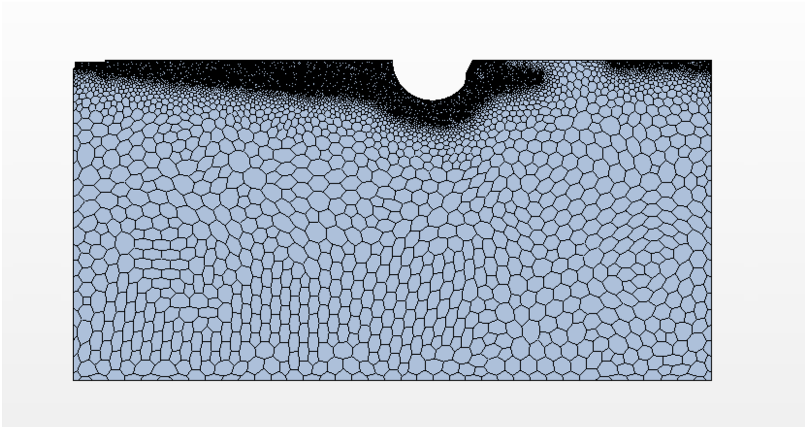

(a) View from above.

(b) Frontal view.

Figure 2.12: Test case 2: mesh at convergence.

Table 2.7: Test case 2: mesh characteristics.

Base size	Refined base size	# of cells
5 mm	0.25 mm	350k

2.2.4 Results and comparisons

A suitable wall treatment is necessary to properly solve the boundary layer near the wall and to capture the physical phenomenon occurring during a fluid-to-wall interaction. In this study, the number of prism layers is changed in order to perform a parametric study on the pressure distribution on the cylindrical wall. Tabrizi expresses the pressure distribution in terms of pressure coefficient defined as the pressure normalization with respect to the maximum value occurring on the surface. Figure 2.13 shows the experimental pressure coefficient compared to the simulated one obtained with 5, 10 and 15 prism layers.

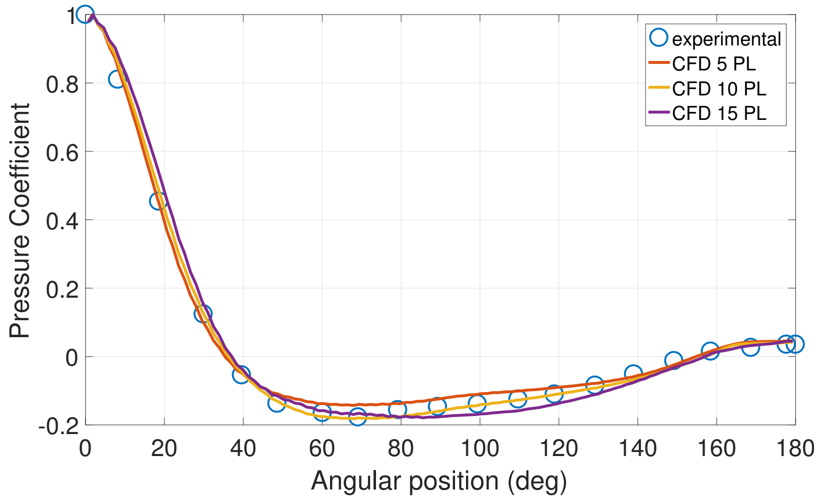

FIGURE 2.13: Test case 2: comparison between experimental and numerical results. A preliminary independence study on the number of prism layer is performed.

Since the pressure coefficients obtained with 5, 10 and 15 prism layers are affected by the same distortions with respect to the experimental result, the minimum number of prism layers (5) is chosen.

2.2.5 Conclusions

The investigation performed on the effect of the number of prism layers on the evaluated pressure coefficient confirm the capability of STAR-CCM+ to give numerical results in line with those experimentally proved. A minimum number of 5 prism layers, as also suggested by the STAR-CCM+ user guide [9], is enough to produce proper results when the interaction between a jet and a wall is of concern.

2.3 Dynamic mesh: test case 3

The last part of the benchmark of experimental results with STAR-CCM+ involves the analysis of an unsteady circular free jet [18]. In this paper, the temporal evolution of circular free jets of air is studied both experimentally and numerically with a strong focus on the development of the Mach disk. From the numerical point of view, Ishii et al. use a Finite Difference method for solving the Eulerian equation of fluid dynamic. A 2D, axis-symmetric, unsteady in time simulation is performed introducing an adaptive mesh refinement (AMR) algorithm based on Courant number. Several experimental results are compared with those obtained with the CFD study performed with STAR-CCM+.

2.3.1 Experimental test case

The experimental apparatus is showed in Figure 2.14. A stainless steel shock tube (diameter = 2 cm) with an open end (E) connects the expansion chamber chamber (C) with the high-pressure chamber (A). A low-pressure chamber (B) between chamber A and C is separated from chamber A by a diaphragm at location O. When the diaphragm is ruptured by a needle, a shock wave propagates towards C until it reaches the open end E at a Mach number equal to M_E. The evolution of the jet is analysed through Schlieren images and shadowgraphs which are taken by a synchronized photograph system.

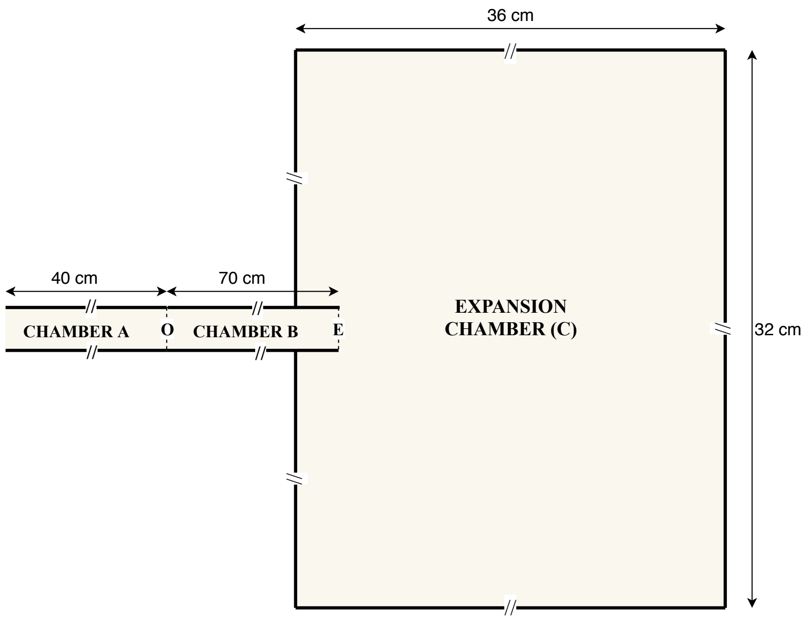

FIGURE 2.14: Test case 3: schematic of the experimental apparatus.

The benchmarked experimental initial conditions are outlined in Table 2.8, where the subscripts A, B, C and E refer, respectively, to the chamber A, B, C and the open end E.

TABLE 2.8: Test case 3: experimental conditions

p_A/p_C	T_A=T_C	p_E	M_E	p_E/p_C
50	288 K	5 bar	1.02	5

2.3.2 CFD set-up

The experimental conditions previously introduced are simulated in STAR-CCM+: the boundary and initial conditions set-up summarised in Table 2.9 are applied to an unsteady CFD simulation performed on the axis-symmetric domain sketched in Figure 2.15. It can easily be noticed that this study simulates only the fluid-dynamics from section E of the experimental domain.

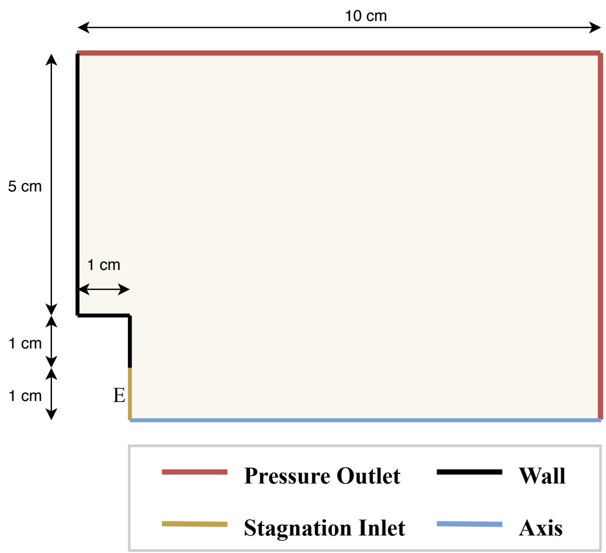

FIGURE 2.15: Test case 3: CFD domain.

TABLE 2.9: Test case 3: CFD initial and boundary conditions.

Reservoir pressure	5 bar
Reservoir temperature	288 K
Jet and expansion chamber composition	air (100%), ideal gas
Expansion chamber pressure	1 bar
Expansion chamber temperature	288 K
Turbulence model	k-ω SST
Time-step	0.5 μs (coupled implicit)
Number of inner iterations (per time-step)	20
Maximum number of cells	150k

Further details on the independence studies performed in order to choose the proper number of inner iterations, time-step and grid base size are present in Appendix A.

2.3.3 Mesh

The AMR algorithm implemented in this thesis is based on the non dimensional Courant number (Co) expressed in Equation 2.2 [29].

$$Co = \frac{v\Delta t}{\Delta x} \tag{2.2}$$

From the physical point of view, Co represents the ratio between the distance travelled in the time-step Δt by an information characterised by a certain velocity v. One of the most important constraint [5, 10, 29] for the stability of a transient CFD analysis, is the Courant-Friedrichs-Lewy (CFL) condition, stating that "the full numerical domain of dependence must contain the physical domain of dependence" [4], i.e. the maximum accepted Courant number value is 1.

$$\text{CFL condition: } Co \leq 1 \tag{2.3}$$

The implementation and validation of an algorithm capable of generating a dynamic mesh that follows the jet during the entire transient is the objective of this section. Figures 2.16 - 2.18 show the coupling between the advancing mesh and the jet: it can be noticed that the CFL condition is respected on almost the entire domain.

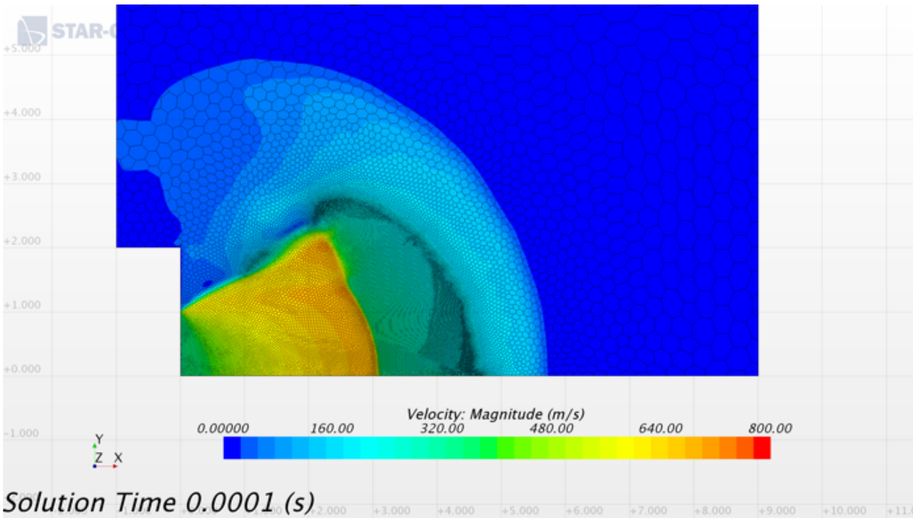

(a) Velocity field and mesh.

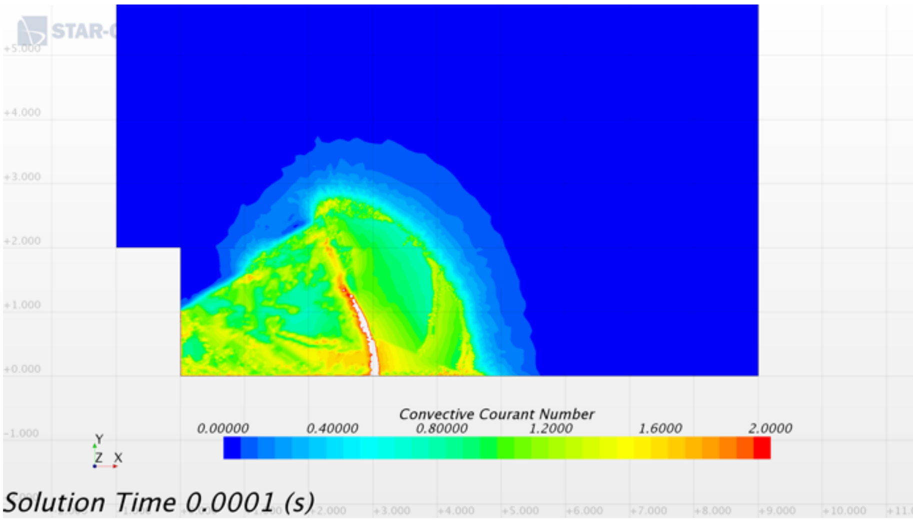

(b) Courant field.

FIGURE 2.16: Test case 3: coupling between the moving jet and the mesh at t=100 μs.

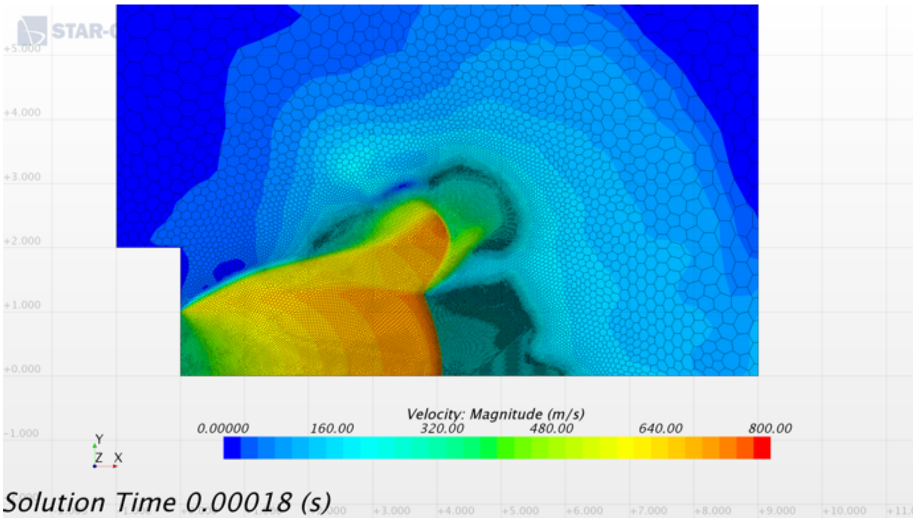

(a) Velocity field and mesh.

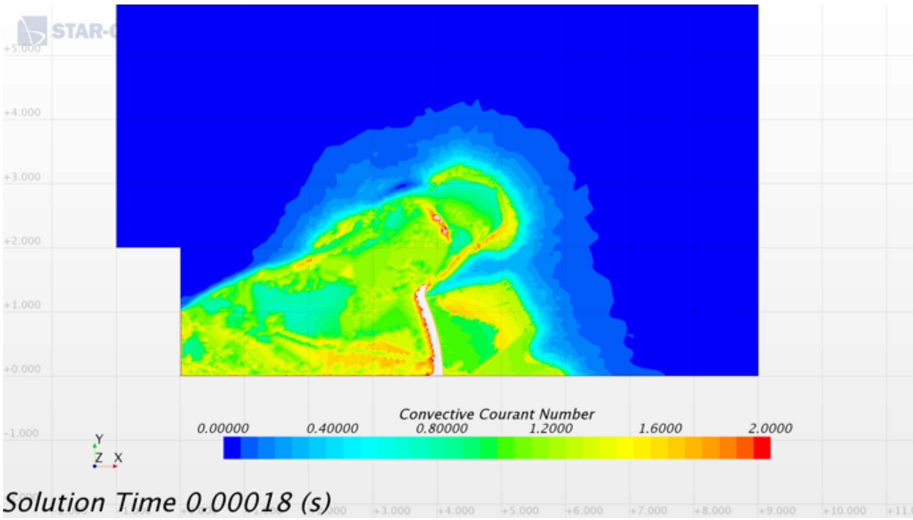

(b) Courant field.

FIGURE 2.17: Test case 3: coupling between the moving jet and the mesh at t=180 μs.

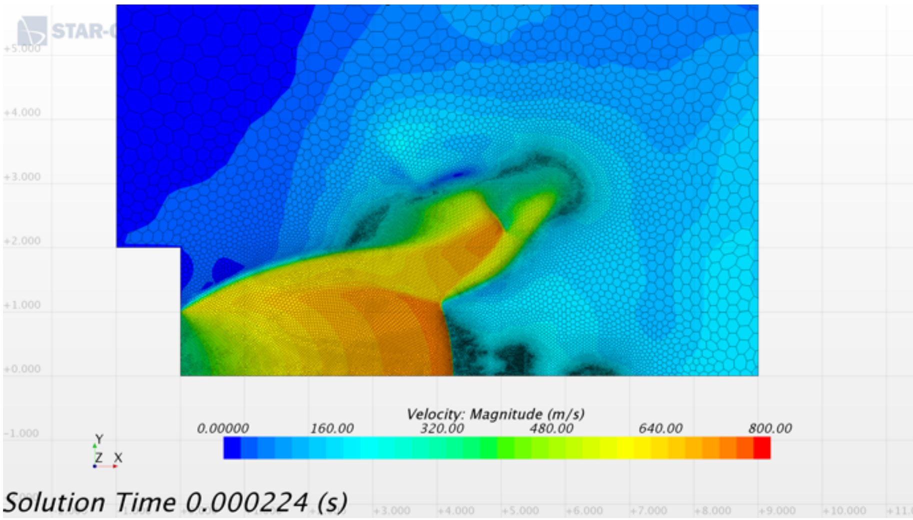

(a) Velocity field and mesh.

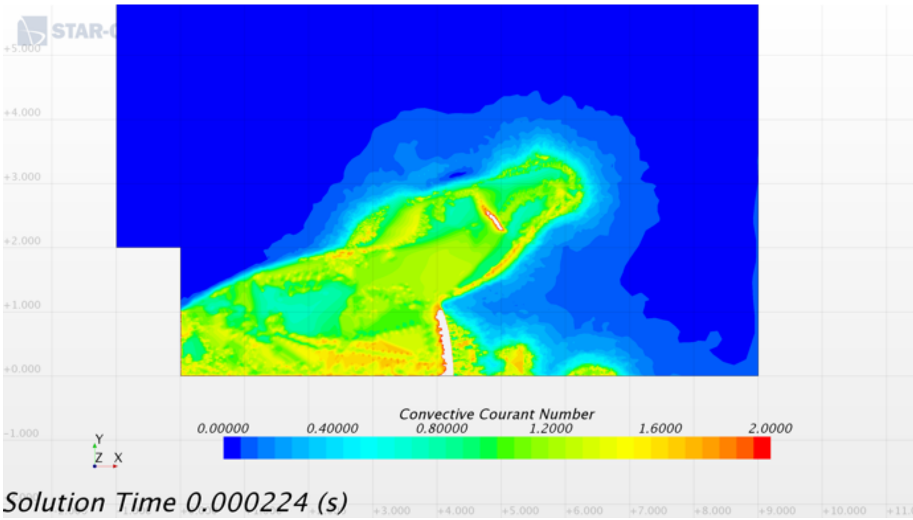

(b) Courant field.

FIGURE 2.18: Test case 3: coupling between the moving jet and the mesh at t=224 μs.

The previous figures clearly show that the algorithm uses a very fine mesh only in the most interesting region of the domain which is, in this case, the area interested by the presence of the jet. A Courant number near the unity (green color) is obtained in the entire jet-zone which is composed by all the cells characterised by a velocity higher than an arbitrary threshold value: the algorithm makes a check on the entire domain, identifies which cells must be re-meshed and assigns them the right base size that respect the CFL condition. Instead, if the cell is considered "outside" the jet, it will have the domain base size.

In a 2D domain, imposing the same size of the cell in the x and y direction

$$\Delta x = \Delta y \tag{2.4}$$

according to Zuev [29], the analytical formulation of the Courant number is:

$$Co = \frac{v_x \Delta t}{\Delta x} + \frac{v_y \Delta t}{\Delta y} \tag{2.5}$$

the cell base size is computed as

$$\Delta x = \frac{\Delta t}{Co}(v_x + v_y) \tag{2.6}$$

With a fixed time-step and Courant set to 1, the base size of each cell, if considered inside the jet, can be estimated. Finally, the logical scheme of the algorithm is showed in Equation 2.7.

AMR ALGORITHM

if (velocity > V_{thr})

$$\Delta x = \frac{\Delta t}{1}\left(|v_x| + |v_y|\right)$$

else

$$\Delta x = \Delta x_{domain}$$

end

(2.7)

Being the velocity threshold an arbitrary figure, a parametric analysis changing its value is performed: the evolution in time of maximum velocity at axis, shock location and Mach disk radius at t=150, 200 and 250 μs are checked for convergence. Table 2.10 summarises the four cases used for the parametric study performed with the same set-up explained in section 2.3.2.

TABLE 2.10: Test case 3: cases for the choice of the V_{thr}.

V_{thr}	# Cell max
0.15 V_{max}	405k
0.20 V_{max}	182k
0.25 V_{max}	70k
0.30 V_{max}	25k

As far as the location of the Mach disk is concerned, its evolution in time, at the three instants taken into consideration is showed in Figure 2.19.

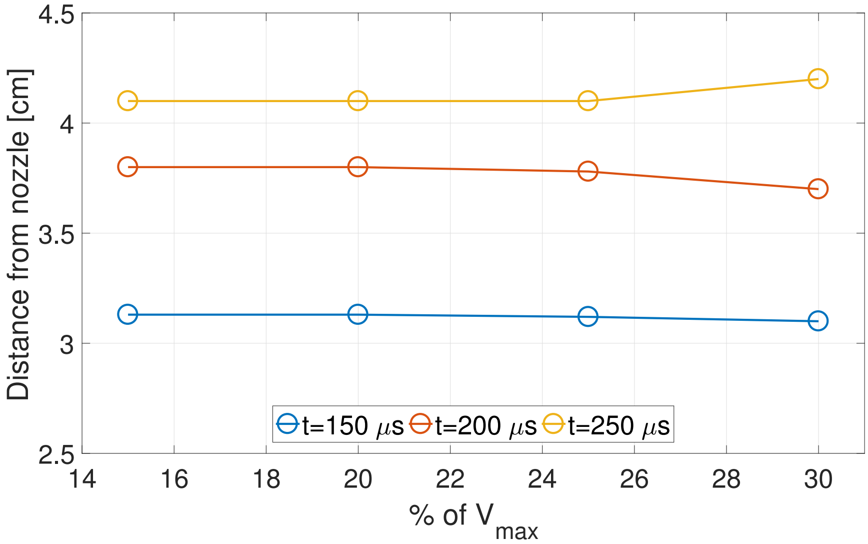

FIGURE 2.19: Test case 3: convergence of the Mach disk location in three instants of the transient.

The previous figure shows that for the three instants considered, if the velocity threshold is lower than 0.25 V_{max} the Mach disk location has reached convergence and, consequently a decrease of the V_{thr} does not give further informations.
The convergence results regarding the Mach disk radius are showed in Figure 2.20.

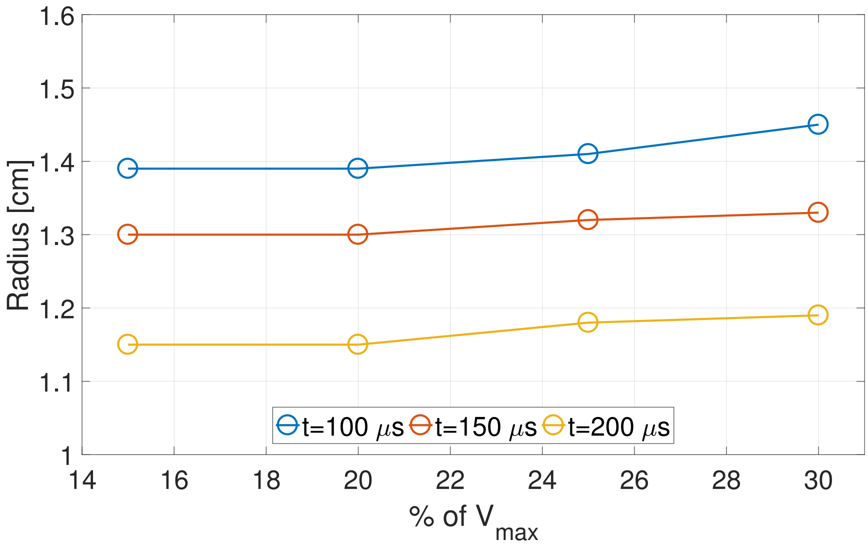

FIGURE 2.20: Test case 3: convergence of the Mach disk radius in three instants of the transient.

In this case, the disk radius values reach convergence, for the three instants considered, only if the threshold velocity is kept lower than 0.20 V_{max}. A decrease of the V_{thr} is not is not advisable since it will only increase the computational time.

Finally, a qualitative analysis is performed comparing the temporal evolution of the maximum velocity for the four cases of interest (Figure 2.21).

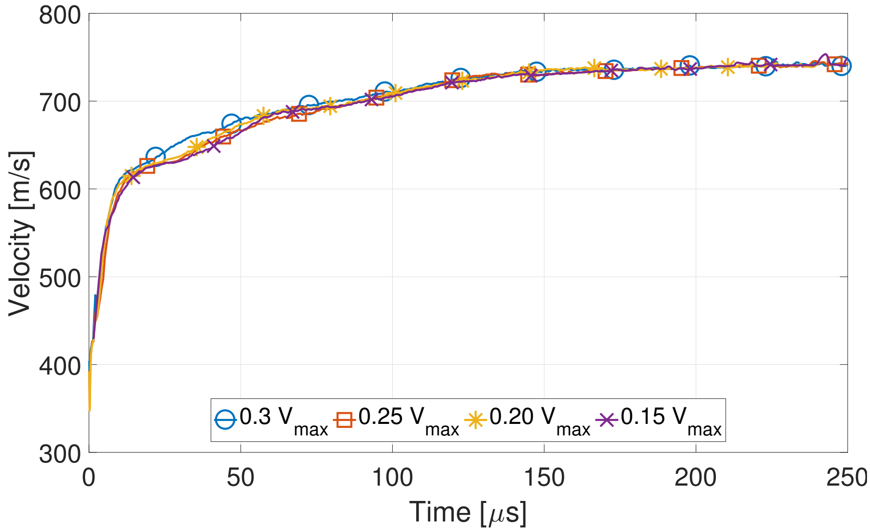

FIGURE 2.21: Test case 3: evolution of the maximum velocity changing the velocity threshold.

The qualitative analysis of the maximum axial velocity confirms that the four cases are characterised by the same maximum velocity for almost the entire duration of the transient: in the first instants, for t<50 μs, early distortions are present for the case characterised by the highest V_{thr}. The best case, which is the one characterised by the lowest V_{thr}=0.15 V_{max} (the purple line) is in line with each threshold value checked.

For the definitive choice of the threshold velocity value, it is necessary to observe that a decrease of the velocity threshold causes a fast increase of the number of cells due to the higher portion of the domain to be meshed. Moreover, these "new" portions of domain will be characterized by lower velocities with a consequent necessary lower base size yielding to an increase of the total amount of cells. A too low threshold velocity can also bring, as showed in Figures 2.22(d), 2.23(d) and 2.24(d), to re-meshed areas not characterised by relevant physical events. It can be noticed how the decrease of the velocity threshold causes an increase of the meshed domain.

As a final result of this convergence study, having considered that with a threshold value equal to 0.25 V_{max} the checked parameters converge and that the jet area is properly interested by the re-meshing action, a threshold equal to 0.25 V_{max} seems to be reasonable.

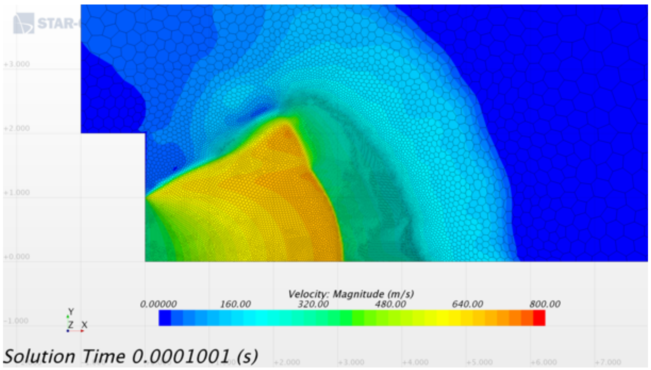

(a) V_{thr} =0.30 V_{max}

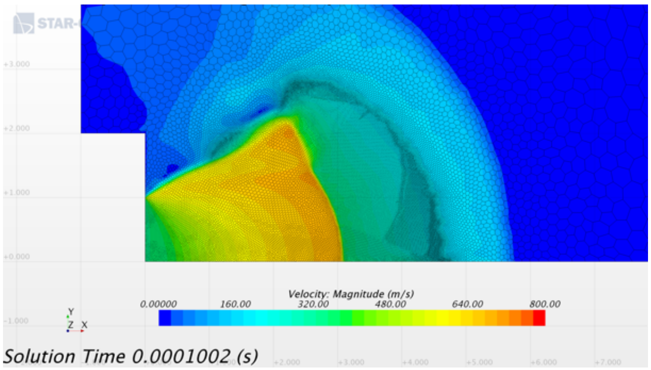

(b) V_{thr} =0.25 V_{max}

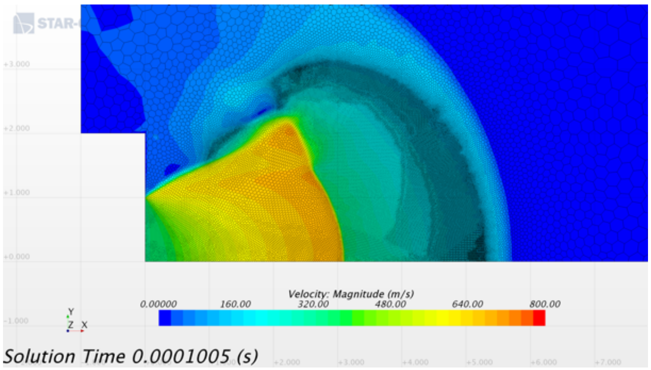

(c) V_{thr} =0.20 V_{max}

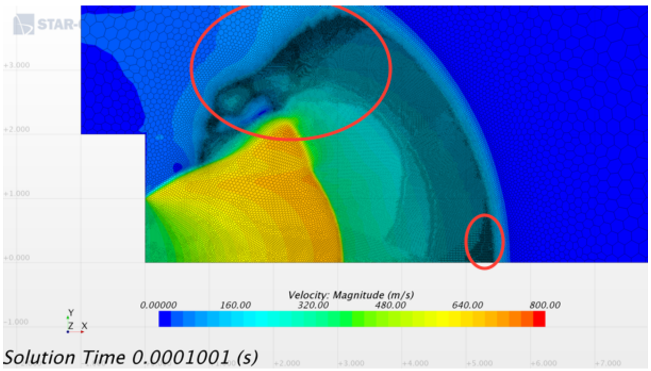

(d) V_{thr} =0.15 V_{max}

FIGURE 2.22: Mesh distribution with different velocity thresholds at t=100 μs.

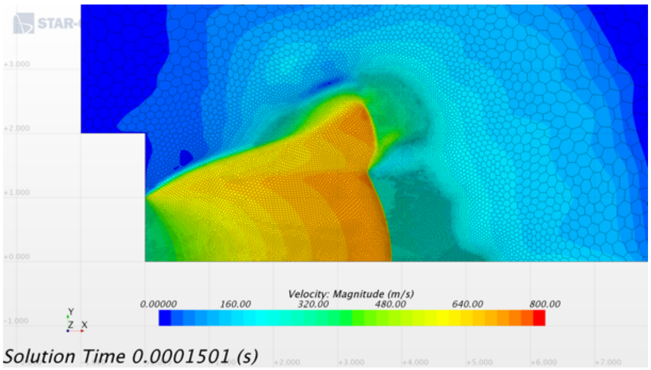

(a) V_{thr} =0.30 V_{max}

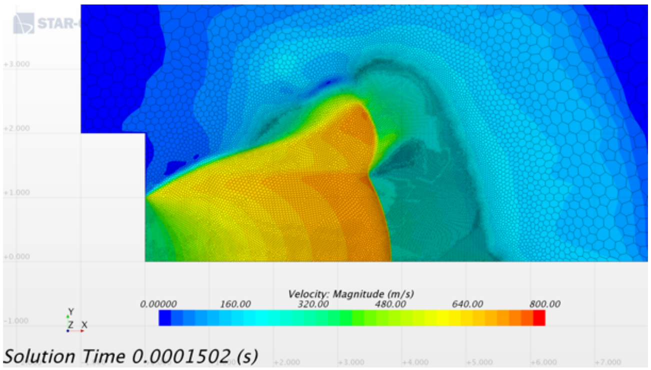

(b) V_{thr} =0.25 V_{max}

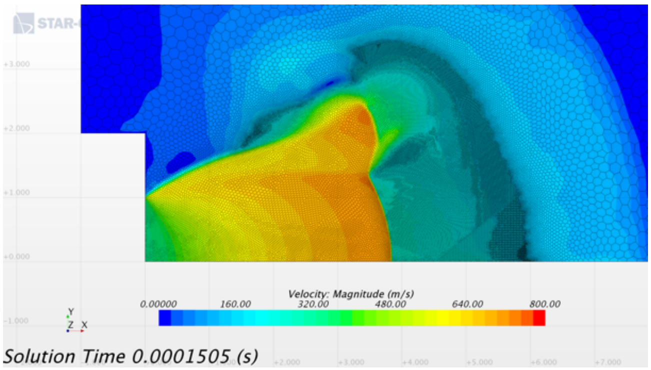

(c) V_{thr} =0.20 V_{max}

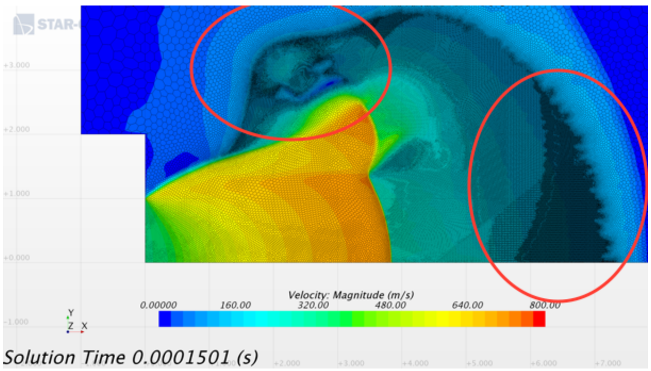

(d) V_{thr} =0.15 V_{max}

FIGURE 2.23: Mesh distribution with different velocity thresholds at t=150 μs.

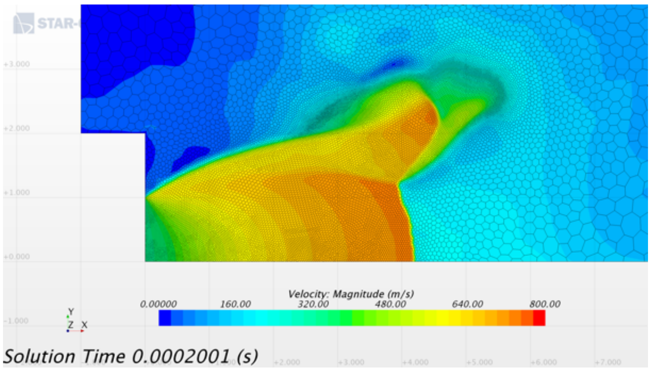

(a) $V_{thr} = 0.30\ V_{max}$

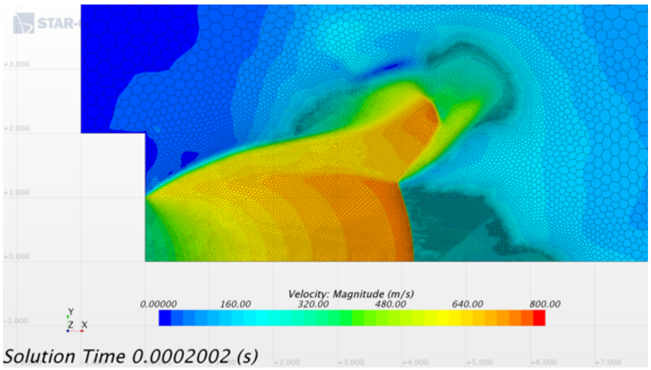

(b) $V_{thr} = 0.25\ V_{max}$

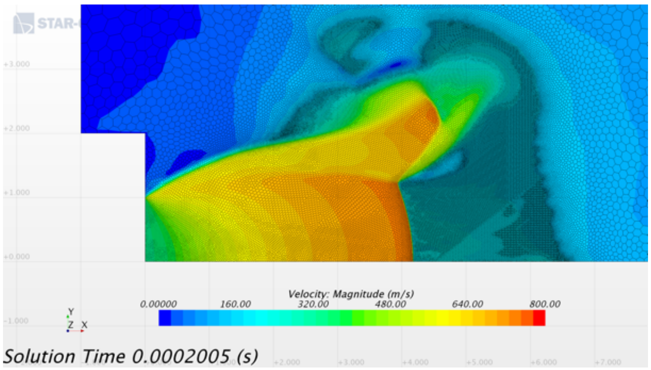

(c) $V_{thr} = 0.20\ V_{max}$

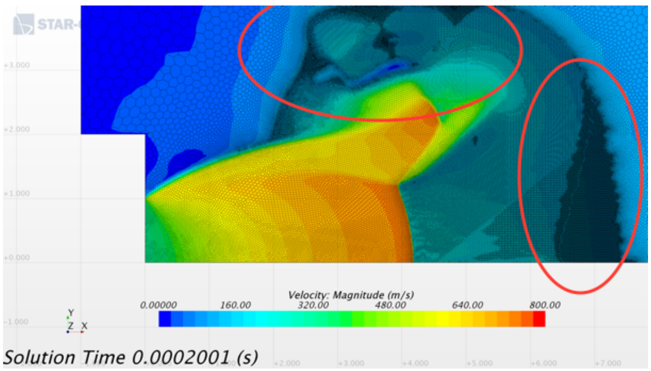

(d) $V_{thr} = 0.15\ V_{max}$

FIGURE 2.24: Mesh distribution with different velocity thresholds at t=200 μs.

2.3.4 Results and comparisons

The comparisons with the results obtained by Ishii et al. [18] are performed considering the evolution of the Mach disk location and its radius showed in Figures 2.25 and 2.26, respectively.

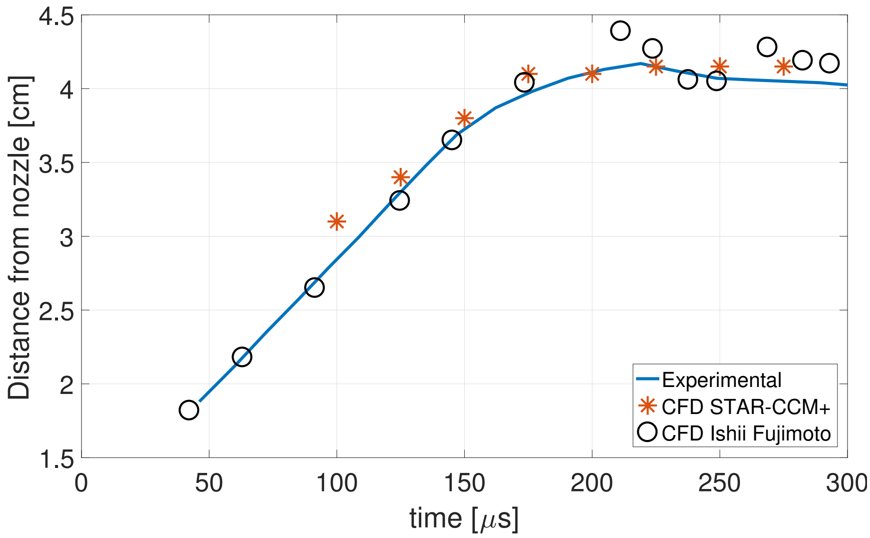

FIGURE 2.25: Test case 3: Mach disk location during the transient.

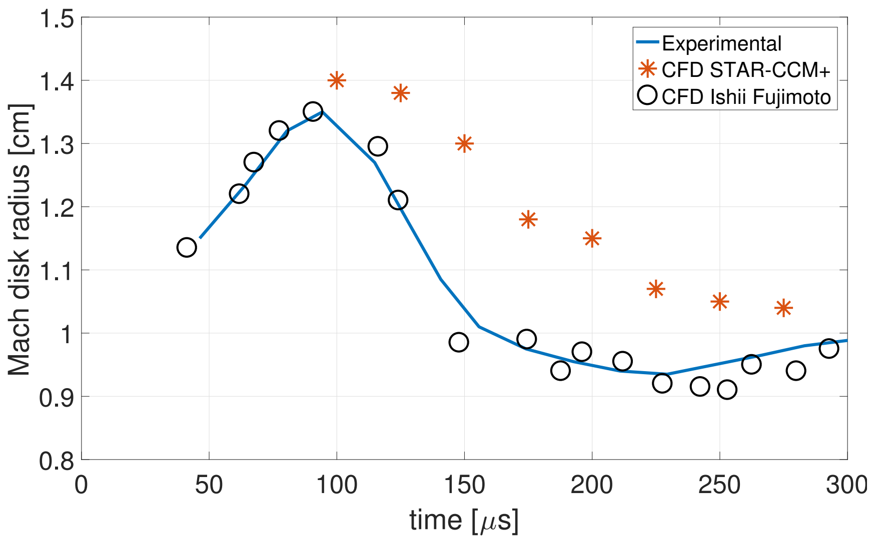

FIGURE 2.26: Test case 3: radius of the Mach disk during the transient.

A very good agreement is obtained for the motion of the Mach disk during the transient with respect to both the experimental and the numerical results. On the other hand, it can be noticed that as far as the radius of the Mach disk is of concern, this value is overestimated in the STAR-CCM+ simulations causing bigger radius by a +10%. A more accurate study must be addressed for future experimental studies.
Additional comparisons on the jet profile in three instants are shown in Figures 2.27 - 2.29 where the shape of the numerical results from STAR-CCM+ are compared with both numerical and experimental jet shape obtained by Ishii et al..

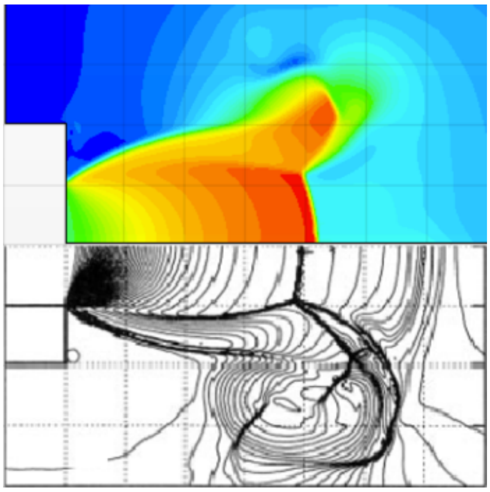

(a) STAR-CCM+ vs num.

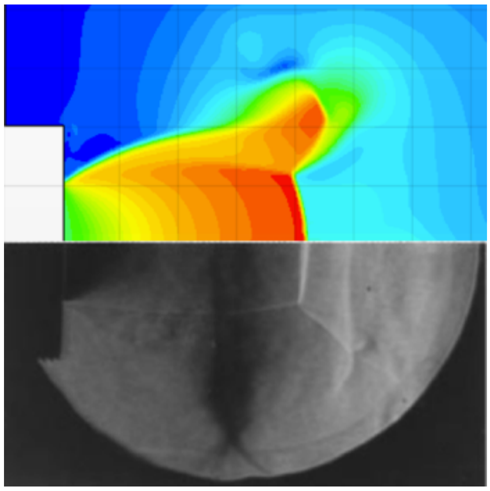

(b) STAR-CCM+ vs exp.

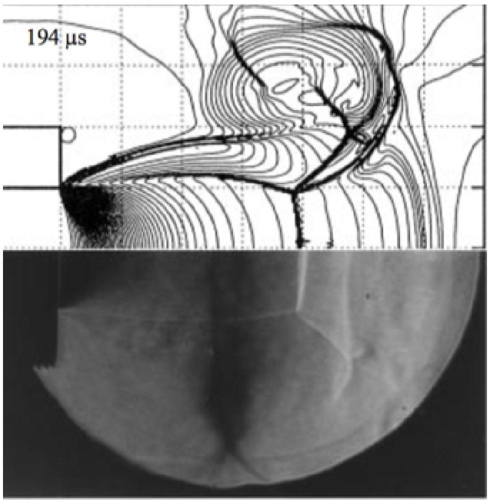

(c) Num vs exp.

FIGURE 2.27: Comparison betwenn numerical (STAR-CCM+) and Ishii et al's results (numerical and experimental) at t=194 μs.

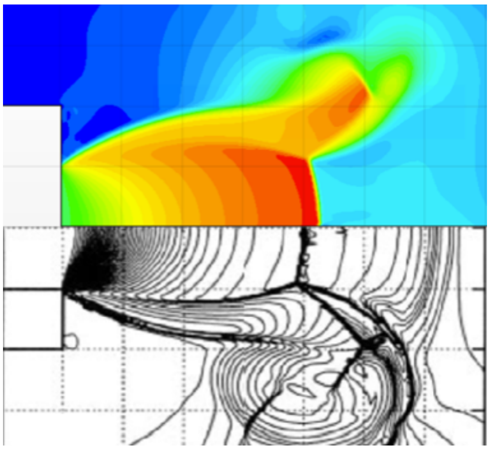

(a) STAR-CCM+ vs num.

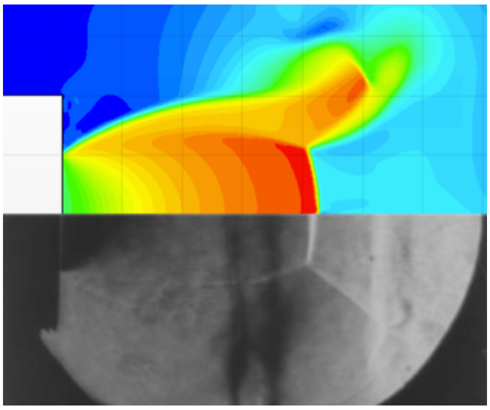

(b) STAR-CCM+ vs exp.

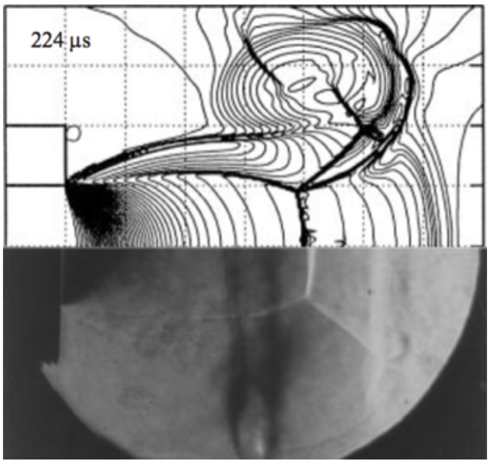

(c) Num vs exp.

FIGURE 2.28: Comparison betwenn numerical (STAR-CCM+) and Ishii et al's results (numerical and experimental) at t=224 μs.

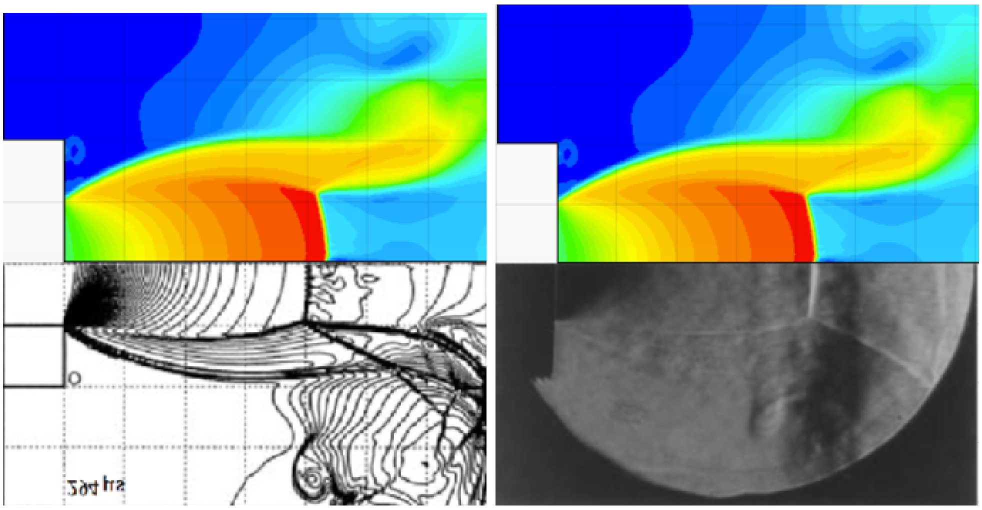

(a) STAR-CCM+ vs num.

(b) STAR-CCM+ vs exp.

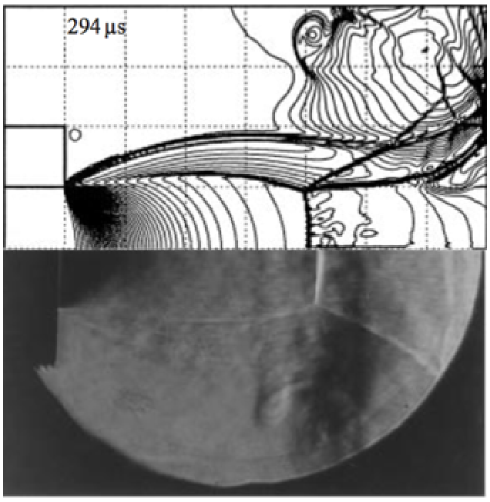

(c) Num vs exp.

FIGURE 2.29: Comparison between numerical (STAR-CCM+) and Ishii et al's results (numerical and experimental) at t=294 μs.

The previous figures confirm, qualitatively, the quantitative observations made in the previous paragraph as they show that the shock location is predicted suitably with respect to the experimental result while bigger radius are found. The order of magnitude of these dissimilarities is the same as the comparison between Ishii's numerical and experimental results.

2.3.5 Conclusions

Provided that the final scope of this thesis is not the exact prediction of the Mach disk location and dimensions but the estimation of the evolution of the jet developing in a big domain, the very small discrepancies between our results and those from literature can be considered acceptable, giving successful results for the most relevant quantities. The peak values of the velocity, the location of the shock as well as the timing are accurately reproduced by STAR-CCM+, however, the dimensions of the shock are foreseen to be bigger than in reality. Thanks to these acceptable results, STAR-CCM+ is confirmed to be reliable for the unsteady study of a jet that develops in an open domain as in case of an in-VV LOCA with a Courant based dynamic mesh refinement approach.

2.4 Application to the case study

The objective of this section is the generalization of the previously studied strategy for a general free jet which develops at very high velocity as in the case of the in-VV LOCA. Being the final simulation performed on a very big domain, this section aims at finding the optimum values for the following parameters considering the conditions of the real jet:

- Time-step and grid base size
- Optimal number of inner iterations
- Velocity threshold for the meshing algorithm

2.4.1 Assumptions

Four assumptions are introduced for the the case study:

- Initial pressure: this value is increased to 0.1 bar (instead of the real vacuum condition of 5 μPa). A too low value of pressure can not allow the use of a CFD tool since the Navier-Stokes equation is valid only if the gas is not too rarefied: further details will be provided in Appendix C [11, 26] .
- Geometry: a cylindrical layout of the VV is introduced. This choice allows to perform a 2D planar simulation of the accident with a consequent reduction of the computational time.
- Break: in order to perform a 2D planar simulation of the accident, the section studied must be representative of each section of the entire domain. This is the motivation for the choice of distributing the break along the entire height of the cylindrical VV.
- Burst Disks: to develop the simplest layout, instead of the two asymmetric locations of the Burst Disk lines (see Figure 2.32), only one BD is implemented and located opposite to the break. The surface area of the BD in the simplified layout is equal to the sum of the two BDs area present in the original design.

2.4.2 2D planar geometry

The EU DEMO reactor, showed in Figure 2.30, has a toroidal VV with a total volume of 3000 m^3 [2, 16]: the vertical and horizontal sections of the Vacuum Vessel are represented in Figures 2.31 and 2.32.

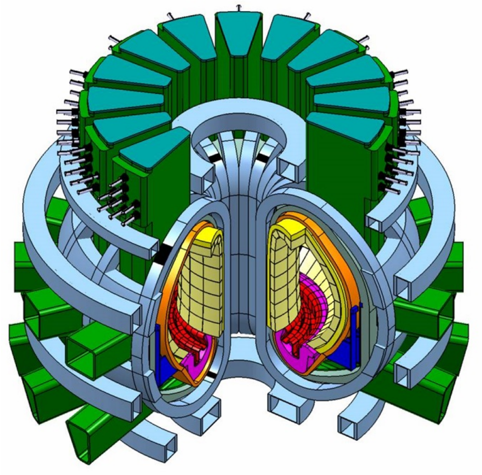

FIGURE 2.30: Rendering of the EU DEMO reactor.

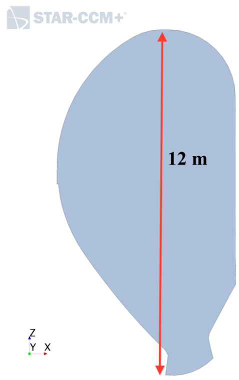

FIGURE 2.31: Frontal section of the EU DEMO VV.

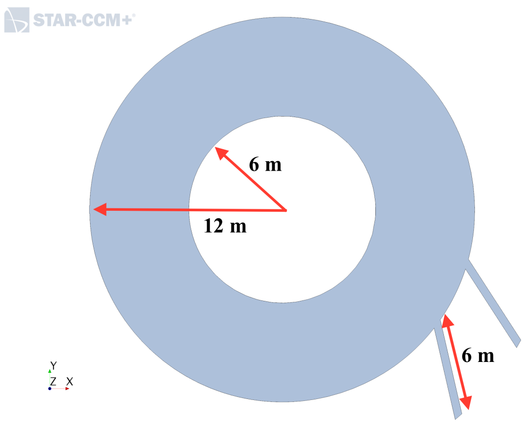

FIGURE 2.32: Planar section of the EU DEMO VV.

The simplified cylindrical layout of the VV is designed taking into account the original geometry: the dimension of the horizontal section is conserved and the total height of the cylinder is estimated keeping the total volume equal to the original one.

$$V_{VV_{cyl}} = \pi(R_{ext}^2 - R_{int}^2)H = 3000m^3 \tag{2.8}$$

the height of the cylinder, H is then equal to 8.84 m. The final simplified layout with the main dimensions is showed in Figure 2.33.

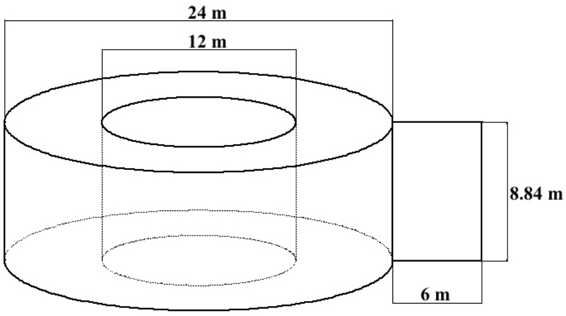

FIGURE 2.33: Simplified 3D cylindrical Vacuum Vessel.

Since the planar section of the cylindrical VV presents symmetric boundary conditions, only half of the section is simulated introducing a symmetry plane as showed in Figure 2.34 this simplification allows to reduce the computational time.

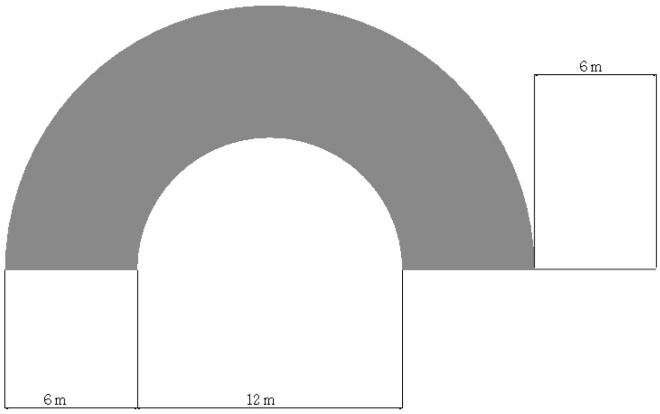

FIGURE 2.34: 2D planar section of the cylindrical VV.

2.4.3 Break and Burst Disks model

In the simulated scenario, referring to the DBA data [2, 16], the break is considered to have a discharging area from the Breeding Blanket of 0.322 m2. As the break is distributed along the entire height of the VV, the rectangular break width can be evaluated with the following expression:

$$\Delta x_{break} = \frac{A_{break}}{H} = 3.64cm \tag{2.9}$$

Given that the total surface area of the BD disk is equal to 1 m^2 [16], similarly to the procedure followed for the evaluation of Δx_{BD}, the BD width can be calculated:

$$\Delta x_{BD} = \frac{A_{BDs}}{H} = 11.3cm \tag{2.10}$$

2.4.4 CFD set-up

Figure 2.35 shows the computational domain and the condition imposed on its boundary; S2, S3, S4, S5, S6 are five sections used for the independence studies: the number indicates the distance from the nozzle (in meters). Boundary and initial conditions are summarized in Table 2.11.

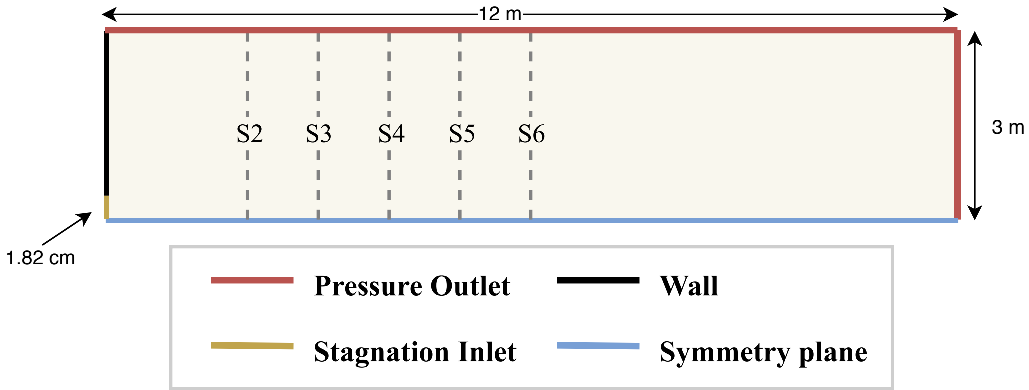

FIGURE 2.35: CFD domain for the application to the case study.

TABLE 2.11: CFD initial and boundary conditions.

Inlet pressure	80 bar
Inlet temperature	673 K
Jet and expansion chamber composition	Helium (100%), ideal gas
Expansion chamber pressure	0.1 bar
Expansion chamber temperature	293 K
Turbulence model	k-ω SST

On this simulation, the AMR algorithm introduced in section 2.3.3 is implemented and parametric studies on the grid and time-step sizes as well as on the threshold velocity are performed.

2.4.5 Grid base size and time step

Since the Courant based AMR algorithm links the time step and the grid base size (see Equation 2.3.3), the independence stud is performed on the time-step only [12]. Starting from the results of the previous sections, this study is performed with a number of inner iterations (ii) equal to 20 ii iterations and a velocity threshold of 0.25 V_{max}.

Table 2.12 shows the cases analysed and the increase of the number of cells as the time-step value is reduced:

TABLE 2.12: Cases for the time-step and grid independence study

Time-step	**# Cell max**
30 μs	8k
20 μs	15k
10 μs	50k
7.5 μs	75k
5 μs	220k

This study is limited to 5 cases because:

- in a big domain as the real final one, it is impracticable to improve a dynamic mesh algorithm with a too low time-step. The dynamic meshing is conceived as a time saving procedure, but only if the meshing time is not too high;
- already with the minimum time-step, a reasonable error is made.

The following parameters are controlled:

- Average pressure and velocity on five sections at 2, 3, 4, 5 and 6 meters from the nozzle exit (see Figure 2.35).
- Average pressure and velocity on the entire domain.

The choice of controlling average quantities at increasing distances from the nozzle is due to the requirement of ensuring that the solution converges also in a big domain. For each section considered and the entire, the average velocity and pressure evolutions in time are showed in Figures 2.36 - 2.40 and a relative error is evaluated with respect to the results obtained with the lowest time-step (case 5).

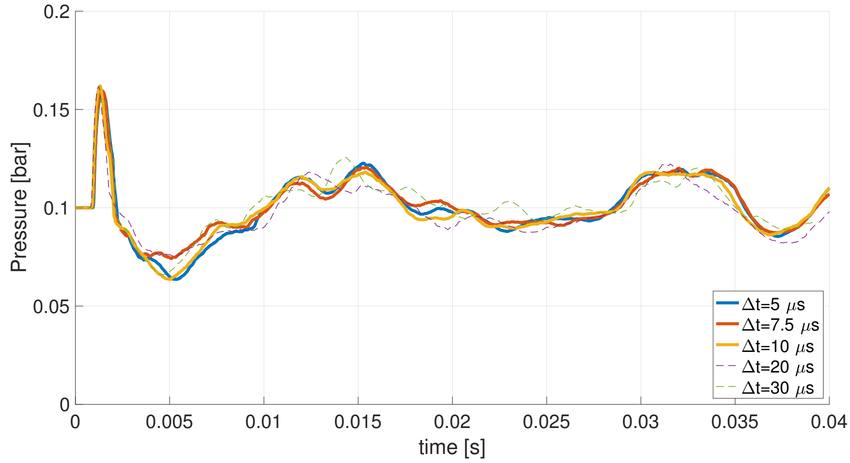

(a) Pressure.

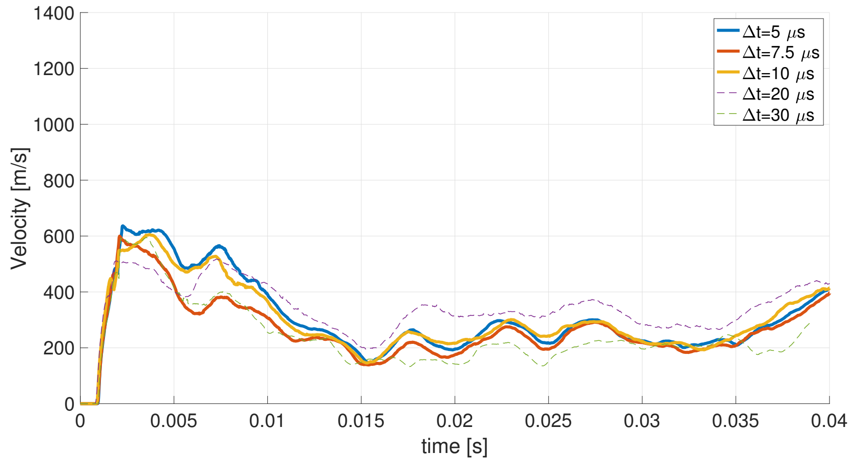

(b) Velocity.

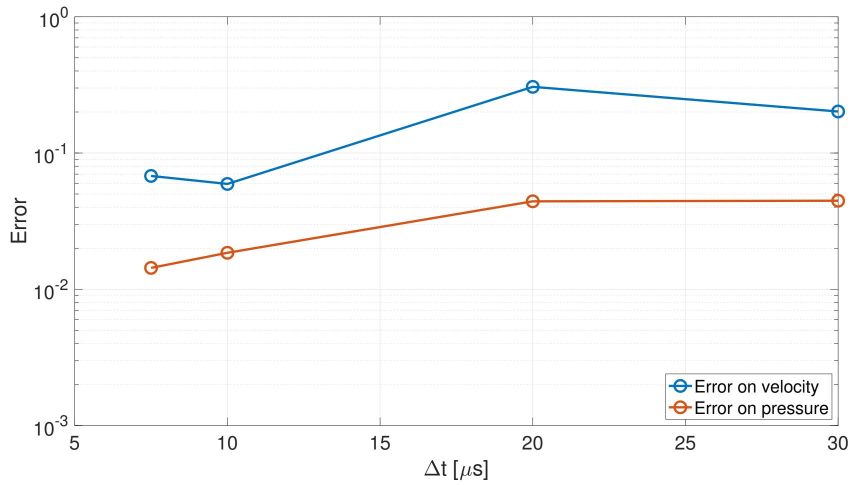

(c) Relative error with respect to case 5.

FIGURE 2.36: Average pressure (a), velocity (b) and errors (c) on a plane section located at 2 m from nozzle.

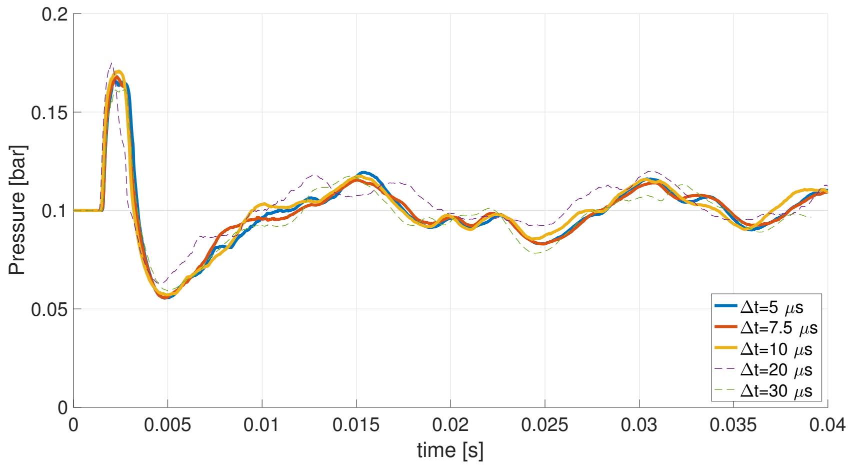

(a) Pressure.

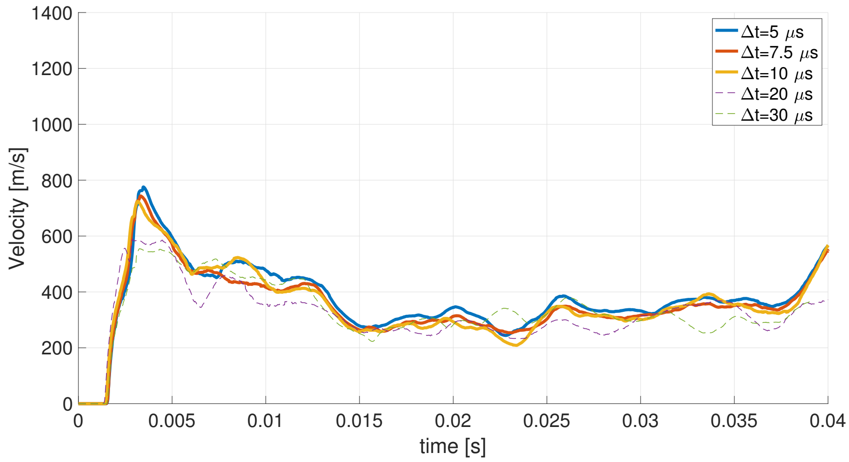

(b) Velocity.

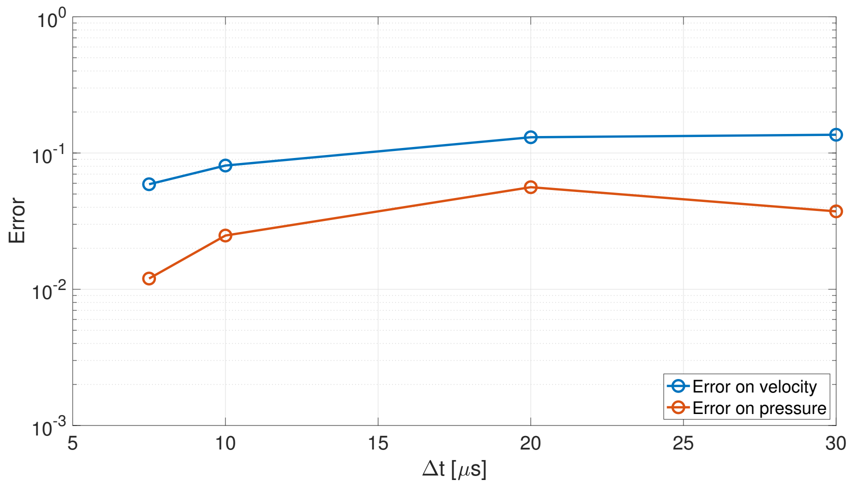

(c) Relative error with respect to case 5.

FIGURE 2.37: Average pressure (a), velocity (b) and errors (c) on a plane section located at 3 m from nozzle.

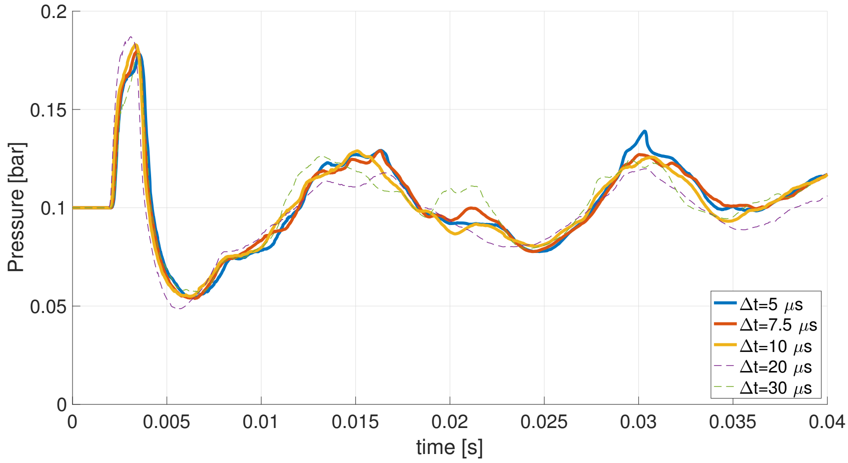

(a) Pressure.

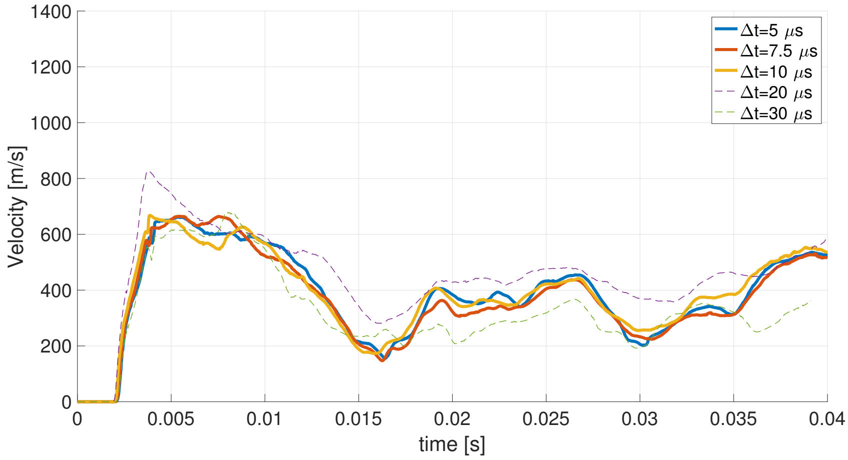

(b) Velocity.

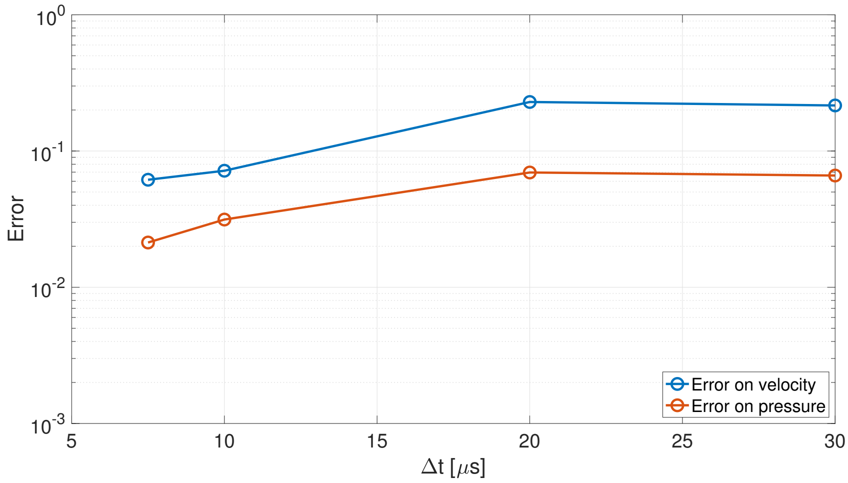

(c) Relative error with respect to case 5.

FIGURE 2.38: Average pressure (a), velocity (b) and errors (c) on a plane section located at 4 m from nozzle.

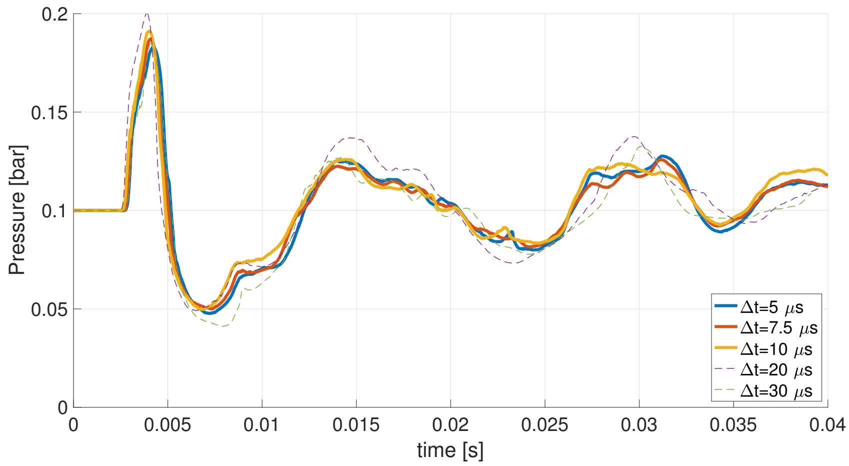

(a) Pressure.

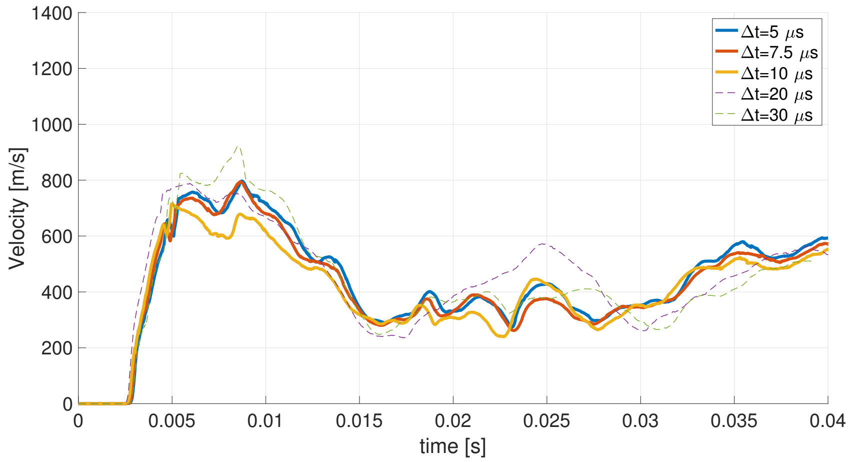

(b) Velocity.

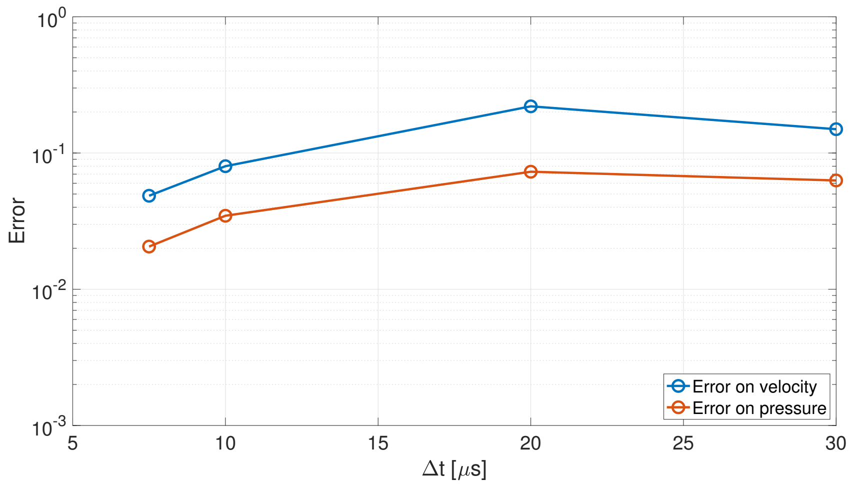

(c) Relative error with respect to case 5.

FIGURE 2.39: Average pressure (a), velocity (b) and errors (c) on a plane section located at 5 m from nozzle.

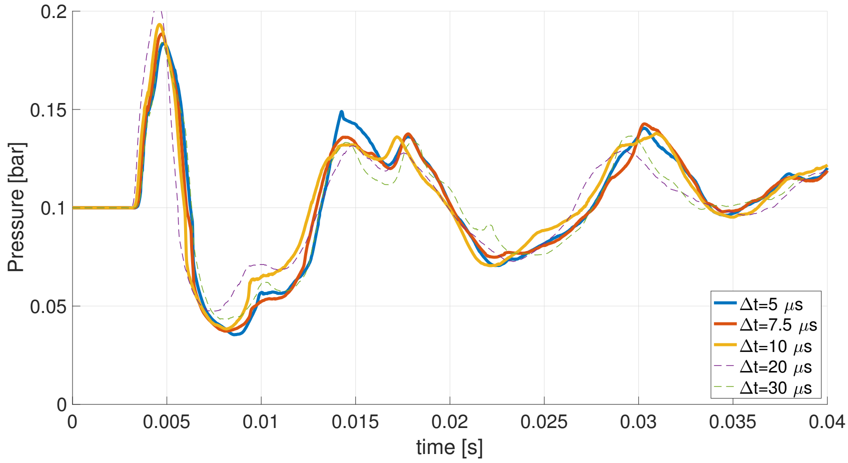

(a) Pressure.

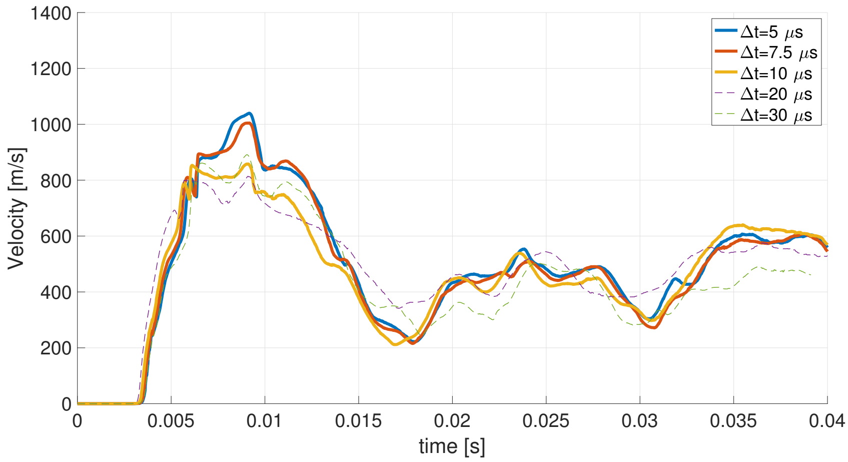

(b) Velocity.

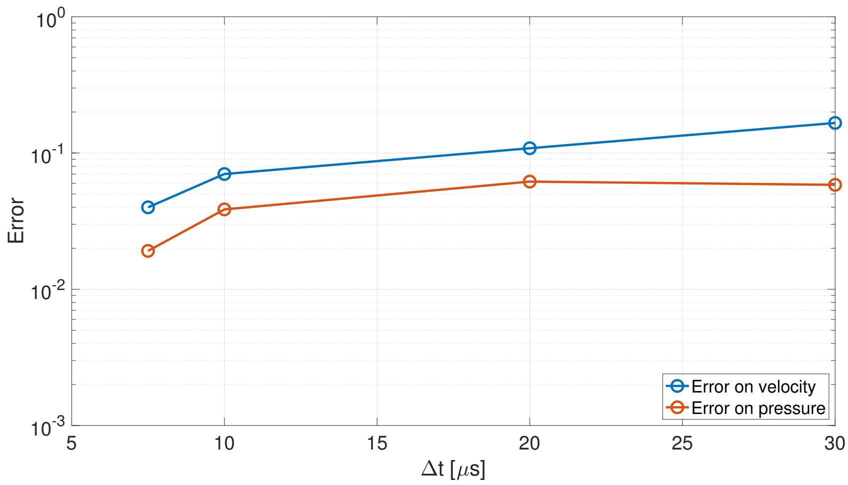

(c) Relative error with respect to case 5.

FIGURE 2.40: Average pressure (a), velocity (b) and errors (c) on a plane section located at 6 m from nozzle.

The previous figures show that except from some local distortions, the evolution in time is similar for each time-step considered. These distortions are bigger in the two cases with the highest time-steps. Velocity profiles show bigger relative errors than pressure ones but in each section, the lowest values are in the range of 10^{-2}.

Figure 2.41 shows the evolution of pressure and velocity values averaged on the entire domain.

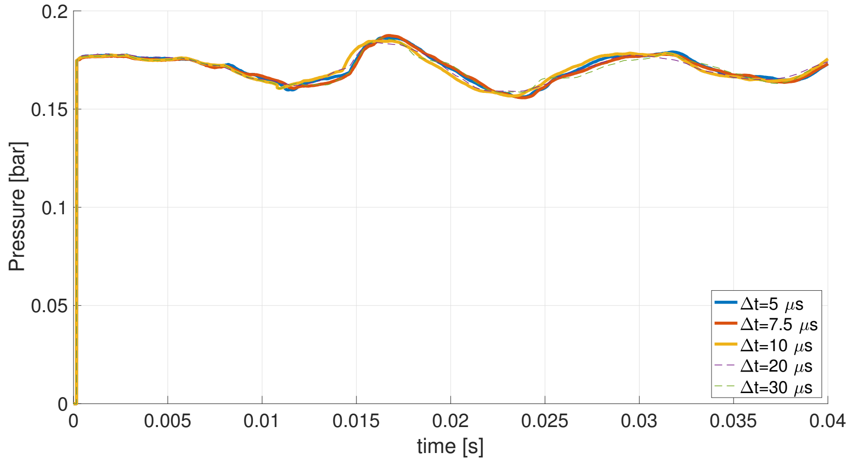

(a) Pressure.

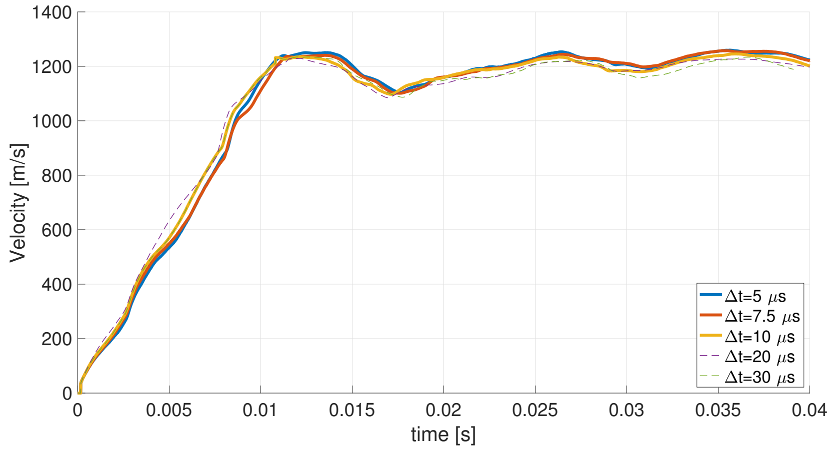

(b) Velocity.

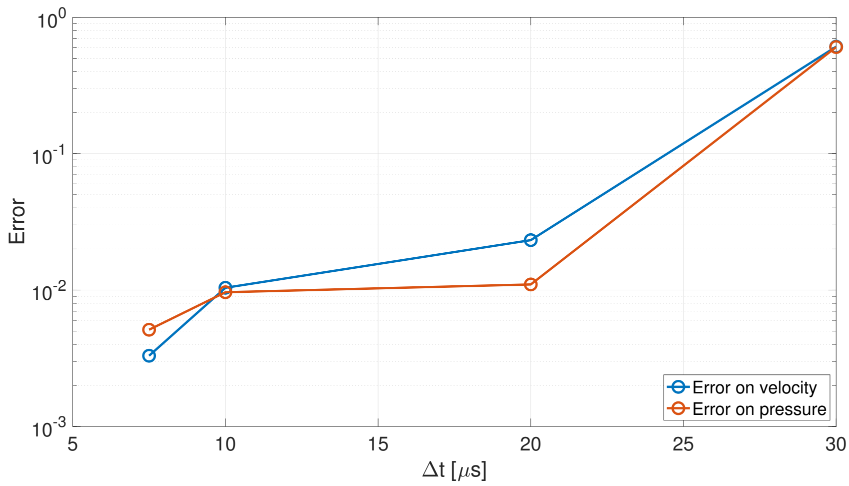

(c) Relative error with respect to case 5.

FIGURE 2.41: Average pressure (a), velocity (b) and errors (c) on the entire domain.

For what concerns domain averaged values, pressures and velocities are evolving in the same way resulting in lower error values with respect to the local ones: the error with a time-step of 7.5 μs is affected by an error of 10^{-3}, which is satisfactory for the purpose of this study.

2.4.6 Number of inner iterations

The number of inner iterations (ii) between two consequent time-steps plays a key role in a CFD simulation: a too low number of ii can bring to not-converged results, while a too high number of ii can lead to a useless increase of the computational time. The optimum number of ii is found with two parallel studies: the analysis of the order of magnitude of the residuals changing the number of ii and the analysis of the asymptotic evolution of relevant parameters as the internal cycle proceeds.

Residual analysis

In STAR-CCM+, the evolution of the residuals related to the following variables can be analysed:

- Continuity
- Specific Turbulent Dissipation Rate - Sdr
- Turbulent Kinetic Energy - Tke
- X-Momentum
- Y-Momentum
- Energy

A residual represents the degree to which the discretized equation is satisfied. Between two successive iterations the residual is the normalized difference between the two values: a low residual implies a converged solution for that quantity. However, while it is true that the residual quantity tends toward a small number when the solution is converged, the residual monitors cannot be relied on as the only measure of convergence. It is advisable to monitor quantities of engineering interest, such as integrated forces, pressure changes, or mass flow rates as well as the residuals [26]. In this study, the same simulation is performed with 10, 20, 30, 50, 100, 200 and 300 inner iterations; the time-step is 7.5 μs (as a result of the previous section of this chapter) and the velocity threshold is 0.25 V_{max}. For each simulation, at t_1=0.005 s and t_2=0.010 s, an internal cycle is run and the evolution of each residual is recorded. The order of magnitude of the residuals and the minimum number that guarantees convergence is analysed.

Table 2.13 summarises the results of the residual analysis.

TABLE 2.13: Minimum number of inner iterations that guarantees convergence for each residuals at the two analysed instants.

	Number of minimum ii that guarantees convergence	
	$\mathbf{t}_1$	$\mathbf{t}_2$
Continuity	3	3
Specific Turbulent Dissipation Rate - Sdr	15	16
Turbulent Kinetic Energy - Tke	16	19
X-Momentum	2	2
Y-Momentum	3	3
Energy	2	2

Only the two residuals that converge with a higher number of ii are studied in detail: Figures 2.42 and 2.43 show the evolution as the inner cycle proceeds for the Sdr and Tke residuals at the two instants analysed.

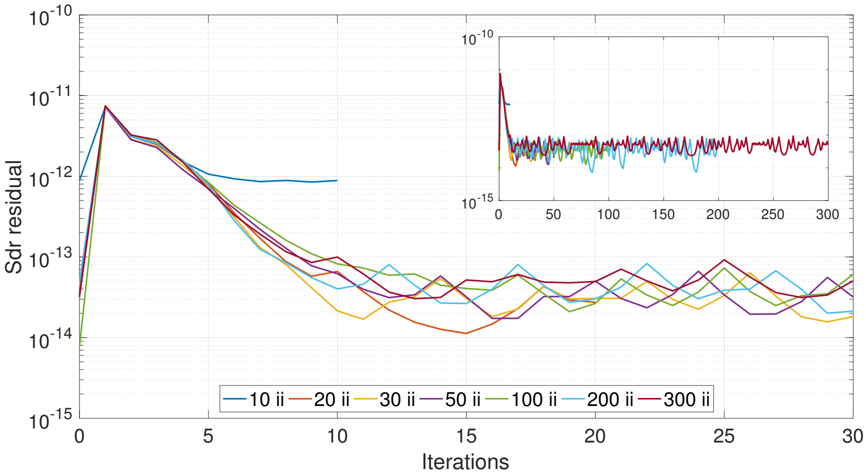

(a) t=0.005 s

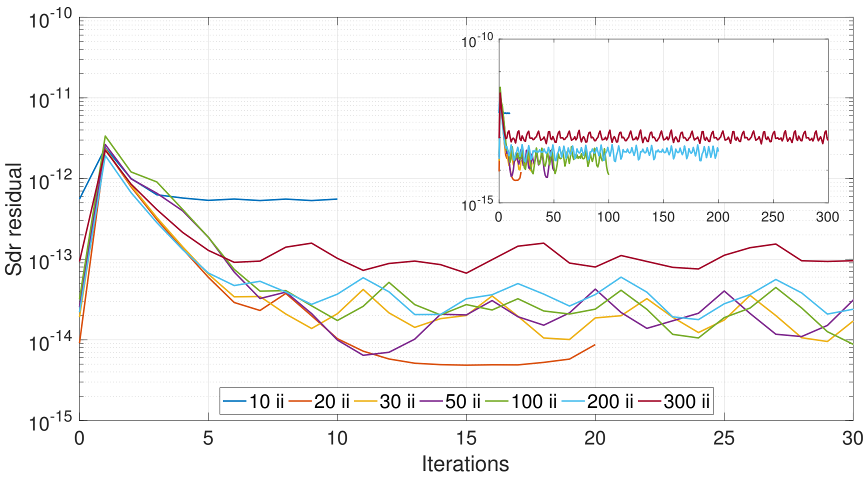

(b) t=0.010 s.

FIGURE 2.42: Specific Turbulent Dissipation Rate residuals evolution in two instants.

The Specific Turbulent Dissipation Rate residuals reach an oscillating converged value after almost 16 inner iterations in both the instants analysed. The simulation performed with 10 inner iterations has higher residuals but their values are very small being in the order of 10−12. The order of magnitude of the residuals do not change as the transient proceeds: it is the same at t_1 and t_2.

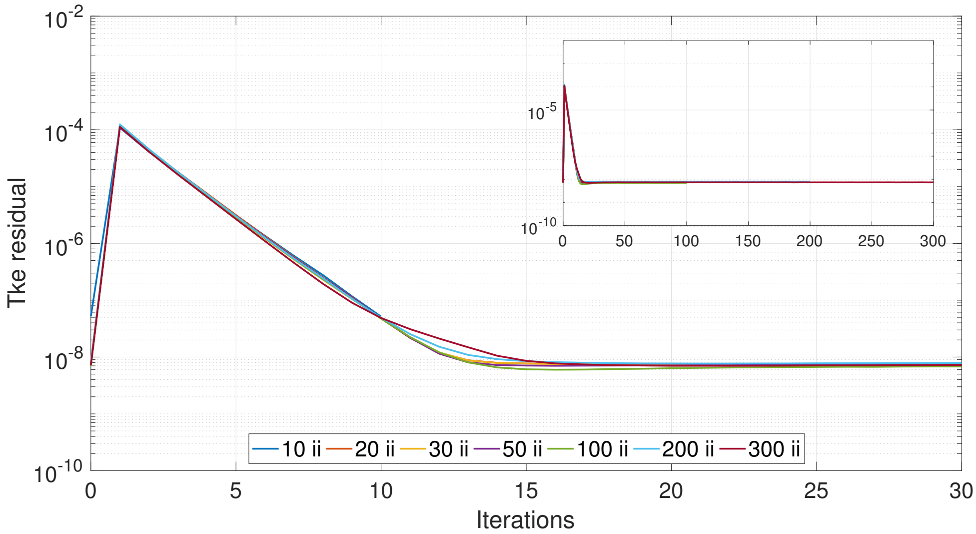

(a) t=0.005 s

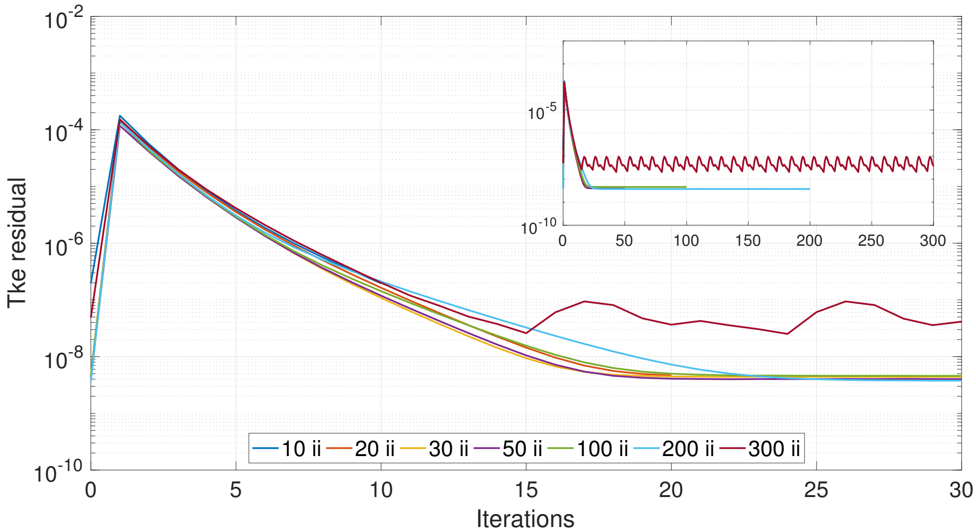

(b) t=0.010 s.

FIGURE 2.43: Turbulent Kinetic Energy residuals evolution in two instants.

The Turbulent Kinetic Energy residuals reach a converged value after almost 19 inner iterations in both the instants analysed. Also the simulation performed with 10 inner iterations has the same order of magnitude of the residual equal to the others. The order of magnitude of the residuals do not change as the transient proceeds: it is the same at $t_1$and t_2.

As a conclusion to this study, Tke and Sdr are considered to be the most critical residuals since they reach convergence in the two instants analysed after 15-20 inner iterations, while the convergence of the other residuals is achieved quite immediately within the first 5 inner iterations. The second part of this section about the number of inner iterations must be analysed taking into account this result.

Asymptotic study

A time-saving procedure for stopping the inner iterations when the time-step has reached convergence is suggested on the online guide [13]: at each inner iteration, a STAR-CCM+ built-in function checks whether a parameter (or more) has reached convergence by analysing its evolution within the last 15 ii and evaluating an error through Equation 2.11.

$$Err = \frac{|max - min|}{Average_{last15ii}} \tag{2.11}$$

The monitored parameter(s) is considered converged if its error computed by 2.11 is lower than a certain arbitrary value. For this study, the parameters checked are the average pressure, the average velocity and the maximum velocity on the symmetry axis of the domain. In order to decide which arbitrary value to set as maximum accepted error, a parametric study is performed with 3 different errors (0.01, 0.001 and 0.0001) and the number of the inner iteration at which the constraint is respected is showed. This check is performed at three different instants of the simulation characterised by 300 inner iterations: 0.005 s, 0.010 s, 0.015 s.

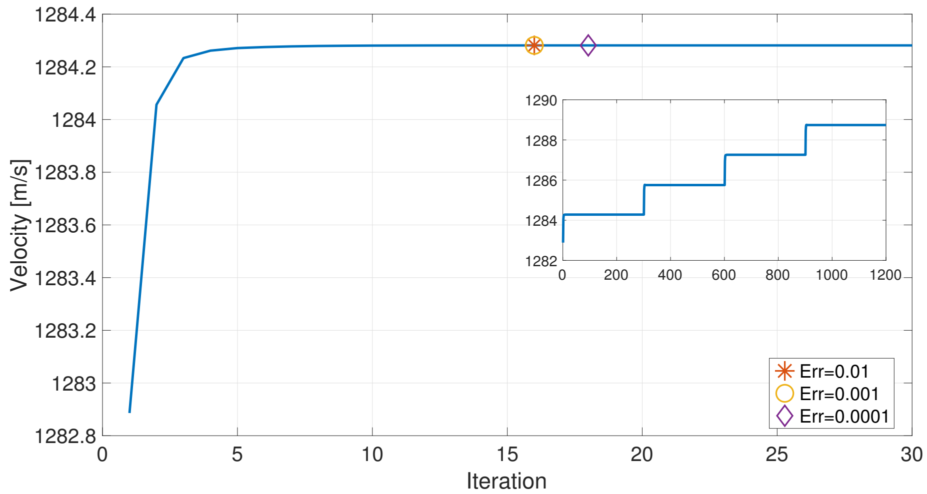

(a) Average velocity.

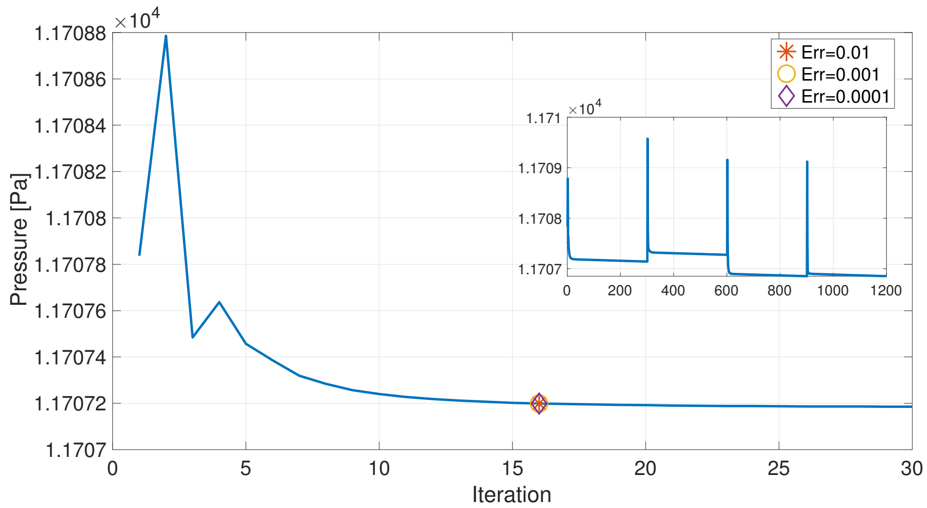

(b) Average pressure.

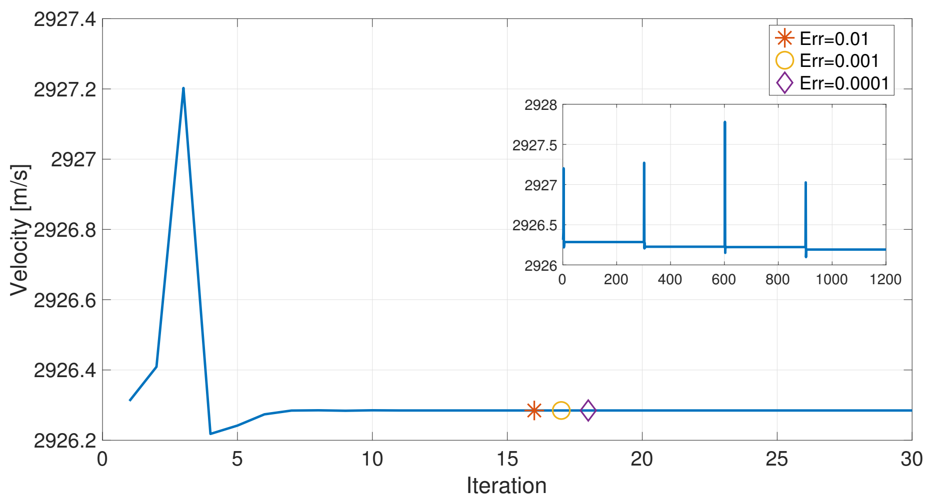

(c) Maximum velocity.

FIGURE 2.44: Average velocity (a), pressure (b) and maximum velocity (c) on the jet axis as the ii proceed at t=0.005 s.

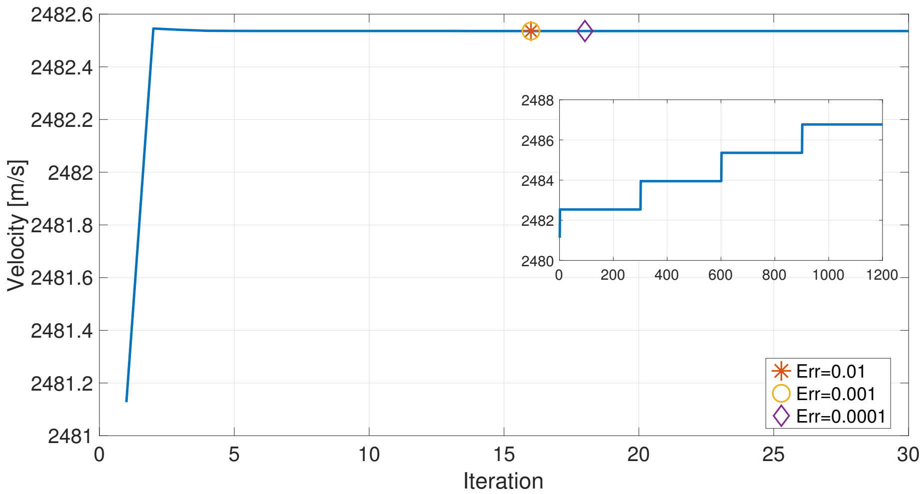

(a) Average velocity.

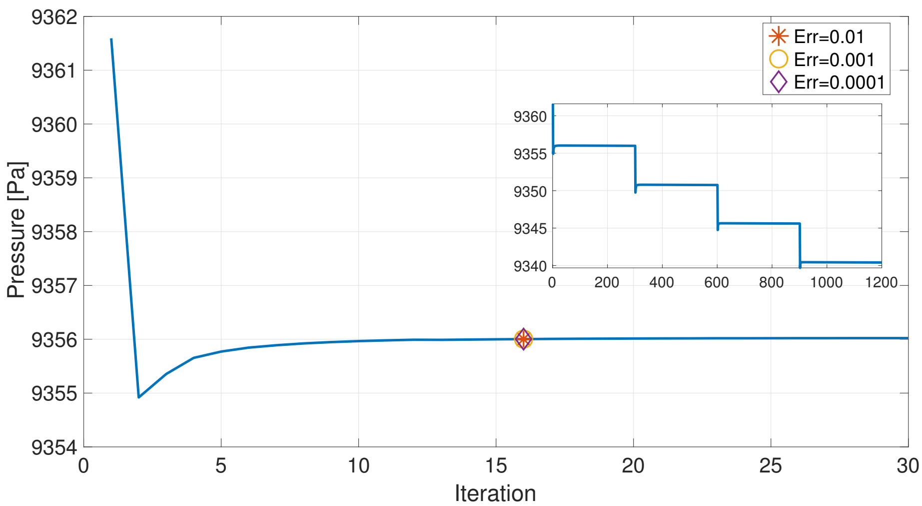

(b) Average pressure.

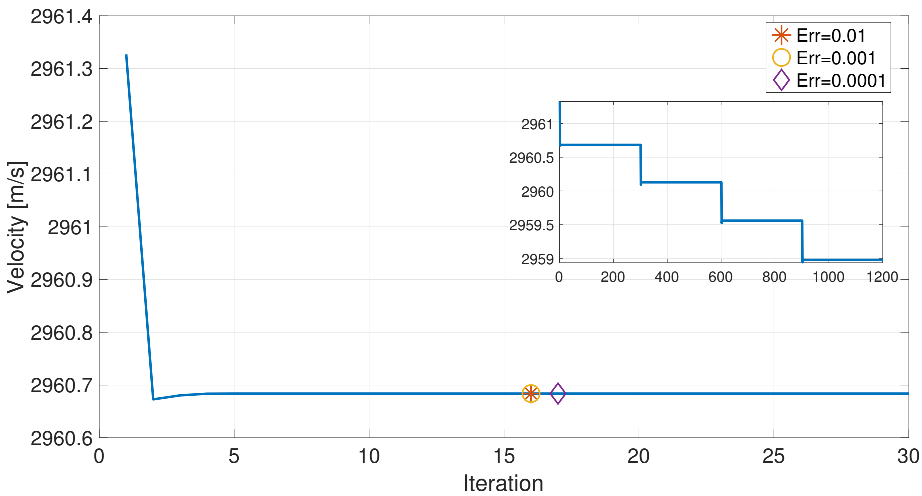

(c) Maximum velocity.

FIGURE 2.45: Average velocity (a), pressure (b) and maximum velocity (c) on the jet axis as the ii proceed at t=0.010 s.

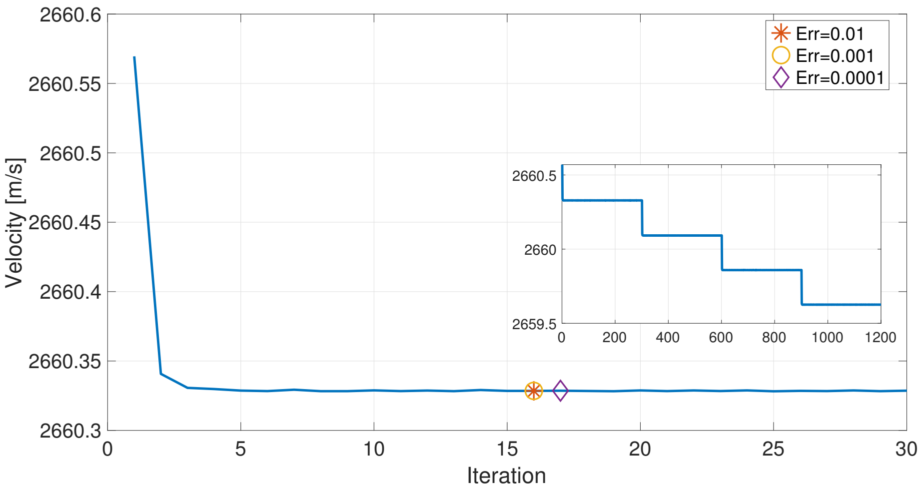

(a) Average velocity.

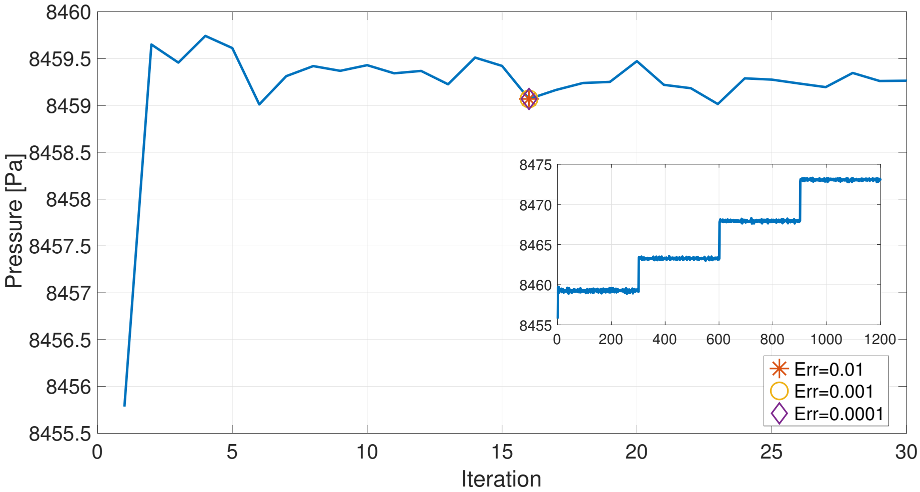

(b) Average pressure.

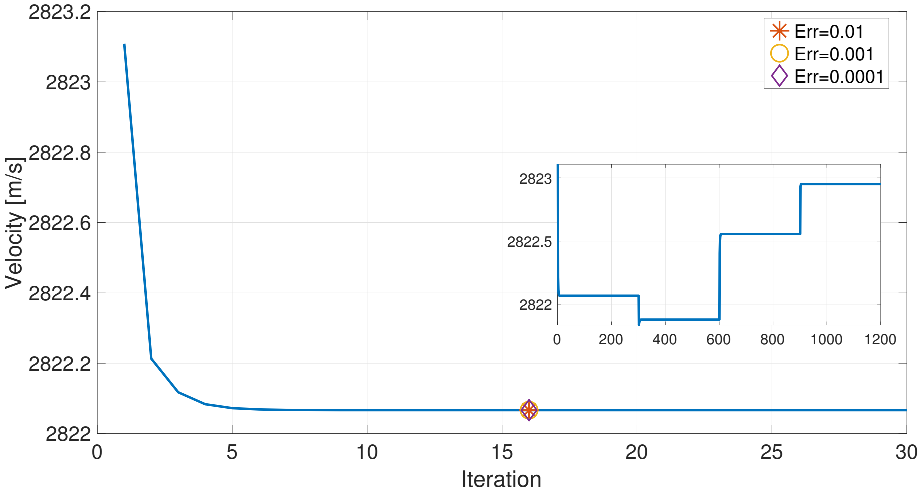

(c) Maximum velocity.

FIGURE 2.46: Average velocity (a), pressure (b) and maximum velocity (c) on the jet axis as the ii proceed at t=0.015 s.

The previous figures confirm that a minimum number of ii of 15/20 are necessary to be performed in order to be sure that the solution has converged. Furthermore, the implantation of the automatic stop to the ii gives good results. Since the difference of number of ii from 0.01 and 0.0001 is negligible (maximum 3 ii), the minimum error (0,001) can be introduced as threshold value.

2.4.7 Velocity threshold

Using the previously explained strategy for the setting of the optimal number of ii, time-step and grid base size, a convergence study on the velocity threshold to set in the AMR algorithm is performed. Table 2.14 summarises the seven cases studied:

TABLE 2.14: Cases for the choice of the V$_{thr}$ value.

	Velocity threshold
Case 1	0.60 V_{max}
Case 2	0.40 V_{max}
Case 3	0.30 V_{max}
Case 4	0.25 V_{max}
Case 5	0.20 V_{max}
Case 6	0.15 V_{max}
Case 7	0.10 V_{max}

The convergence study is performed checking three parameters:

- Mach disk location
- Pressure and velocity values in correspondence of the Mach disk location
- Spatial profile along the jet axis of pressure and velocity in two instants of the simulations (t_1=0.005 s and t_2=0.010 s).

Figure 2.47 shows that, at t_1 the jet has reached a distance of about 5 metres from the nozzle and the shock is located at a distance between 2 and 3 metres from the nozzle.

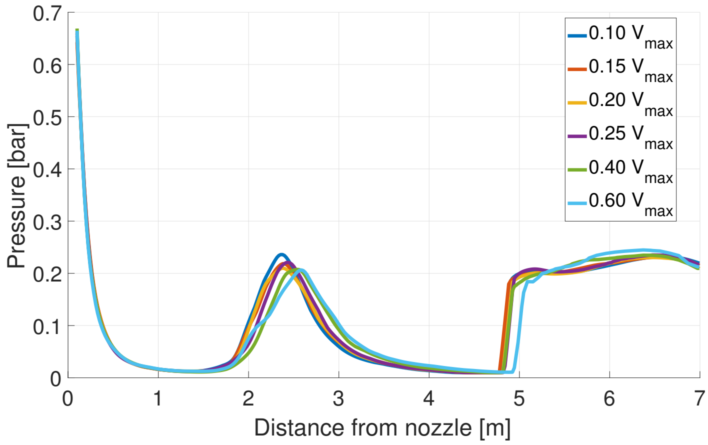

FIGURE 2.47: Pressure profile on axis at t=0.005 s with different V$_{thr}$.

In correspondence of the shock a pressure peak occurs; the lower the velocity threshold the higher the pressure peak value. The simulation with the highest velocity threshold (light blue line) does not foresee accurately the final edge of the jet since it is the only one detached from the others.

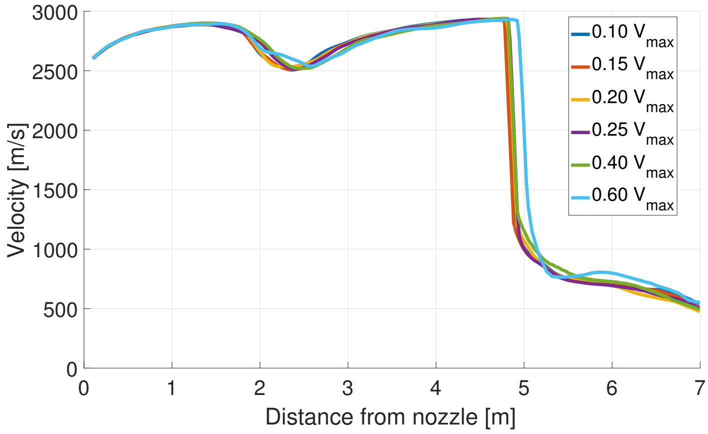

FIGURE 2.48: Velocity profile on axis at t=0.005 s with different V_{thr}.

As far as the spatial distribution of the velocity at t_1, showed in Figure 2.48, is of concern, a minimum value is expected in correspondence of the shock. Also in this case, the simulation with the highest threshold value is characterised by a not so accurate forecast of the jet spatial limits.

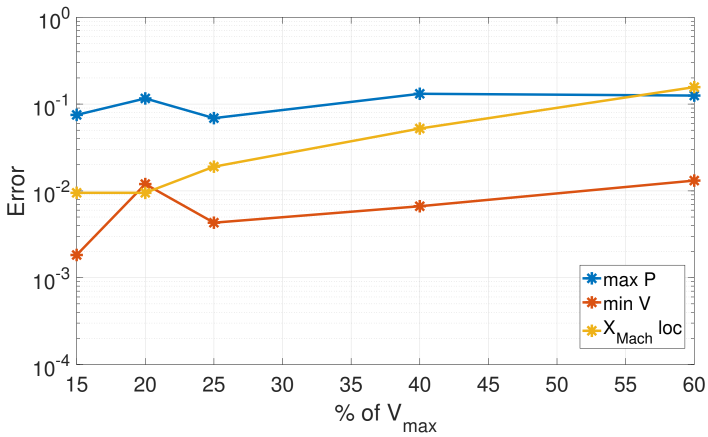

FIGURE 2.49: Error on maximum pressure, minimum velocity and Mach disk location at t=0.005 s with different V_{thr}.

Once the qualitative observations of the pressure and velocity distribution at t_1 are performed, a quantitative analysis on the error with respect to the case with the lowest velocity threshold is presented in Figure 2.49: the error on the maximum pressure is of the order of 10^{-1} independently from the threshold value, however, the minimum velocity and the Mach disk location are characterised by lower errors which decrease decreasing the V_{thr}. In particular, a minimum error of 0.01 is achieved for the Mach disk location, while, as concerns the minimum velocity, the lowest error is 0.002. Following the previous description, assuming that the maximum pressure has the same error independently from the V_{thr}, the key role is played by the other two monitors which have an error value lower than 0.02 with a velocity threshold of 25 %.

As concerns the second instants, t_2, the same analyses are performed looking at Figures 2.50 and 2.51 at this instant, the shock keeps maintaining its position between 2 and 3 meters while the front end of the jet has overtaken 7 meters.

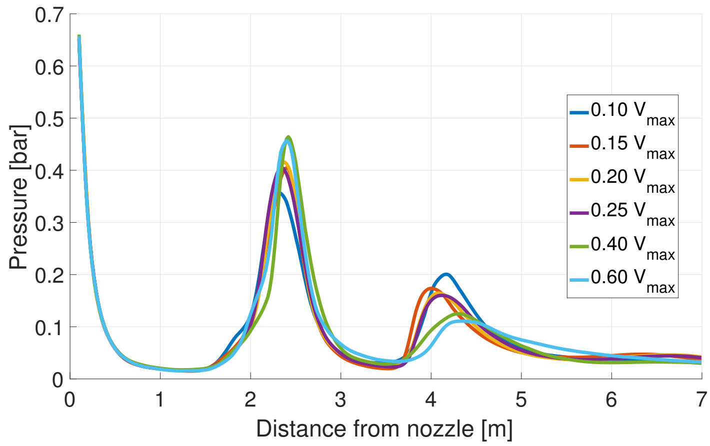

FIGURE 2.50: Pressure profile on axis at t=0.01 s with different V_{thr}.

As far as the pressure spatial distribution at t_2 is concerned, the maximum value of pressure is increased with respect to t_1, and an increase of V_{thr}, causes a decrease of the maximum value. Some distortions are present between 4 and 5 meters.

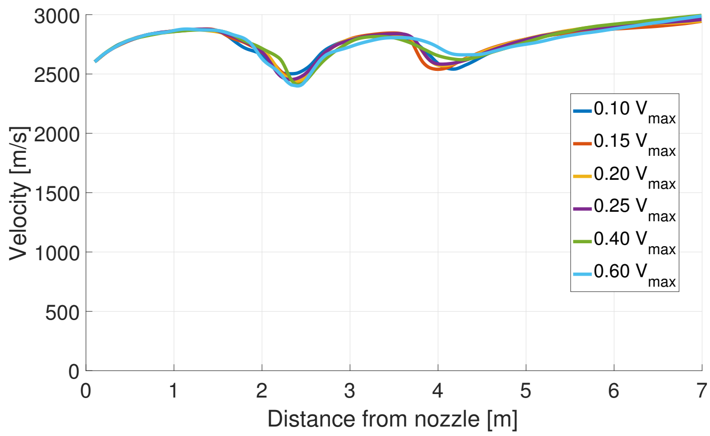

FIGURE 2.51: Velocity profile on axis at t=0.01 s with different V_{thr}.

The velocity evolution shows a minimum in correspondence of the shock and, as presented in the pressure distribution evolution, some irregularities are present between 4 and 5 meters.

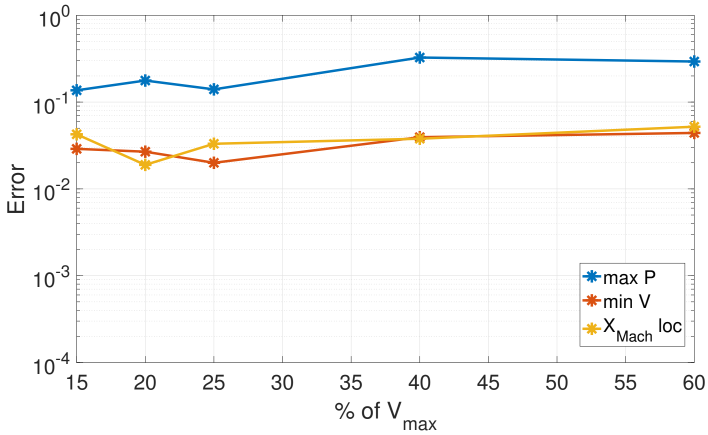

FIGURE 2.52: Error on maximum pressure, minimum velocity and Mach disk location at t=0.01 s with different V_{thr}.

Due to the higher presence of irregularities, the error in this second instants are characterised by higher values with respect to the previous instant (see Figure 2.52). The three errors do not decrease a lot decreasing the V_{thr}, as in the previous case. All the errors have a minimum value of the order of 10^{-2} and 10^{-1}.

As a conclusion, this parametric study states that a reasonable choice for V_{thr} can be 0.25 V_{max}, in line with the results of section 2.3.3.

2.5 Conclusions

All the previous sections represent a perfect recipe for the study of an under expanded jet which develops in an open domain and impinges on a cylindrical wall. Every section of this chapter justifies each choice that will be implemented in the 2D planar simulation. Table 2.15 shows a summary of the results from Chapter 2.

TABLE 2.15: Summary of the results from Chapter 2.

FREE JET STUDY - steady analysis	
Turbulence model	k-ω SST
WALL TREATMENT	
Number of prism layers	5
FREE JET STUDY - unsteady analysis	
Time-step	7.5 μs
Grid base size	from AMR algorithm
Number of ii	from asymptotic study (with min 20 ii)
V_{thr} for AMR algorithm	0.25 V_{max}

Chapter 3

CFD simulation of the in-VV LOCA for the EU DEMO reactor

In this chapter the in-VV LOCA in the EU DEMO reactor is simulated considering two different simplified geometries of the VV:

- 2D planar geometry: a simulation with the implementation of the AMR validated algorithm on a domain with the same characteristics outlined in section 2.4.2.
- 3D toroidal geometry: a preliminary study performed with the previously exposed conditions on a 3D domain characterised by a static mesh without the implementation of the AMR algorithm.

The comparisons between the results obtained in the 2D planar geometry, 3D toroidal geometry and those from the MODELICA 0D simulation will be exposed in the final section of this chapter. The transient starts at t=0 s and stops when the average pressure on the BD, after having reached (1.5 bar) decreases below it (t_{end}=0.025 s).

3.1 2D planar geometry

In this study, the AMR algorithm presented in section 2.3.3 is adopted and implemented with the settings derived from section 2.5 in the 2D planar geometry presented in section 2.4.2 A summary of the parameters introduced is showed in Table 3.1.

TABLE 3.1: Characteristics of the CFD study for the 2D planar geometry.

Time-step	7.5 μs
Type of mesh	Polyhedral
Dynamic mesh	Based on Co=1
Maximum number of cells	210k
Threshold velocity for AMR	0.25 V_{max}
Minimum error for the ii convergence	0.0001
Number of prism layers	5

Figures 3.1 and 3.2 show the evolution of the mesh and the Courant number on the domain in four instants of the transient: the coupling between the mesh and the moving jet and the respect of the CFL condition are demonstrated since the mesh always covers the portions of the domain interested by the presence of the jet and

the resulting Courant number is in the correct range. It can be noticed that, as the transient proceeds, the number of cells increases starting from 2000 and reaching a maximum of 185000 cells (see Figure 3.3).

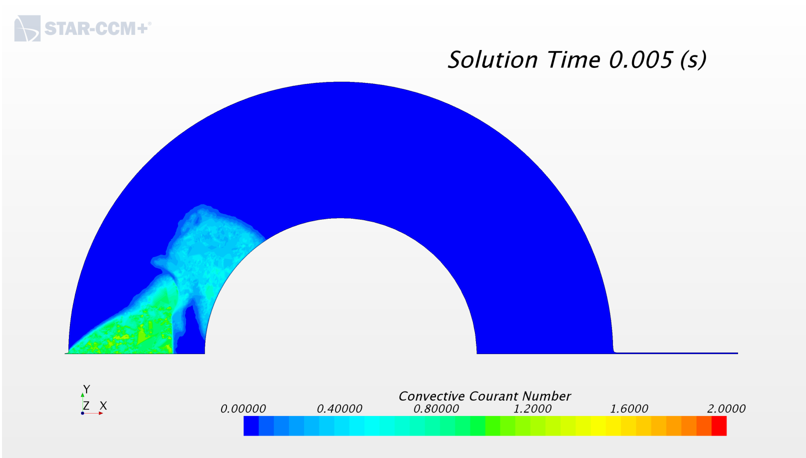

(a) Courant value.

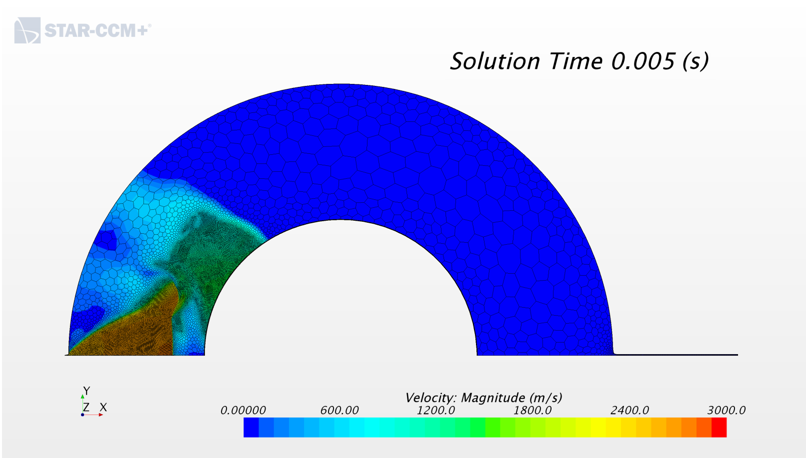

(b) Mesh distribution.

FIGURE 3.1: Courant and Mesh distribution at t=0.005 s.

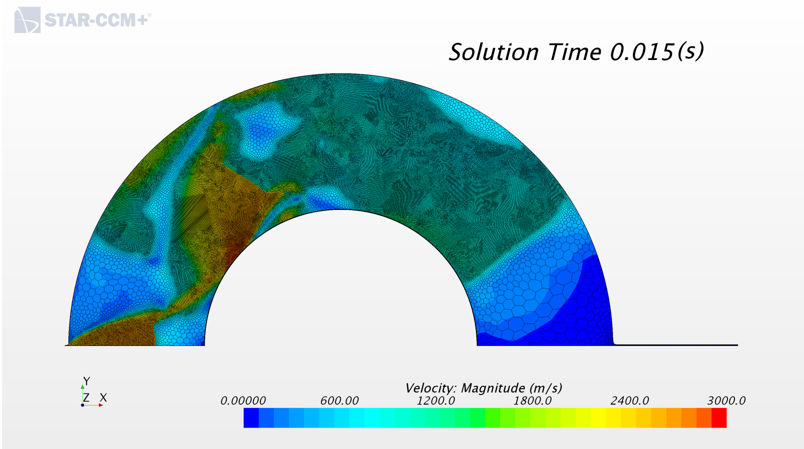

(a) Courant value.

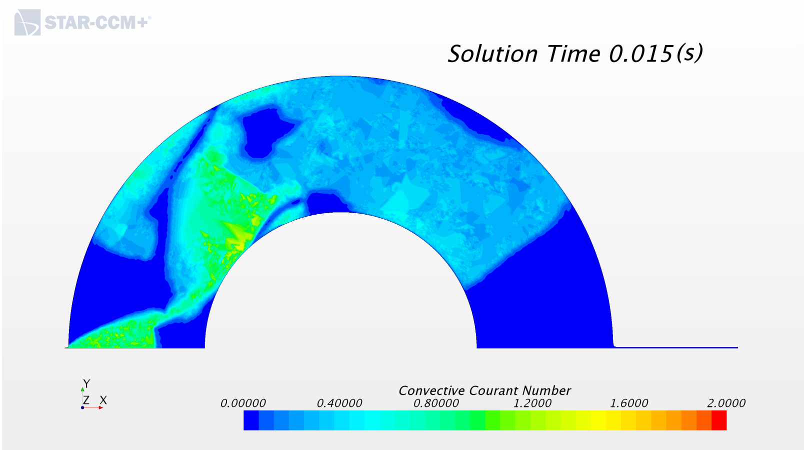

(b) Mesh distribution.

FIGURE 3.2: Courant and Mesh distribution at t=0.015 s.

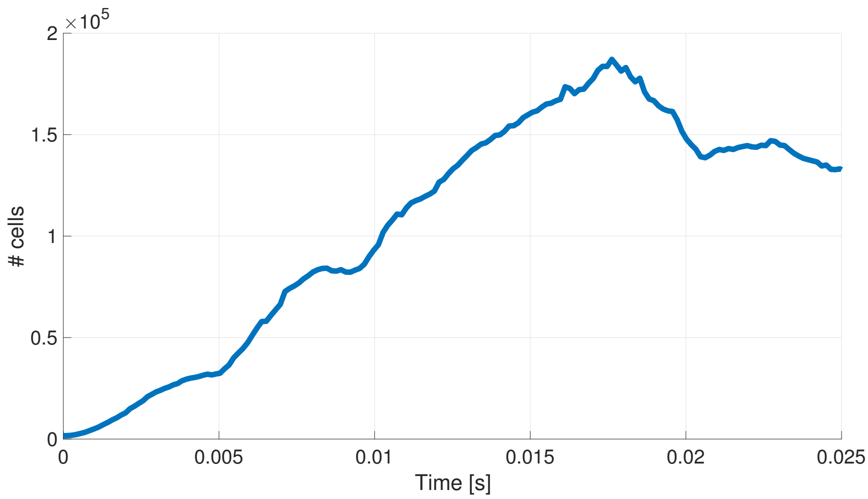

FIGURE 3.3: Number of cells as the transient proceeds.

3.2 From the 2D to the preliminary 3D

The sketch of the toroidal geometry on which the 3D simulations are performed is showed in Figure 3.5(a): the solid is built with a revolution of the section showed in Figure 3.4 around the y-axis. Figure 3.4 and Table 3.2 summarise the main geometrical dimensions, which are computed considering the following parameters equal to those present in the real 3D geometry:

- the distance between internal and external walls (6 meters);
- the radius of the external wall (12 meters);
- the total volume of the vessel (3000 m^3);
- the BD section area (1 m^2, showed in Figure 3.5(b));
- the break section area (0.322 m^2, showed in Figure 3.5(c));

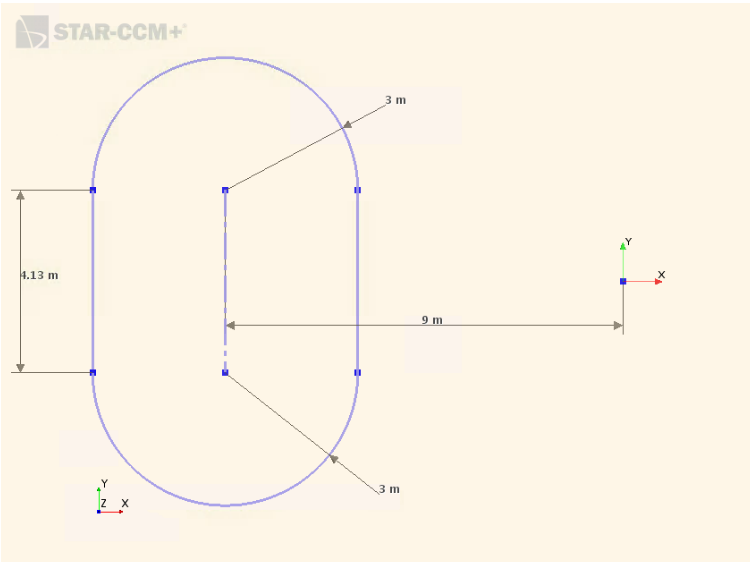

FIGURE 3.4: Section of the 3D toroidal geometry.

TABLE 3.2: Main geometrical details of the 3D toroidal geometry.

Volume of the VV	3000 m^3
Break area	0.322 m^2
Break radius	0.32 m
BD area	1 m^2
BD radius	0.56 m
BD channel length	6 m

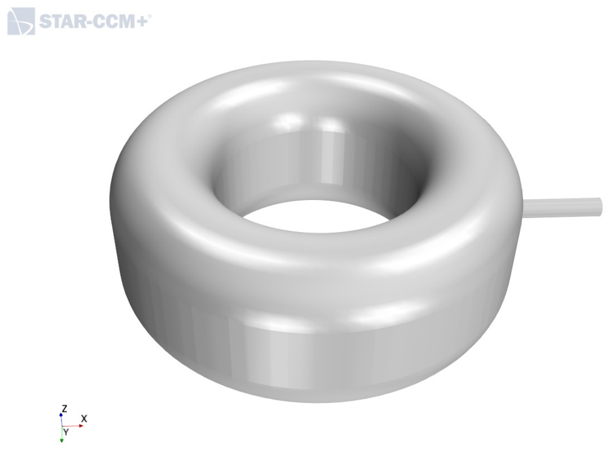

(a) 3D geometry.

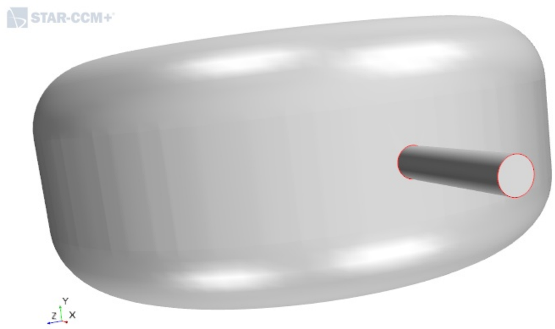

(b) Zoom on the BD.

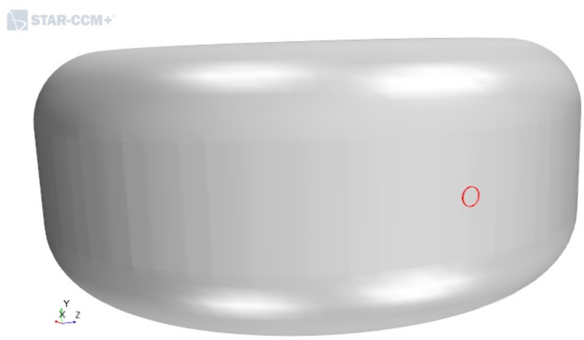

(c) Zoom on inlet.

FIGURE 3.5: Sketch of the 3D toroidal geometry.

Due to the geometry characterised by symmetric conditions, only the quarter of the domain showed in Figure 3.6 is simulated.

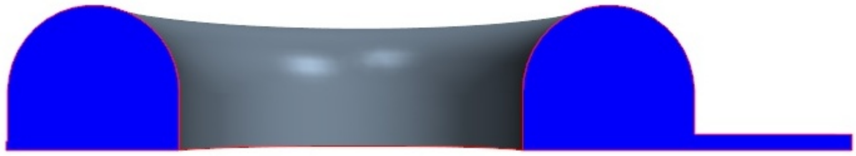

(a) Frontal view.

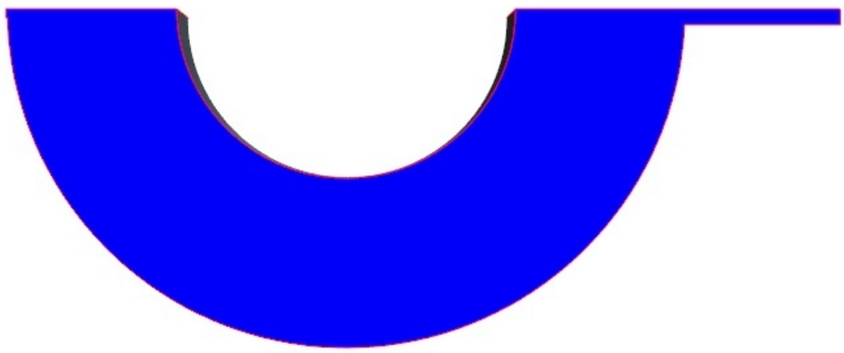

(b) View from the bottom.

FIGURE 3.6: 3D toroidal CFD domain. Blue surfaces are symmetry plane boundary conditions.

3.2.1 Mesh and CFD set-up

This preliminary CFD study is performed on a polyhedral static mesh characterised by the parameters outlined in Table 3.3. A coupled implicit scheme with a time step of 5 μs and a k-ω SST turbulence model is used.

TABLE 3.3: Main features of the mesh for the 3D toroidal study.

Maximum base size	25 cm
Minimum base size	2.5 cm
Base size on inlet	2 cm
Number of prism layers	5
Number of cells	150k

Figure 3.7 show the mesh on the 3D toroidal domain: the mesh is still coarse.

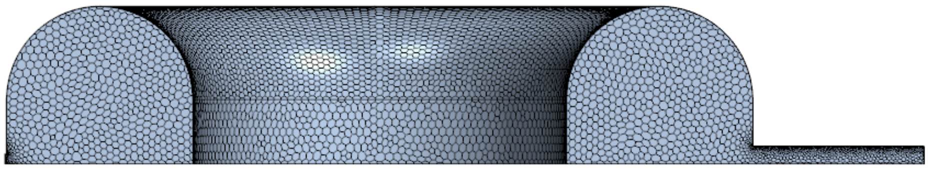

(a) Frontal view.

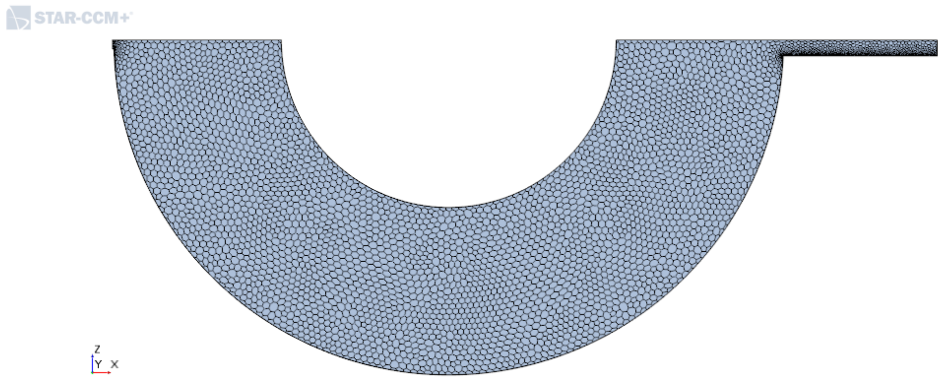

(b) View from the bottom.

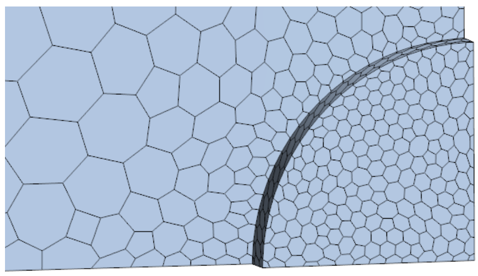

(c) Remeshed inlet.

FIGURE 3.7: 3D toroidal meshed domain.

3.3 Boundary and initial conditions

In both 2D and 3D geometries the same set-up for the boundary and the initial conditions is implemented. In order to avoid the introduction of the volume of the PHTS in the CFD domain, the mass flow rate, PHTS pressure and temperature from the 0D study are imposed as boundary conditions at the inlet of the two domains. A summary of the boundary and initial condition set-up is showed in Table 3.4.

TABLE 3.4: Initial conditions imposed in the final simulations.

Inlet velocity	1321 m/s (Mach=1)
Mass flow rate	1582 kg/s
PHTS total pressure	80 bar
PHTS static pressure	39 bar
PHTS total temperature	673 K
PHTS static temperature	506 K
PHTS gas composition	Helium (ideal gas)
PHTS total density	5.71 kg/m^3
PHTS static density	3.72 kg/m^3
VV pressure	0.1 bar
VV temperature	293 K

The temporal evolution of the values detected on the inlet surface are showed in Figures 3.8 - 3.11: the perfect agreement between the expected values from MODELICA and literature (see Appendix B) and the simulated data confirm the consistency and correctness of the boundary conditions set-up.

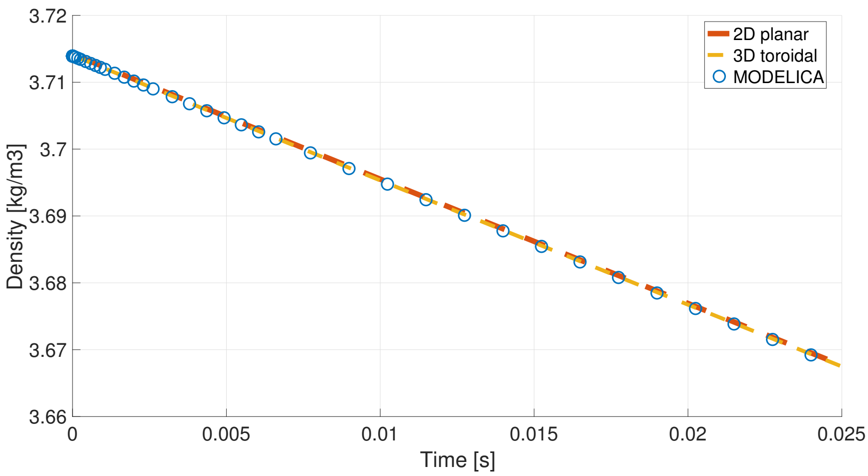

FIGURE 3.8: Inlet density.

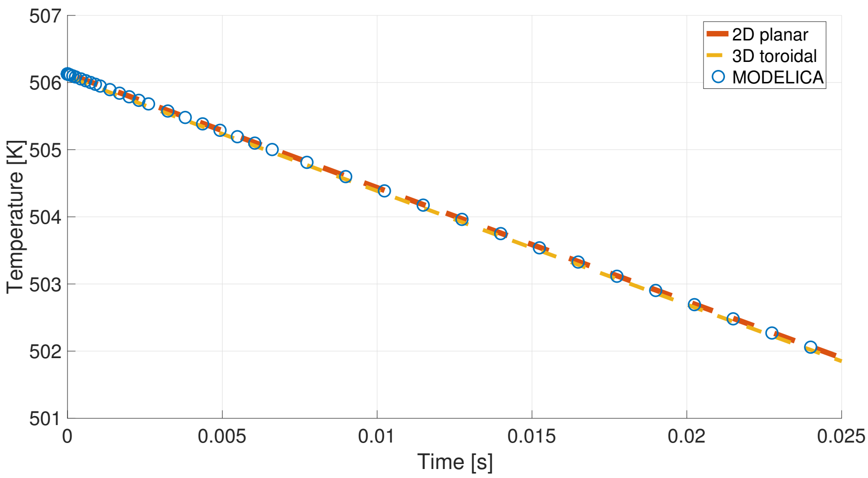

FIGURE 3.9: Inlet temperature.

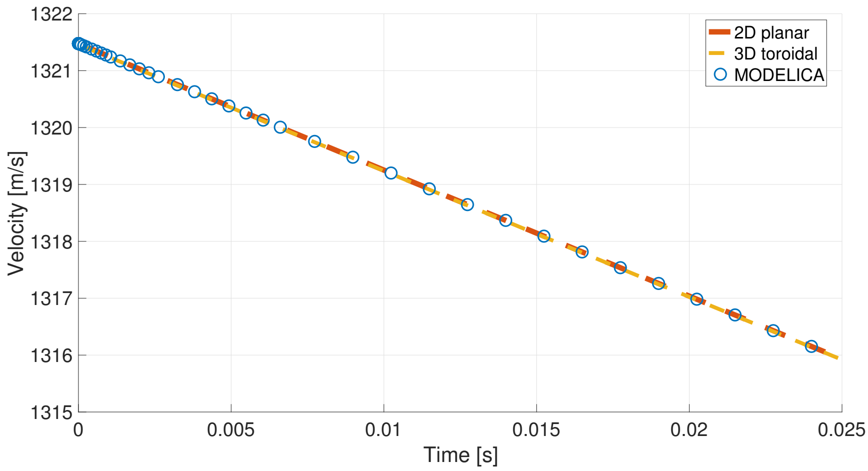

FIGURE 3.10: Inlet velocity.

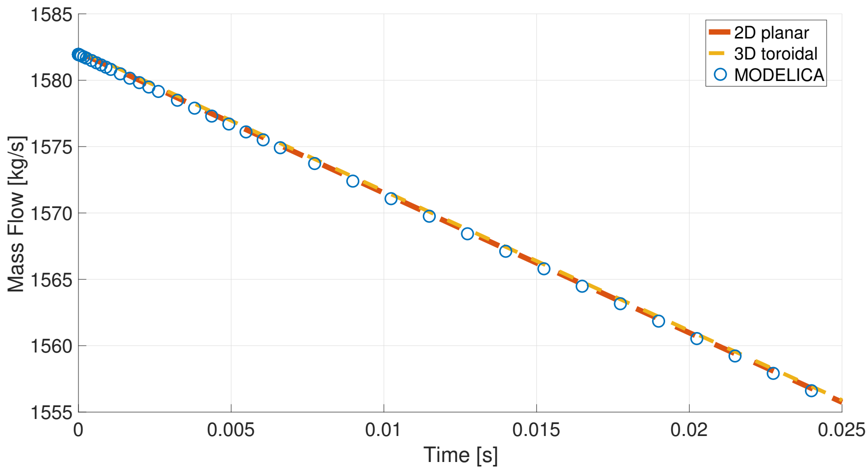

FIGURE 3.11: Inlet massflow.

3.4 Results

This chapter collects the results from the CFD simulations performed. The fluid-dynamic inside the VV is investigated by the analysis of pressure and velocity fields captured in different instants of the transient while quantitative results regarding pressure, density and temperature from CFD are compared with those expected from MODELICA.

3.4.1 2D planar geometry: pressure and velocity fields

For a better understanding of the dynamic of the helium jet that develops inside the VV, Figures 3.12 - 3.26 show the entire transient in terms of pressure and velocity fields in different instants. The jet moves from the inlet, impinges on the internal wall directly facing the break; afterwards, it is deviated towards the external wall where, half of it moves towards the BD while the other part comes back to the inlet area on the external wall giving rise to the establishment of a vortex. Once the moving front reaches the BD, it causes on its surface a pressure peak that triggers the operations of the VVPSS.

Figures 3.12 and 3.13 show the pressure and velocity field at t=0.003 s: at this instant, the jet has already travelled a distance of 6 metres: its velocity is very high (~2700 m/s) and a first high pressure spot (~1 bar) on the surface of the internal wall due to the first jet impingement is detected.

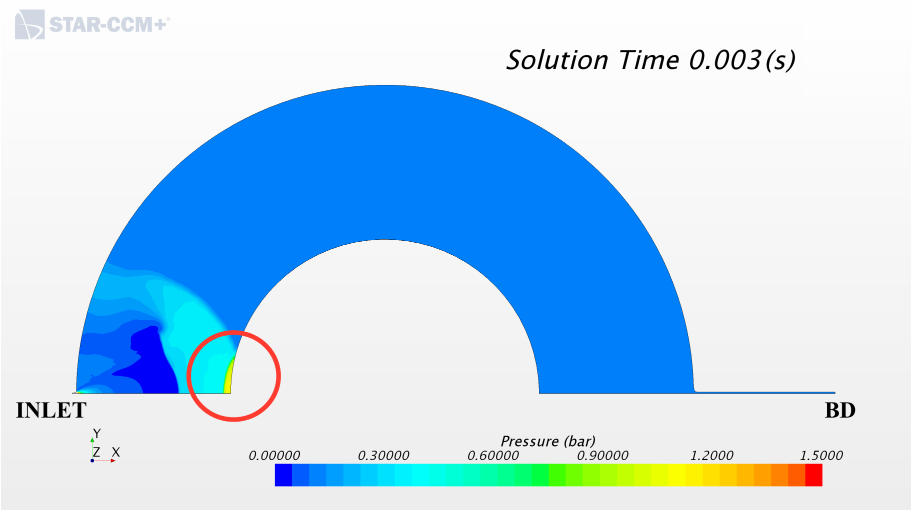

FIGURE 3.12: Pressure field on the 2D planar geometry at t=0.003 s.

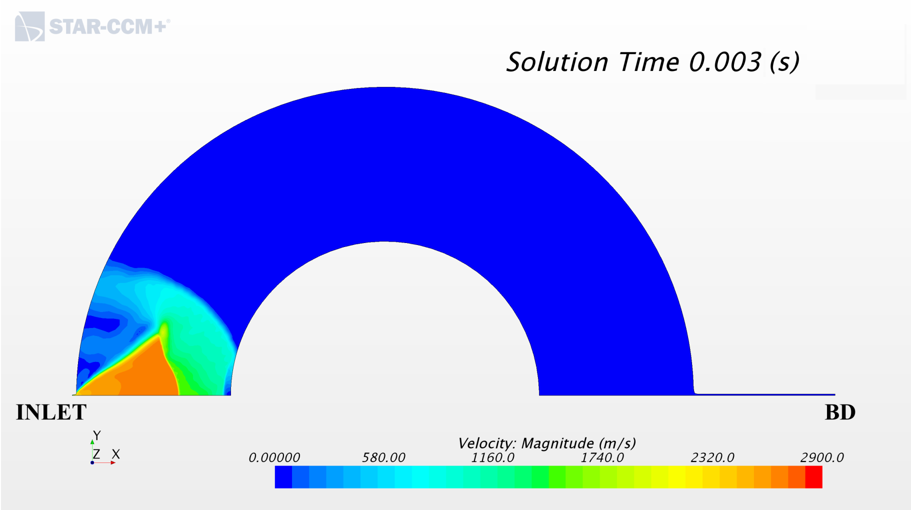

FIGURE 3.13: Velocity field on the 2D planar geometry at t=0.003 s.

At t=0.005 s, the pressure and velocity fields showed in Figures 3.14 and 3.15 state that the high pressure spot on the internal wall increases its dimension and the jet is deviated towards the external wall at a lower velocity with respect to the previous instant.

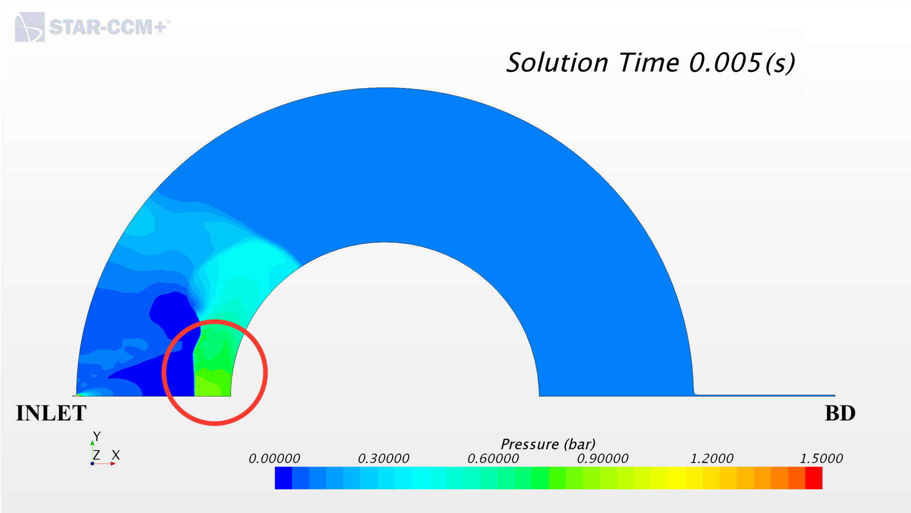

FIGURE 3.14: Pressure field on the 2D planar geometry at t=0.005 s.

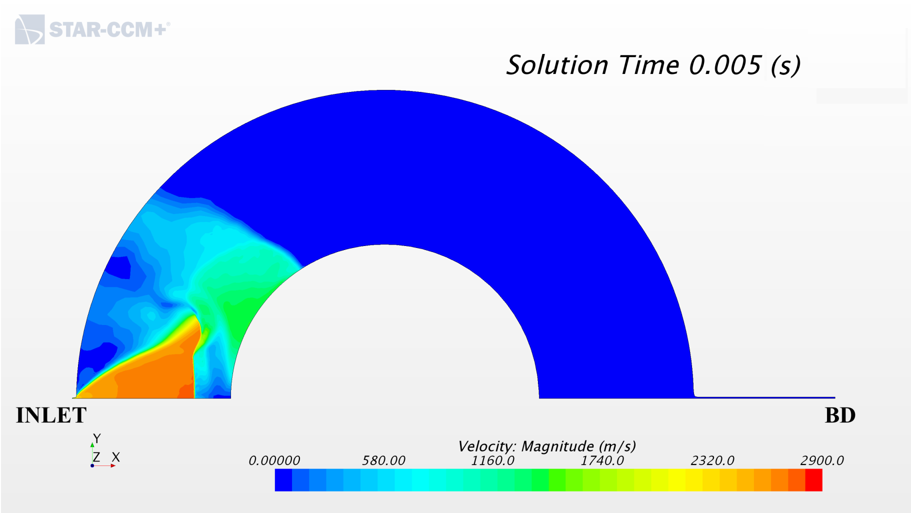

FIGURE 3.15: Velocity field on the 2D planar geometry at t=0.005 s

At t=0.007 s, Figures 3.16 and 3.17 show that the jet reaches the external wall yielding to a first increase of pressure on its surface.

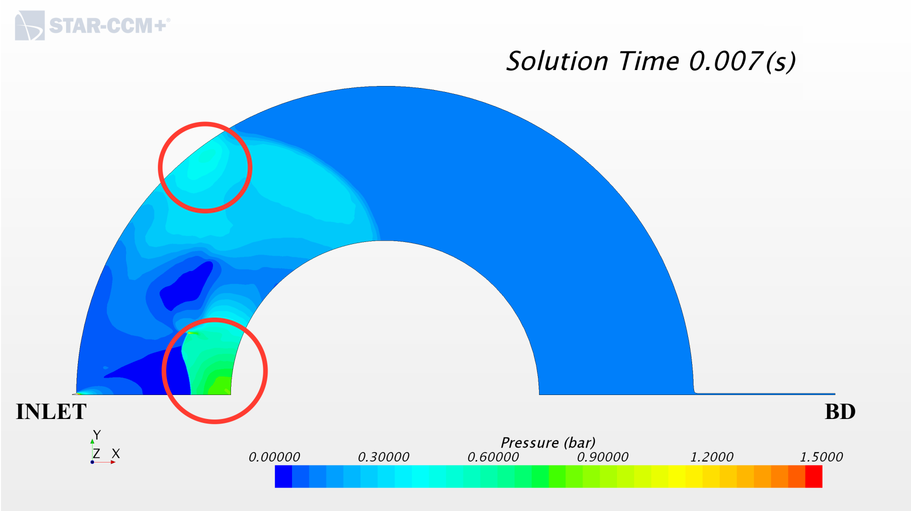

FIGURE 3.16: Pressure field on the 2D planar geometry at t=0.007 s.

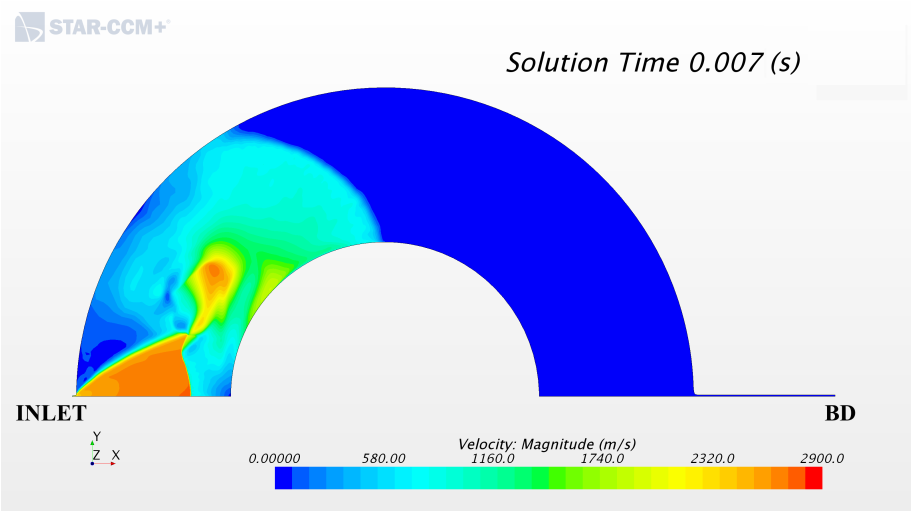

FIGURE 3.17: Velocity field on the 2D planar geometry at t=0.007 s.

At t=0.009 s, as in the case of the impingement on the internal wall, the high pressure spot on the external surface of the VV increases its dimension. The jet has travelled half the distance towards the BD. See Figures 3.18 and 3.19

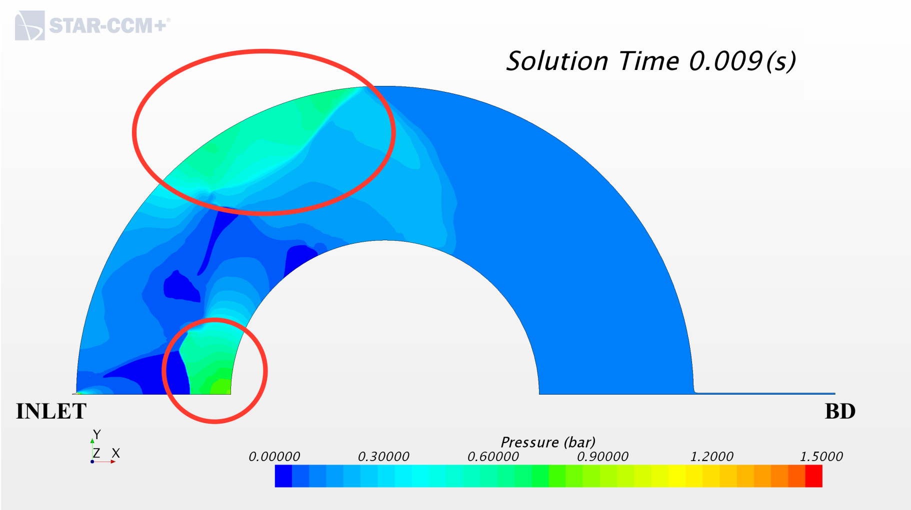

FIGURE 3.18: Pressure field on the 2D planar geometry at t=0.009 s.

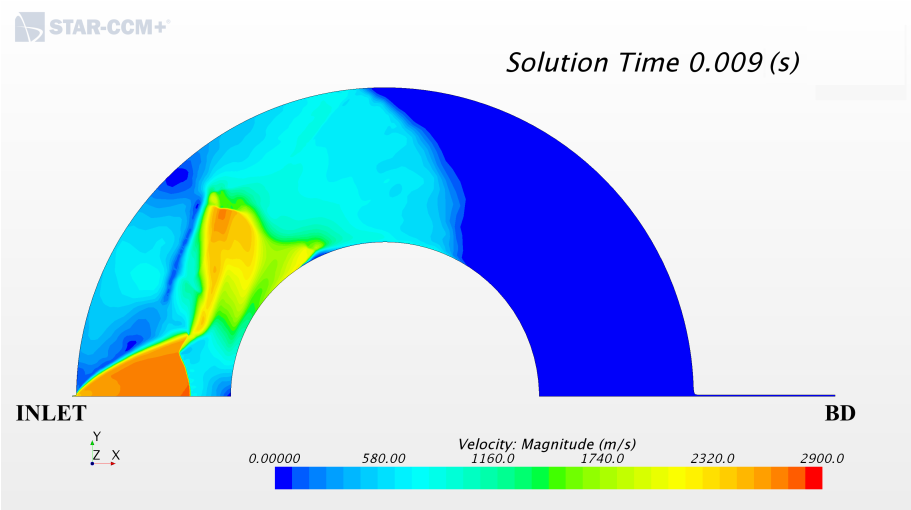

FIGURE 3.19: Velocity field on the 2D planar geometry at t=0.009 s.

The instant t=0.013 s is showed in Figures 3.20 and 3.21: the jet is filling the entire domain and it can be noticed the general behaviour that will establish regarding the velocity field. In fact, once the jet impinges on the external surface, a part of it keeps moving towards the BD, while the other part moves back to the inlet area generating a vortex. ...

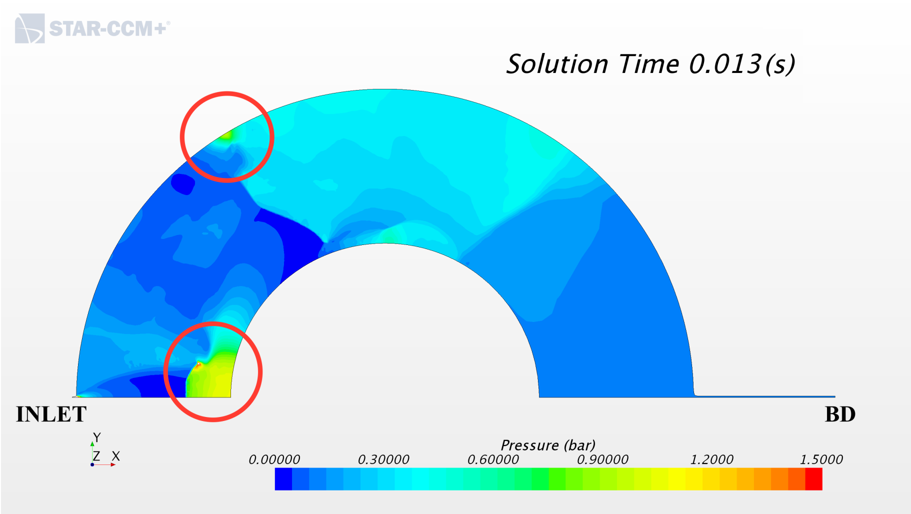

FIGURE 3.20: Pressure field on the 2D planar geometry at t=0.013 s.

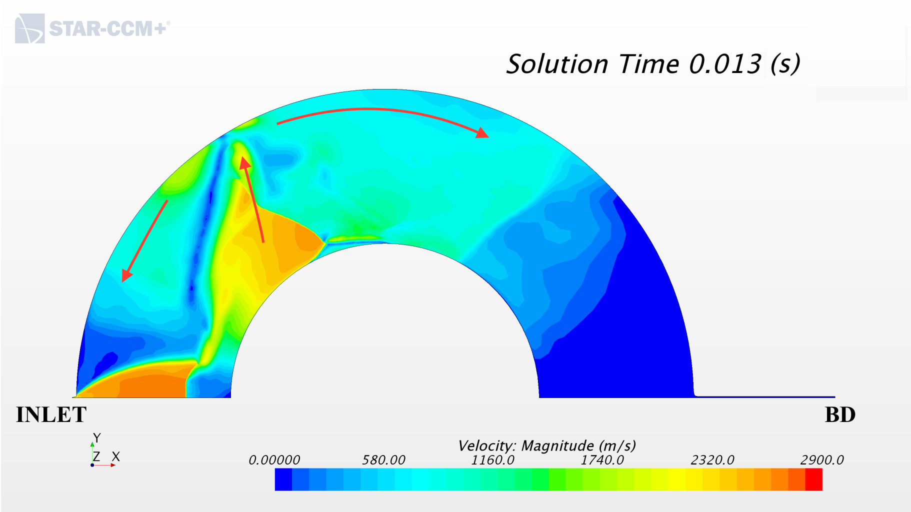

FIGURE 3.21: Velocity field on the 2D planar geometry at t=0.013 s.

Figures 3.22 and 3.23 show the instant t=0.019 s: the jet enters the BD channel and a high pressure spot is formed at the entrance. Three high pressure spots are present on the walls of the domain: one at the entrance of the BD channel, one on the internal wall facing the inlet and the last one on the external wall. It can be noticed that the initial shape of the jet has changed with respect to the initial one becoming more elongated and it gets closer to the internal wall surface causing an increase of the pressure values in that area. This phenomenon can be justified by the presence of the vortex in the inlet area that forces the jet elongation and strength (see Figure 3.24 for the detection of the near inlet vortex).

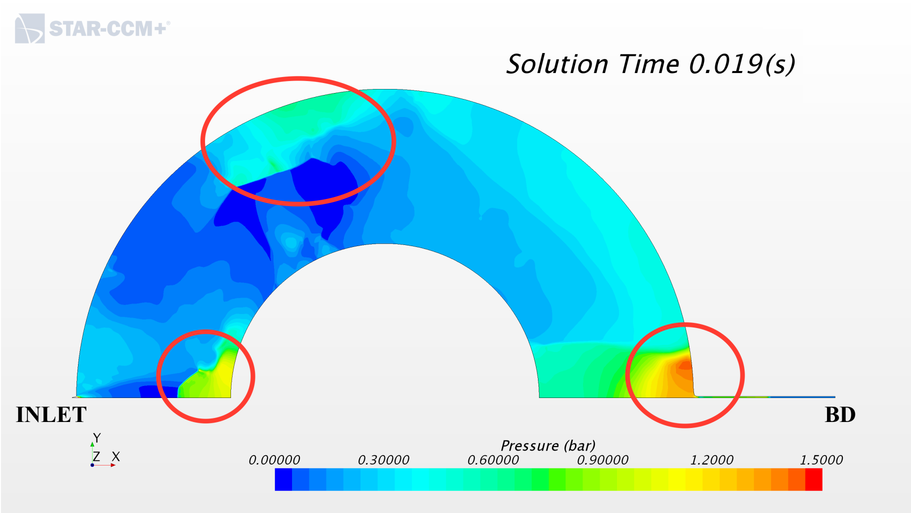

FIGURE 3.22: Pressure field on the 2D planar geometry at t=0.019 s.

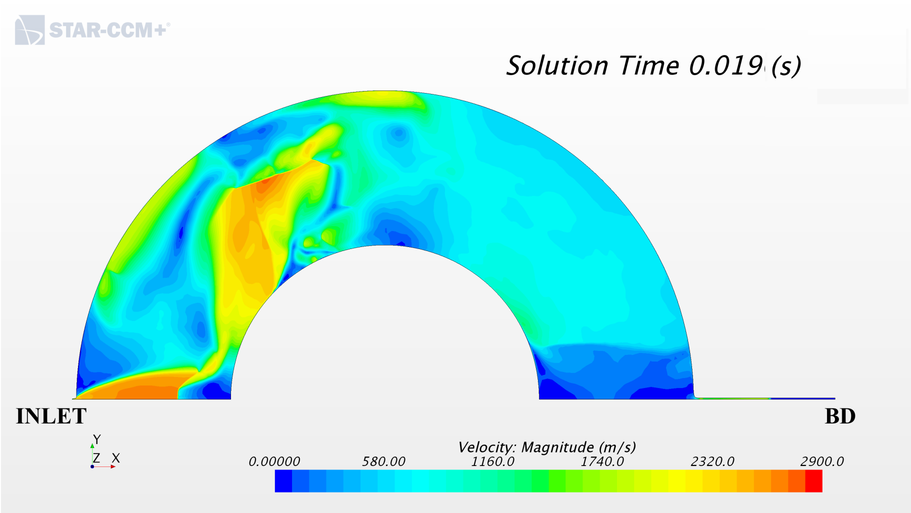

FIGURE 3.23: Velocity field on the 2D planar geometry at t=0.019 s.

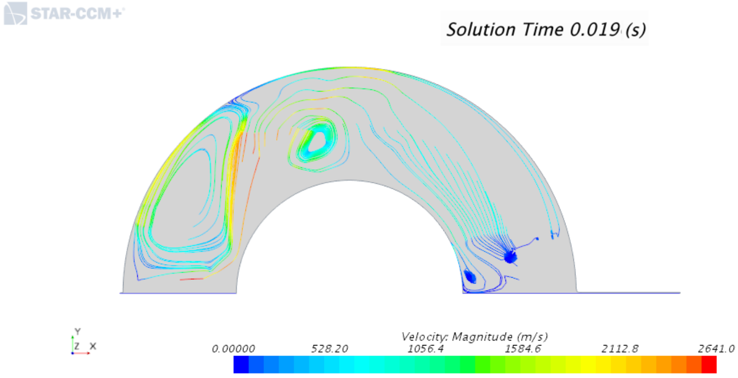

FIGURE 3.24: Velocity streamlines on the 2D planar geometry at t=0.019 s.

At t=0.021 s (see Figures 3.25 and 3.26), the pressure spot near the BD increases its dimension and the pressure on the BD surface reaches values over the rupture limit. After this instant, the transient can be considered completed.

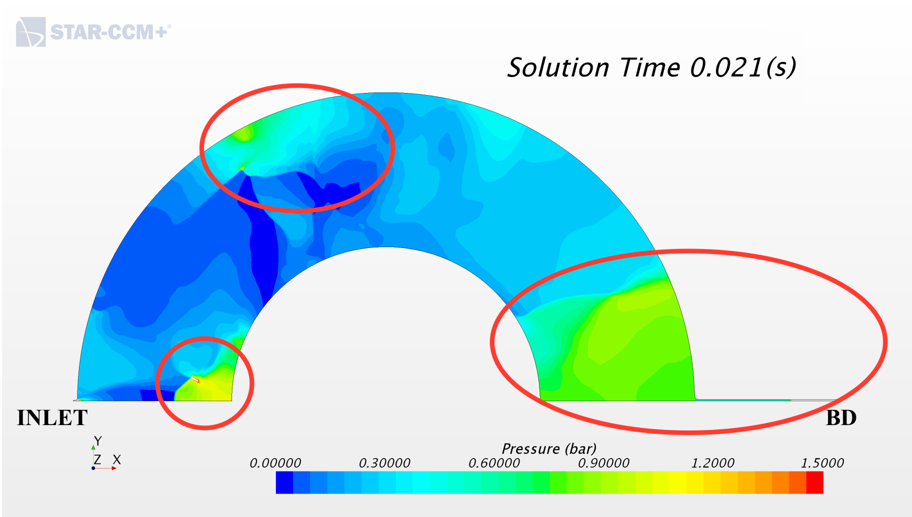

FIGURE 3.25: Pressure field on the 2D planar geometry at t=0.021 s.

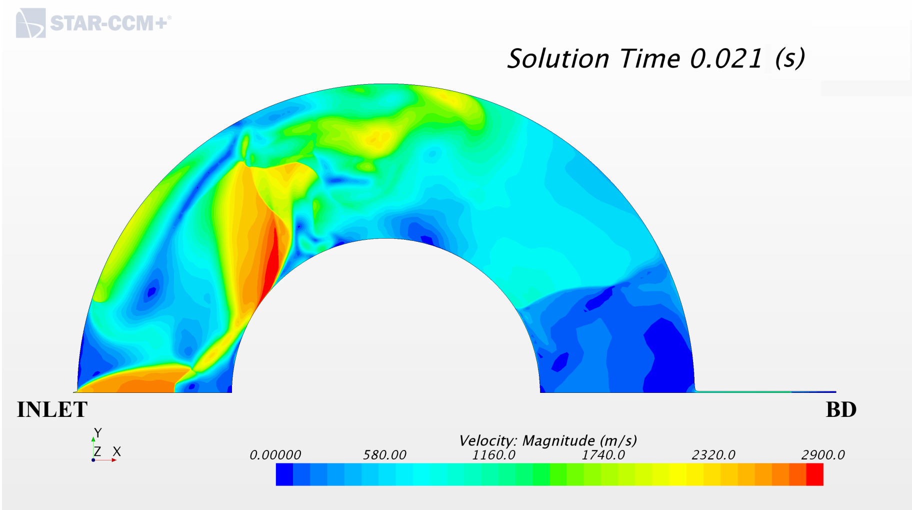

FIGURE 3.26: Velocity field on the 2D planar geometry at t=0.021 s.

3.4.2 Comparison with MODELICA

The comparison with the 0D MODELICA results is divided in two main parts: the first one dedicated to the comparison between the 0D results and the average values on the entire domain; the second one focused on the analysis of pressure values on the walls of the domain to investigate the presence of peaks overtaking the safety limit.

As far as the density and mass temporal evolutions are of concern, a quite perfect benchmark of the MODELICA with both CFD results is obtained as stated by Figures 3.27 and 3.28. The linear behaviour is confirmed even though the results from the 2D planar simulations are affected by small local oscillations that cause a maximum error of 2% with respect to MODELICA. These results verify the mass conservation (since MODELICA results are computed imposing this constraint) and the linear relation between mass and density since the two curves have the same slope.

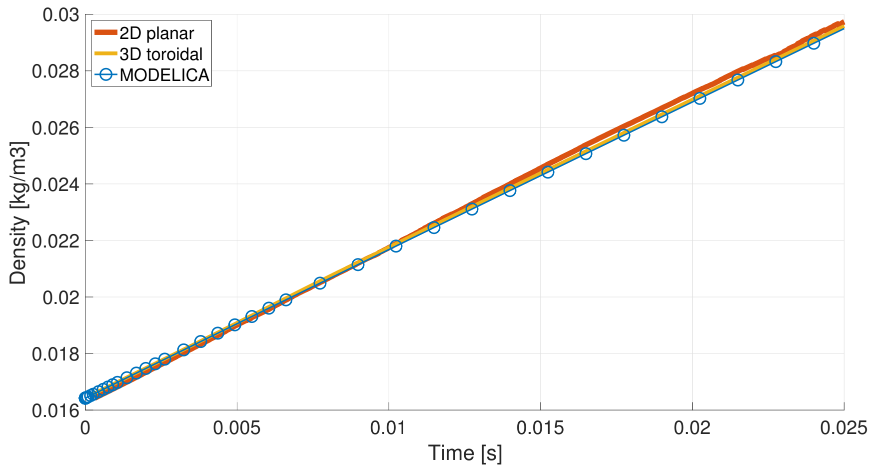

FIGURE 3.27: Average density in the entire domain.

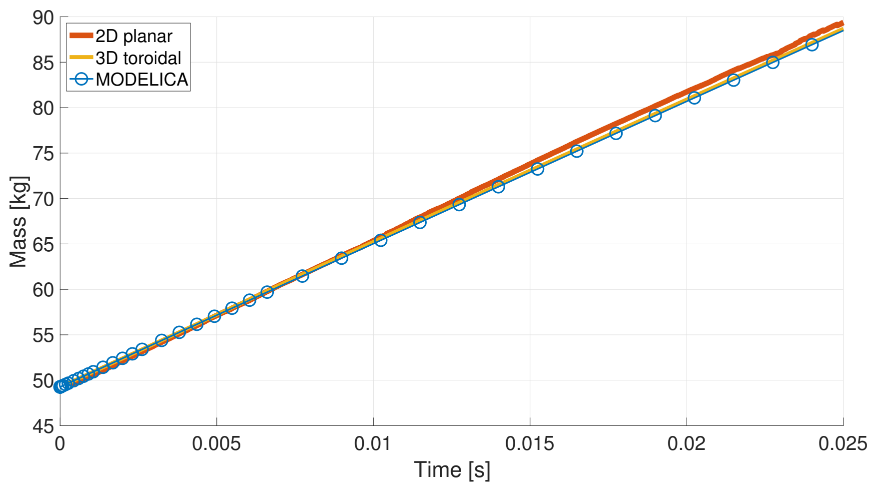

FIGURE 3.28: Total mass inside the domain.

The comparison of the average pressure in the VV, as showed in Figure 3.29, claims that the CFD foresees for both the cases studied a lower value (-12% max) with respect to MODELICA. However, the two CFD results evolve in the same way.

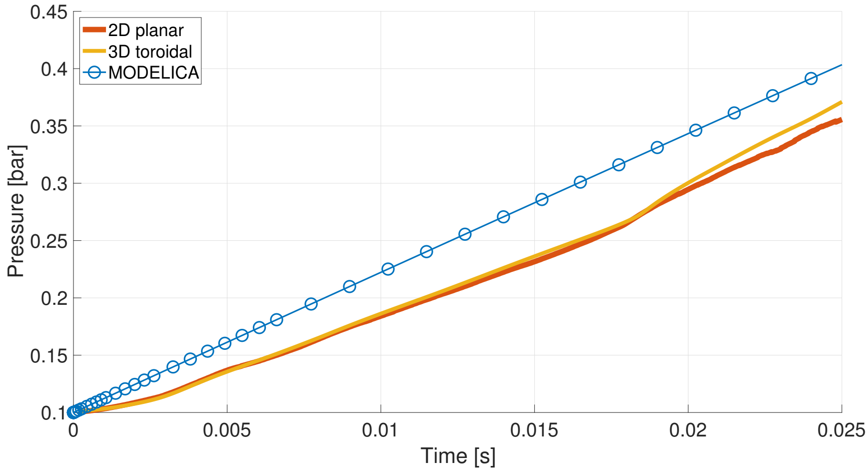

FIGURE 3.29: Average pressure in the entire domain.

Since pressure, temperature and density are related by the perfect gas law, and being the density well represented both in the 2D and 3D geometry, a lower (or equal) average pressure with respect to MODELICA will definitely cause a lower (or equal) average temperature. This statement is confirmed by Figure 3.30 that shows the same results as for the pressure: a lower value of the temperature with respect to MODELICA.

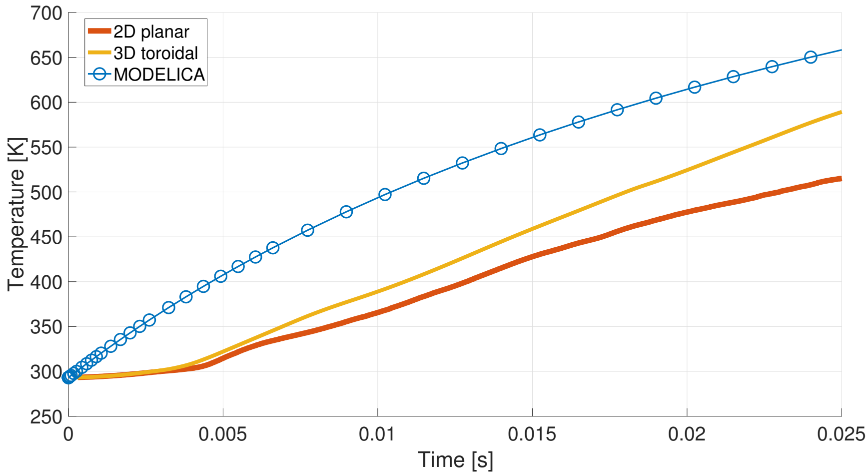

FIGURE 3.30: Average temperature in the entire domain.

The analysis of the average pressure on the BD surface, showed in Figure 3.31, aims at controlling the instant at which the rupture is expected to occur: at t~0.02 s the two CFD simulations detect a pressure peak (2.8 bar for the 3D simulation, 3 bar for the 2D) which overtake the BD opening limit (2 bar) that should cause the activation of the VVPSS and the discharge of helium towards the expansion volumes. After the peak, caused by the impingement of the jet on the BD surface, the measured pressure rapidly decreases due to the establishment of a pressure gradient between the BD surface and the VV that causes the helium to move back to the VV chamber.

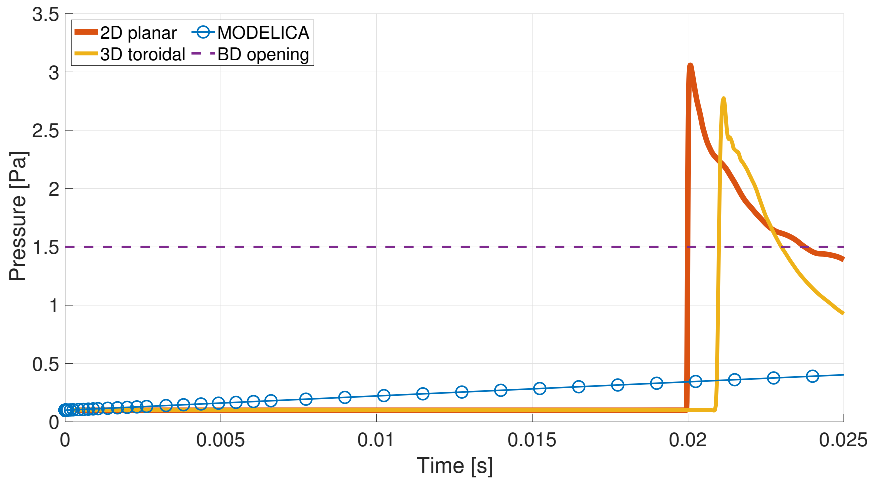

FIGURE 3.31: Pressure on the Burst Disk surface.

The change of direction of the flow in the BD channel of the 2D planar geometry is showed in Figure 3.32: before the impaction the flow is moving towards the BD surface (in the positive direction of x-axis), afterwards it moves back to the VV chamber with a lower velocity but negative i-th component of velocity.

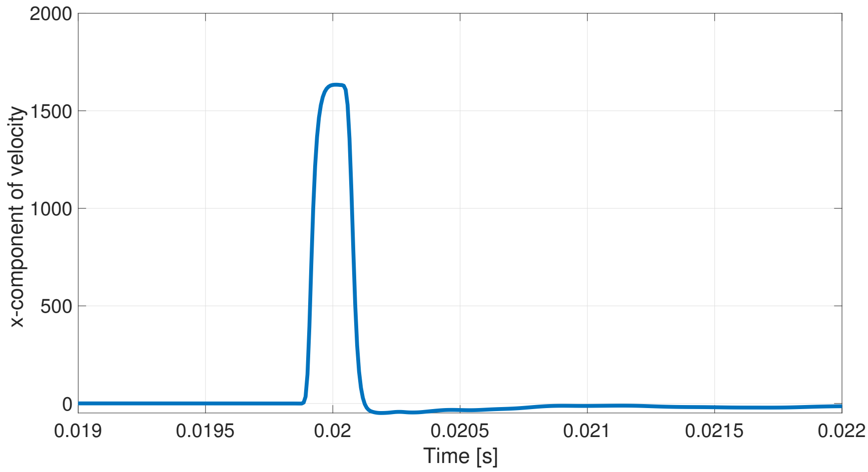

FIGURE 3.32: Average value of the i-th component of the velocity in a section located 15 cm from the BD surface. If positive, moving towards the BD and viceversa

A further analysis of the pressure on walls aimed at conducting a preliminary safety assessment of the structures mainly involved by the jet impingement is performed. The portions of the domain studied are the internal wall facing the break, the external wall on which the jet impinges after the first collision with the internal wall (analysis conducted only on the 2D domain) and, for the 3D domain, the upper surface of the VV. Figure 3.33 shows the pressure detected on the internal wall: as far as the average pressure is of concern, both CFD results are in line with the avearge pressure foreseen by MODELICA. The analysis of the maximum pressure confirms the detection for both geometries of the first peak, caused by the impingement of the jet on the wall, at t~0.0025 s: the timing of the peak is the same in both geometries and the peak values are similar being 1.6 bar for the 3D domain and 1.4 bar for the 2D domain. This first peak is below the safety limit in both geometries. As the transient proceeds, another peak is present for the 2D domain with a maximum value of 1.7 bar mainly due to the strengthening of the jet at the inlet area caused by the establishment of a vortex as already stated in the previous section of this chapter.

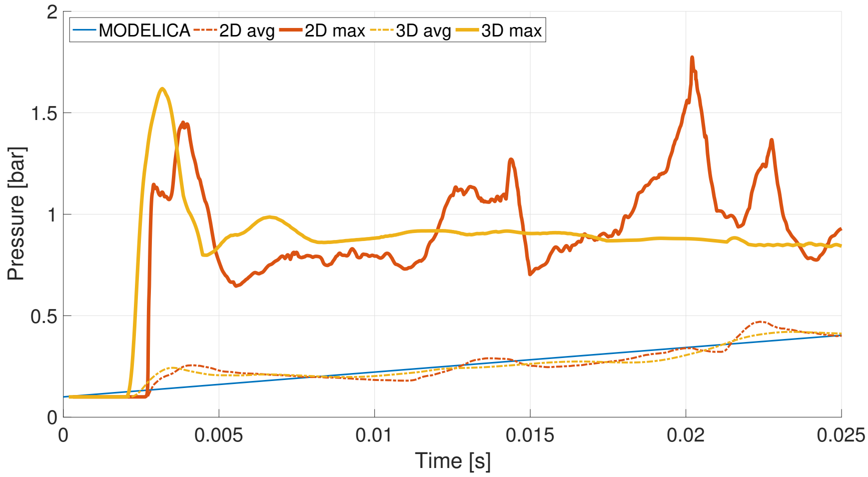

FIGURE 3.33: Pressure on internal wall.

On the 2D planar geometry, a second safety assessment is made checking the pressure on the external wall (Figure 3.34).

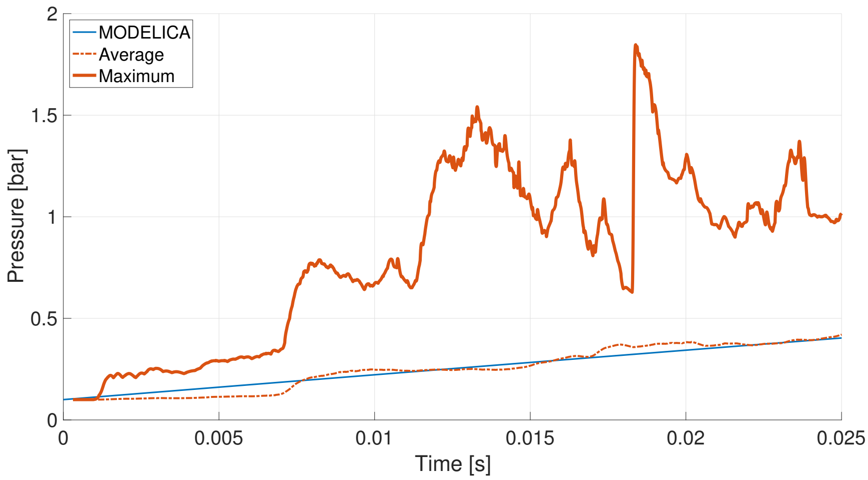

FIGURE 3.34: Pressure on the external wall of the 2D planar geometry.

After the jet impinges on the internal wall, it is deviated towards the external wall causing a first pressure peak of about 0.75 bar at t~0.007 s. The average pressure on this component does not detect any change until the first peak occurs: after that instant, the average pressure is in line with that from MODELICA. The maximum pressure, except the first peak, is characterised by an increasing trend, always below the safety limit, with maximum values slightly below 2 bar.

The preliminary analysis of the average and maximum pressure on the upper wall of the 3D toroidal domain is presented in Figure 3.35. In the 3D domain, after the impingement on the internal wall, the jet moves towards both the upper and the external walls of the domain.

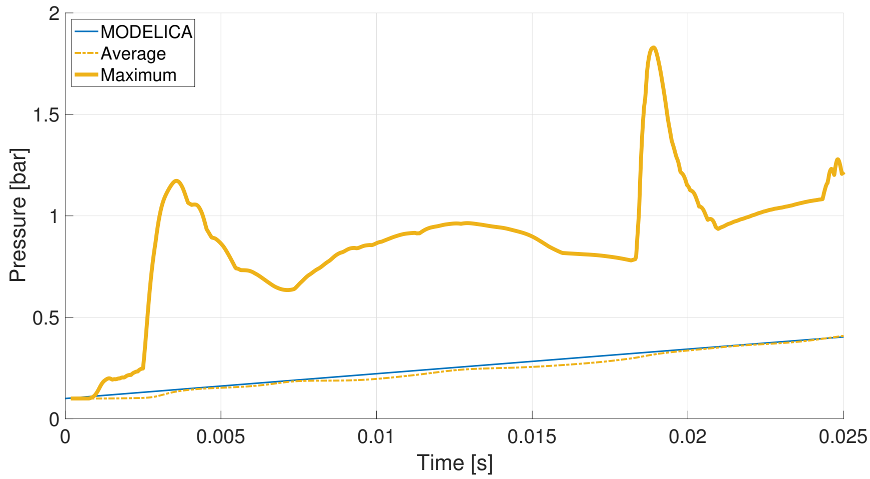

FIGURE 3.35: Pressure on the upper wall in the 3D toroidal geometry.

The average pressure perfectly matches the MODELICA results, and the maximum detected pressure values do not overtake the safety limit but high values (~1.8 bar) are detected.

3.5 Comments

Before the conclusions, it is necessary to state that the two simulated domains, even if built with proper assumptions in order relate them to the real design, are characterised by strong differences: as far as the break is of concern, the 3D domain has a localized circular inlet with a diameter of 64 cm while the 2D domain has a distributed rectangular inlet of 8.840x0.0364m. The two jets are different and the only common points between the two are the inlet boundary conditions. However, the analysis of the results from the two set-ups and their comparison with the 0D MODELICA study confirm the presence of the same phenomena and timings in both domains.

The comparisons with the 0D model results confirm the general trend of the analysed physical parameters: since the VV is being filled an increase of pressure, temperature and density is expected. The density from the CFD simulations is in perfect agreement with MODELICA due to the inlet mass flow imposed; a different result should worry since the density is related to the mass, and the mass must be conserved. Pressure and temperature values, linked to the density by the perfect gas law, are calculated considering this constraint: if the pressure is underestimated with respect to MODELICA, also the temperature will be underestimated (and vice versa). The constraint is respected as showed in the pressure and temperature evolution of the 3D and 2D domains.

The analysis of the pressure value on the BD is of key importance since the duration of the transient and its criticality depends directly on this value: when the BD surface detects values higher than 1.5 bar, it breaks and the helium from the in-VV LOCA is discharged towards the VVPSS and the expansion volumes. The MODELICA simulation, based on a 0D model, cannot detect the presence of local peaks, and consequently its VVPSS is expected to start operating when the average pressure reaches 1 bar (for the BLs) and 1.5 bar (for the BDs) on the entire domain, respectively at t_{BLs}~0.071 and t_{BD}~0.110 s. Conversely, the CFD study is able to detect pressure peaks: both 3D and 2D simulations confirm the presence of a first pressure peak on the BD surface at t=0.020 s that should trigger the break of the disk earlier than MODELICA. The agreement between the two CFD timings guarantee the goodness of this result although further studies in this direction should be addressed.

The study of the pressure on the walls of the VV is performed to check whether, in case of an in-VV LOCA, too high pressure peaks (> 2 bar) can cause the structural failure of the VV. The pressure on the internal wall is checked in both the 2D and 3D domains yielding to the following conclusion: at t~0.0025 s the jet impinges on the internal wall without overtaking the safety limit. The same conclusion can be stated for the pressure on the external wall checked on the 2D domain and for the pressure values on the upper part of the wall of the 3D domain. However, dangerous pressure peaks higher than 1.5 bar are detected both on the internal and on the external surfaces of the VV.

Chapter 4

Conclusions and perspectives

The in-Vessel Loss of Coolant accident is one of the most critical event for a tokamak since, in absence of proper safety and mitigating systems such as the VVPSS, it can bring to the structural failure of the walls of the Vacuum Vessel with a possible dangerous release of radioactive inventory to the environment. Studies have already been performed by means of a 0D model, where only the average value for the pressure is evaluated, in order to check the suitability of the strategy of He discharge into an expansion volume by means of burst disks or bleeding lines equipped with valves.

In this thesis, the CFD analyses, performed within the commercial code STAR-CCM+, involve the simulation of the accidental sequence developing after a break of a He-cooled portion of the First Wall inside the Vacuum Vessel of the EU DEMO reactor and the evaluation of the pressure transient.

In the first part of the thesis, different features of the CFD model have been selected and benchmarked against experimental results found in literature regarding steady and unsteady jets evolution in open domains and the interaction between jets and cylindrical walls. These benchmarks allow to perform a preliminary verification of the capability of STAR-CCM+ to properly predict the relevant phenomena that characterize the in-VV LOCA and to find the most suitable settings to model them from the numerical point of view. The CFD results demonstrate that the application of the RANS k-ω SST turbulence model as well as a wall treatment characterised by the presence of 5 prism layers on walls bring to successful benchmark with published data. An Adaptive Mesh Refinement algorithm based on the CFL condition is introduced to reduce the computational time without decreasing the result resolution. Detailed convergence studies have been performed in order to find the proper time-step, grid base size and number of inner iterations to be used in the CFD study, and the velocity threshold for the AMR algorithm: the combination of these models/parameters are then applied to the final simulation.

The transient evolution of the in-vessel LOCA in the EU DEMO reactor is simulated considering two different simplifications of the real VV toroidal geometry:

1. a 2D cylindrical domain, modelled distributing the break and the Burst Disks on the entire height of the VV;

2. a 3D toroidal geometry built simplifying the real EU DEMO VV geometry with a symmetric domain.

The comparisons of the results regarding the evolution in time of the average value of pressure, temperature, density and mass need detailed analyses. Density and mass inventory in both the 3D and 2D domains are in line with those expected from the 0D model, except some negligible distortions and oscillations in the 2D simulation. The evaluation of pressure peaks on the walls of the VV as well as on the surface of the Burst Disk has been then performed. As far as the timing of these peaks is of concern, both the 2D and 3D simulations show a pressure peak that would break the BD at t~0.020 s ($p_{rupture}$= 1.5 bar), to be compared to the much larger time for the rupture obtained from the 0D model which is foreseen at t=0.11 s. Average and maximum pressure on the external and upper walls have been checked, respectively, on the 2D planar domain and the 3D toroidal domain showing that in both layouts the pressure structural limit (2 bar) is not overtaken before the rupture of the BD; however, the presence of very high peaks over 2 bar are expected to occur – this second phase of the simulations would require, however, the modelling of the He discharge through the BD, which was beyond the scope of my thesis.

Some aspects could deserve some more attention in future works on this topic following two main lines:

1. The simulation of the accident considering the discharge of helium from the BD to the VVPSS, properly modelling the choked flow that is expected to occur and investigating the presence of pressure peaks on the VV walls. (Note that, being the discharge choked, the flow rate towards the VVPSS can be too small to avoid a fast pressurization of the VV over the safety limit).

2. The simulation of the LOCA imposing the real quasi-vacuum initial condition in the VV. The use of DSMC simulation should be considered for the very first portion of the transient, to assess the limitations of the continuum approach adopted by CFD.

Bibliography

[1] National Aeronautics and Space Administration (NASA). *NASA.com*. 2017. URL: https://www.grc.nasa.gov/www/K-12/airplane/mflchk.html (visited on 05/2018).

[2] A. Bertinetti et al. *Analysis of VVPSS for Helium and Water cooled Breeding Blankets*. Tech. rep. EUROfusion, 2017.

[3] G. Bird. "Molecular gas dynamics and the direct simulation monte carlo of gas flows". In: *Clarendon, Oxford* 508 (1994), p. 128.

[4] G. Caminha. *The Steve Portal - Online Official STAR-CCM+ guide*. Aug. 2017. URL: https://www.simscale.com/blog/2017/08/cfl-condition/ (visited on 05/2018).

[5] *CFD online*. URL: https://www.cfd-online.com/Wiki/Courant%E2%80%93Friedrichs%E2%80%93Lewy_condition (visited on 01/2018).

[6] EFDA. *Fusion Electricity: A roadmap to the realisation of fusion energy*. Nov. 2012.

[7] P. L. Eggins and D. A. Jackson. "Laser-Doppler velocity measurements in an under-expanded free jet". In: *Journal of Physics D: Applied Physics* 7.14 (1974), p. 1894.

[8] F4E. *Fusion for Energy*. URL: http://fusionforenergy.europa.eu (visited on 04/2018).

[9] A. Field. *The Steve Portal - Online Official STAR-CCM+ guide*. Feb. 2017. URL: https://thesteveportal.plm.automation.siemens.com/articles/en_US/FAQ/Do-I-need-prism-layers-How-many-should-I-use-temp (visited on 12/2017).

[10] A. Field. *The Steve Portal - Online Official STAR-CCM+ guide*. Oct. 2017. URL: https://thesteveportal.plm.automation.siemens.com/articles/en_US/FAQ/Define-the-time-step-using-Courant-number (visited on 01/2018).

[11] A. Field. *The Steve Portal - Online Official STAR-CCM+ guide*. Oct. 2017. URL: https://thesteveportal.plm.automation.siemens.com/articles/en_US/FAQ/How-do-I-know-if-my-flow-is-too-rarefied (visited on 06/2018).

[12] A. Field. *The Steve Portal - Online Official STAR-CCM+ guide*. Mar. 2018. URL: https://thesteveportal.plm.automation.siemens.com/articles/en_US/FAQ/How-to-do-a-grid-dependence-study (visited on 04/2018).

[13] A. Field. *The Steve Portal - Online Official STAR-CCM+ guide*. Mar. 2018. URL: https://thesteveportal.plm.automation.siemens.com/articles/en_US/FAQ/JC-5-009 (visited on 04/2018).

[14] E. Franquet et al. "Free underexpanded jets in a quiescent medium: A review". In: *Progress in Aerospace Sciences* 77 (2015), pp. 25 –53. ISSN: 0376-0421.

[15] C. Freudenrich. *Science: how stuff works.* 2016. URL: https://science.howstuffworks.com/fusion-reactor3.htm (visited on 06/2018).

[16] A. Froio et al. "Benchmark of the GETTHEM vacuum vessel pressure suppression system (VVPSS) model for a helium-cooled EU DEMO blanket". In: *Safety and Reliability–Theory and Applications* (2017), pp. 11–18.

[17] A. Froio et al. "Modelling an in-vessel loss of coolant accident in the EU DEMO WCLL breeding blanket with the GETTHEM code". In: *Fusion Engineering and Design* (2018), p. 5. ISSN: 0920-3796.

[18] R. Ishii et al. "Experimental and numerical analysis of circular pulse jets". In: *Journal of Fluid Mechanics* 392 (1999), pp. 129–153.

[19] S. E. Mattsson, H. Elmqvist, and M. Otter. "Physical system modeling with Modelica". In: *Control Engineering Practice* 6.4 (1998), pp. 501–510.

[20] G.F. Nallo et al. "Modeling the lithium loop in a liquid metal pool-type divertor". In: *Fusion Engineering and Design* 125 (2017), pp. 206 –215. ISSN: 0920-3796. DOI: https://doi.org/10.1016/j.fusengdes.2017.07.004.

[21] L. Normand. *Statistical thermodynamics: fundamentals and applications.* Cambridge University Press, 2005.

[22] N. Novembre, F. Podenzani, and E. Colombo. "Numerical study for accidental gas releases from high pressure pipelines". In: *ECCOMAS CFD 2006: Proceedings of the European Conference on Computational Fluid Dynamics.* 2006.

[23] ITER organization. 2016. URL: https://www.iter.org/ (visited on 06/2018).

[24] E. Pederiva. "Towards the CFD simulation of accidents on off-shore platforms: dispersion of a turbulent jet hitting a cylinder". MA thesis. Politecnico di Torino, Mar. 2015.

[25] R. H. Perry and D. W. Green. *Perry's Chemical Engineers'Handbook.* 8th ed. McGraw-Hill, 2008.

[26] Simcenter STAR-CCM+. *Release Notes.* 13.04.

[27] S. P. A. Tabrizi. "Jet impingement onto a circular cylinder". PhD thesis. University of Liverpool, 1996.

[28] *The European Fusion Education Network.* URL: www.fusenet.eu (visited on 06/2018).

[29] J. Zuev. *Courant Stability Conditions for first order scheme of advection equation.* Boulder, CO, USA, 2002.

Appendix A

Convergence studies

This appendix describes the rationale that brought to the choice of the time-step and the minimum number of inner iterations for the study present in section 2.3.2. The simulations are performed on the same set-up described in section 2.3.2. From the quantitative study, the analysis is based on the convergence of the Mach disk location (Figures A.1 and A.4) and the dimension of its radius (Figures A.2 and A.3). A qualitative analysis aimed at confirming furtherly the quantitative results is present at the end of the Appendix and regards the evolution of the maximum velocity detected on the axis of the jet (Figures A.5 and A.6). All the simulations are performed with a velocity threshold for the AMR algorithm of 0.25Vmax. The first study is performed on the mesh base size which is directly related to the time- step by the AMR algorithm; starting with 10 inner iterations the study is performed on four different cases summarised in A.1

TABLE A.1: Cases for the time independence study.

Time-step [μs]	**Maximum number of cells** [-]
1	23000
0.75	38000
0.5	85000
0.25	310000

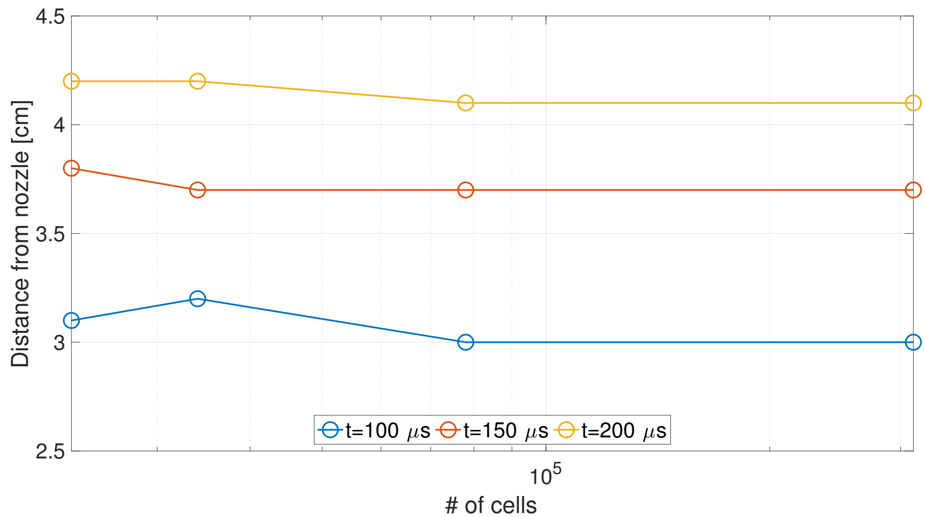

FIGURE A.1: Convergence study on the Mach disk location changing the time-step.

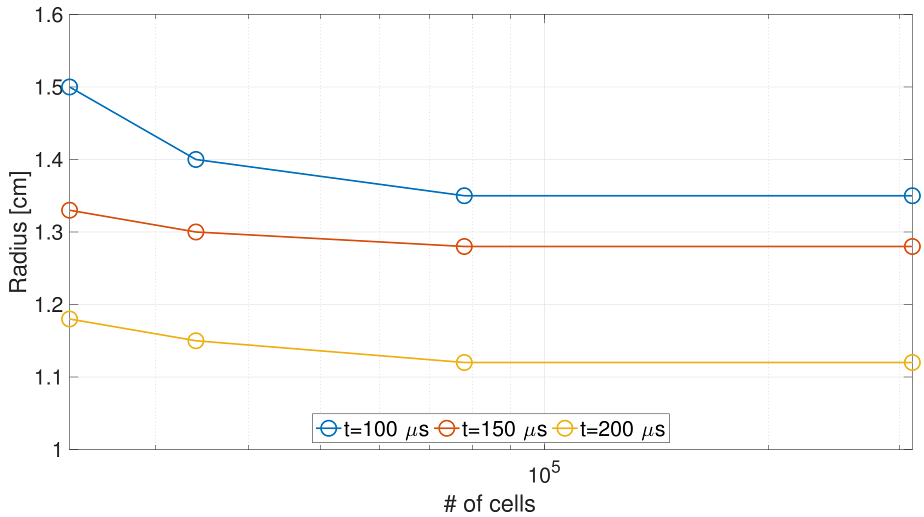

FIGURE A.2: Convergence study on the radius of the Mach disk changing the time-step.

Figures A.1 and A.2 demonstrate that with a mesh characterized by a maximum number of cells equal to 100k (corresponding to a time-step of 0.5 μs), the checked parameters reach convergence.
The same study is performed for the evaluation of the number of inner iterations that guarantees convergence for the Mach disk radius and location. This study is performed with the time-step from the previous convergence study (0.5 μs) on simulations characterized by 5, 10, 20, 40 inner iterations.

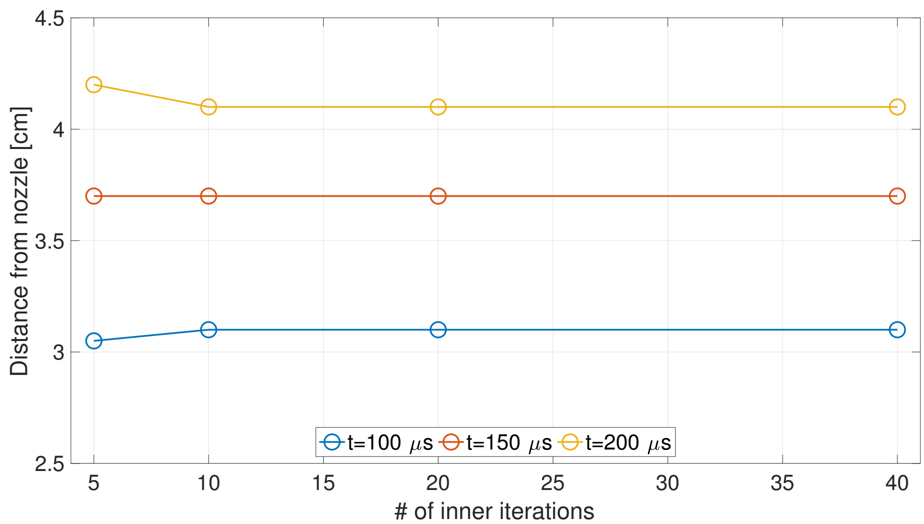

FIGURE A.3: Convergence study on the Mach disk location changing the number of inner iterations.

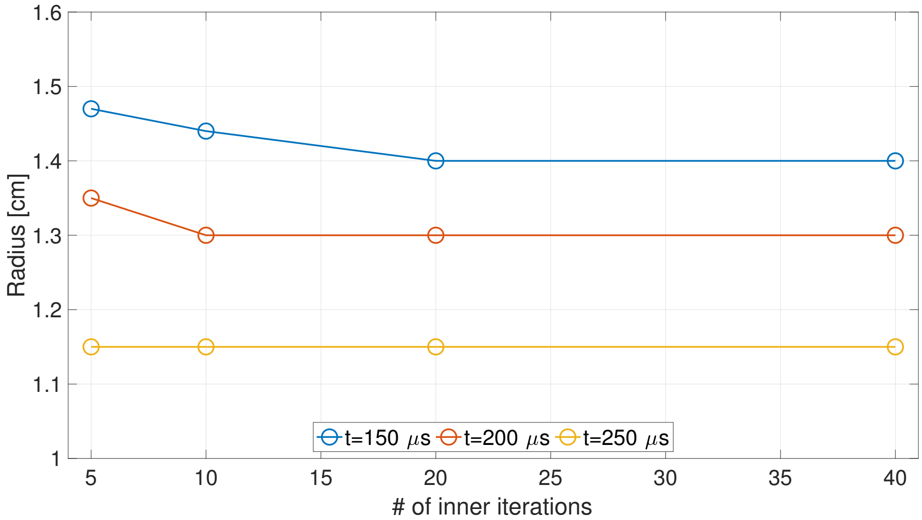

FIGURE A.4: Convergence study on the radius of the Mach disk changing the number of inner iterations.

In this case convergence is reached with 20 inner iterations.

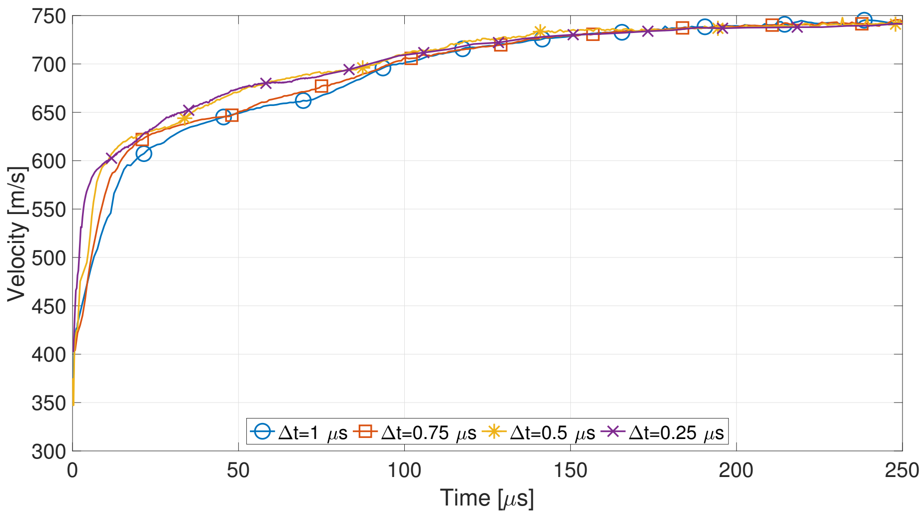

FIGURE A.5: Maximum velocity trend on the symmetry axis changing the time-step.

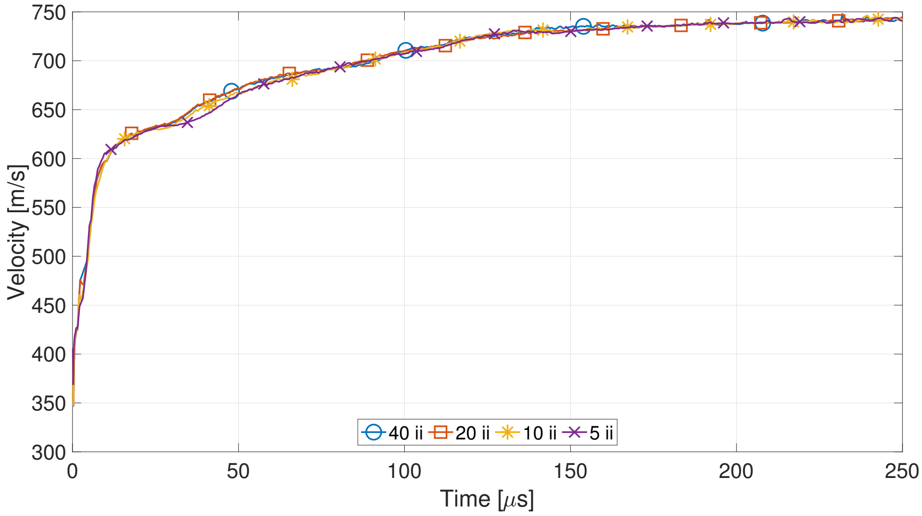

FIGURE A.6: Maximum velocity trend on the symmetry axis changing the number of inner iterations.

The analysis of the maximum velocity evolution in time is stating that this parameter is not strongly affected by the changing the grid base size and the inner iterations. However, some distortions are present in the first phase of the transient. Following this study, a time-step of 0.5 μs related to a grid of about 100000 cells and a minimum number of inner iterations equal to 20, can be set for the study of the unsteady free jet.

Appendix B

Choked flow

Choked flow is a phenomenon that occurs when a compressible fluid flows through a nozzle connecting two different chambers characterised by a pressure ratio lower than a certain threshold value. This value, called critical ratio (β_{cr}), evaluated from Equation B.1,

$$\beta_{cr,He} = \left(\frac{2}{k+1}\right)^{\frac{k}{k-1}} \tag{B.1}$$

depends only on $k = c_p/c_v$, the specific heat ratio, which is a characteristic value of each gas (for Helium k=1.667 [25]). In a convergent nozzle, in case of choked flow, each section is characterised by sonic conditions and the local velocity depends only on the local temperature: it means that the flow conditions do not depend on those present at the nozzle exit. Figure B.1 shows a convergent nozzle where the inlet conditions are "total" since the incoming velocity is 0 and the flow is quiet; instead, local conditions where the fluid is in motion are called "static".

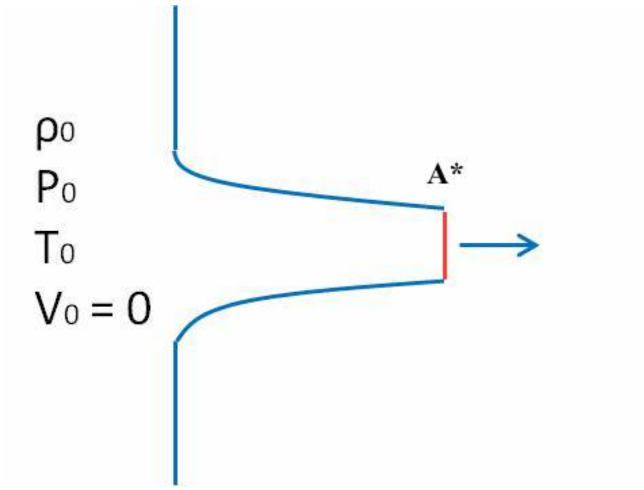

FIGURE B.1: Sketch of a convergent nozzle.

In case of an in-VV LOCA, the helium in the Breeding Blanket is in total conditions and due to the huge pressure difference occurring between the VV and the PHTS, choked flow is expected to occur at the break: as a consequence, the break is modelled as a surface on which sonic conditions are present. The static conditions on the break can be evaluated by Equations B.2 - B.4 [1] that link total to static conditions as a function of k and the Mach number value (M):

$$\frac{T_{tot}}{T_{st}} = \left(1 + \frac{k-1}{2}M^2\right) \tag{B.2}$$

$$\frac{p_{tot}}{p_{st}} = \left(1 + \frac{k-1}{2}M^2\right)^{\frac{k}{k-1}} \tag{B.3}$$

$$\frac{\rho_{tot}}{\rho_{st}} = \left(1 + \frac{k-1}{2}M^2\right)^{\frac{1}{k-1}} \tag{B.4}$$

The mass flow rate, as expressed by Equation B.5 [1], depends only on the inlet conditions and the outgoing flow area:

$$\dot{m}_{t=0} = A^* \frac{p_0}{\sqrt{R^* T_0}} \sqrt{k \left(\frac{2}{k+1}\right)^{\frac{k+1}{k-1}}} \tag{B.5}$$

Also the sonic velocity can be evaluated being dependent only on the static temperature at the outlet and on the gas parameters [1]

$$C_{s,t=0} = \sqrt{k R^* T_{st}} \tag{B.6}$$

Table B.1 shows the static and total conditions for the in-VV LOCA studied in this thesis referring to the parameters outlined in Table B.2.

TABLE B.1: Characteristics of the gas and the break.

p_{VV}/p_{PHTS} [-]	0.00125
Specific heat ratio, k [-]	1.667
Gas constant, R* [J/kgK]	2078.5
Rupture area [m^2]	0.322

TABLE B.2: Total and static conditions on the rupture area at start-up.

	TOTAL	**STATIC**
Pressure [bar]	80	39
Temperature [K]	673	505
Density [kg/m^3]	5.71	3.72
Mach [-]	0	1
Velocity [m/s]	0	1323
Flow rate [m^3/s]	0	1582

Appendix C

Justification of the CFD approach

The in-Vessel LOCA is characterized by high Mach flow towards high vacuum conditions. It is therefore necessary to assess whether the continuum assumption, which is one of the fundamental requirements for CFD codes to be employed, is satisfied.

In general, flow problems can be divided into four flow regimes based on the Knudsen number, which is a dimensionless parameter defined as the ratio between the mean free path of a particle (atom or molecule) (λ) and a characteristic length of the system (L) [3].

$$Kn = \frac{\lambda}{L} \tag{C.1}$$

The four flow regimes are summarised in Table C.1.

TABLE C.1: Flow regimes definition based on Knudsen number.

Kn < 0.01	Continuum
0.01 < Kn < 0.1	Slip flow regime
0.1 < Kn < 3	Transitional regime
Kn > 3	Free molecular flow

The two quantities arising in equation C.1 can be evaluated as follows. The mean free path, for a Boltzmann gas, can be evaluated by means of Equation C.2 [21]:

$$\lambda(t) = \frac{k_b T(t)}{\sqrt{2}\pi d^2 p(t)} \tag{C.2}$$

where, k_b is the Boltzmann's constant, T is the temperature, p is the pressure and d is the Van der Waals diameter of the particle (for Helium, d=140 pm [25]). The characteristic length of the system is instead equal to the characteristic length of the gradients of a certain quantity of the flow field, for example the density [20]:

$$L \sim \frac{\rho}{|\nabla \rho|} \tag{C.3}$$

STAR-CCM+, as well as all CFD codes, is strictly applicable only in the continuum regime where the Navier-Stokes equations are valid. In the slip flow regime, CFD can still be employed, but the conventional no-slip condition for velocity at the walls must be replaced by suitably derived expressions taking into account molecular effects. Transitional and free molecular flow regimes must be solved with different approaches aiming at the solution of the Boltzmann equation. In particular, for the transitional regime the Direct Simulation Monte Carlo (DMSC) method is widely used [26]. Therefore, the selection of the appropriate tool for solving the problem at hand should take into account the flow regime. However, both and actually depend on the solution of the problem. A possible strategy is to employ the available MODELICA results to evaluate Kn as a function of time. However, being MODELICA a 0D model, only a global Knudsen number can be evaluated which assumes as characteristic length of the gradients a geometric length of the system. The latter can be approximated as the distance between the internal and the external wall of the VV (6 metres) [20]. The evolution of the Knudsen number in time is hence calculated. As shown in Figure C.1, at the very beginning of the transient, until t*= 3 μs, the Knudsen number is larger than the validity limit of CFD codes (the yellow dotted line). Even though t* can appear small with respect to the entire transient, this evaluation points out the fact that a CFD approach cannot be employed for the whole entire transient and for the entire domain. As a consequence of these considerations, the initial pressure of the benchmarked MODELICA set-up used in this thesis is increased to 10 kPa in order to avoid high Knudsen number at the start-up: Figure C.1 shows that with the new initial conditions, the global Knudsen remains below the limit for the entire duration of the transient justifying the study of the accident with a CFD approach. This choice will allow a fair comparison between the 3D approach and the lumped 0D model. In the future, a combination of CFD (for the high-collisionality regions) and DSMC (for the low collisionality regions) might be employed.

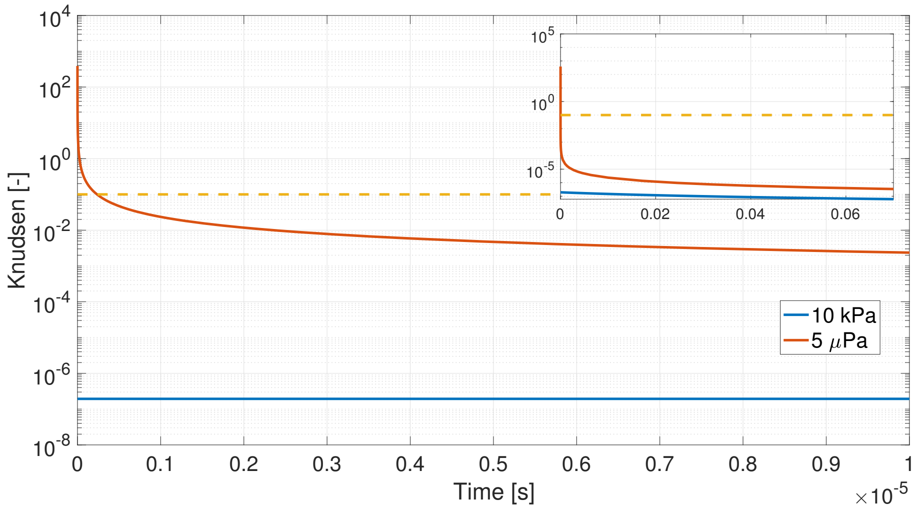

FIGURE C.1: Evolution in time of the Knudsen number for the two cases considered.